A Quantum Information Approach to Material Science Simulations

Christopher Willby
St Anne's College
University of Oxford

A thesis submitted for the degree of
Doctor of Philosophy
Michaelmas 2024

Abstract

Despite its ubiquity, many-body dispersion remains poorly understood. There have been numerous studies confirming the importance of many-body effects in dispersive forces. These often play a decisive role in determining properties and functionalities of physical, chemical and biological systems, ranging from condensed phases in noble gases to biomolecules and nanomaterials. Still, a general understanding of their behavior is lacking.

In this thesis we study many-body dispersion with quantum Drude oscillator assemblies — minimal models for dispersion bound systems. We show how Gaussian states provides an efficient and comprehensive framework for understanding many-body forces, within the quantum Drude model. In doing so, we analytically and rigorously establish how the distribution of entanglement in the QDO model governs many-body dispersive bond energies. We further show how the monogamy of entanglement can be used to predict whether many-body corrections to the bond energy are repulsive or attractive.

The work in this thesis does not aim to study a specific physical system or experiment. Instead, we use model systems and analytical results to characterize and discuss how entanglement properties affect dispersive bonds. Importantly, our method is applicable to arbitrary arrangements of dipoles and hence to a wide range of systems.

Gaussian state quantum information tools bring important insights and understanding of dipolar forces from a new angle. In addition the Gaussian state approach allows us to construct efficient symplectic optimization algorithms for variationally solving the coupled quantum Drude model. Our symplectic optimization algorithm provides a novel route towards including many-body dispersive forces in material simulations. We further show how our symplectic optimization algorithm can in principle be turned into a variational quantum algorithm. Our methods and results

provide a path toward fully understanding the nature of quantum effects in large biomolecules and complex crystal structures.

Contents

1 Introduction **2**

1.1 Background . . . 2
1.2 Publications . . . 5
1.3 Thesis Results . . . 5
1.4 Thesis Structure . . . 7
1.5 Thesis Notation . . . 8
1.6 Computational Resources . . . 9

2 Gaussian States **10**

2.1 Introduction . . . 10
2.2 Phase Space Representation . . . 10
2.2.1 Quadractic Hamiltonians . . . 12
2.3 Correlation Matrix and Symplectic Diagonalization . . . 12
2.3.1 Gaussian density matrices . . . 12
2.3.2 Gaussian correlation matrices . . . 13
2.3.3 Gaussian variational principle . . . 14
2.3.4 Symplectic diagonalization . . . 14
2.3.5 Block diagonal Hamiltonians . . . 16
2.4 Conclusion . . . 17

3 Entanglement Monogamy **18**

3.1 Introduction . . . 18
3.2 Qubit Monogamy . . . 19
3.3 Gaussian Tangle . . . 20
3.3.1 Gaussian tangle in a two mode state . . . 21
3.3.1.1 Standard form . . . 21
3.3.1.2 Detecting two mode entanglement . . . 23
3.3.1.3 Two mode entanglement in a pure state . . . 24

3.3.2 Gaussian tangle in a multimode state . . . 25
3.4 Gaussian Monogamy . . . 27
3.4.1 Gaussian monogamy inequality . . . 27
3.4.2 Proof of Gaussian monogamy inequality . . . 27
3.5 Conclusion . . . 28

4 Promiscuity and Monogamy in Gaussian States 29
4.1 Introduction . . . 29
4.2 Two Mode State . . . 30
4.3 Three Mode State . . . 31
4.4 Low Dimensional Approximation . . . 32
4.4.1 Multipartite state . . . 32
4.4.1.1 Three mode state . . . 34
4.5 Mean-Field Cluster . . . 35
4.6 Conclusion . . . 38

5 A Quantum Information Perspective on Many-Body Dispersive Forces 40
5.1 Introduction . . . 40
5.2 QDO Model . . . 40
5.2.1 Many-Body effects . . . 41
5.2.1.1 Axilrod-Teller potential . . . 42
5.2.2 Gaussian state CM . . . 43
5.2.2.1 Bounds in the QDO CM . . . 43
5.3 Multipartite Gaussian Entanglement and Energy . . . 45
5.3.1 Reduced tangle . . . 45
5.3.2 Reduced tangle bound on the MB energy . . . 45
5.3.3 Pairwise tangle bound on MB energy . . . 46
5.4 Trimer, Chains and Extended Lattices . . . 47
5.4.1 Relative density . . . 47
5.4.2 Entanglement distribution index . . . 47
5.4.3 Trimer . . . 48
5.4.3.1 Trimer setup . . . 48
5.4.3.2 Axilrod-Teller in the trimer . . . 49
5.4.3.3 EDI and MB effects . . . 50
5.4.3.4 Reduced tangle bounds . . . 50
5.4.4 Linear and zigzag chain . . . 54
5.4.4.1 EDI and MB effects . . . 54

5.4.4.2 Reduced tangle bounds . . . 55
5.4.5 2D crystal lattices . . . 55
5.4.5.1 EDI and MB effects . . . 59
5.4.6 3D crystal lattices . . . 60
5.4.7 Finite size effects . . . 61
5.5 Conclusion . . . 61

6 Symplectic Optimization **63**
6.1 Introduction . . . 63
6.2 Symplectic Trace Minimization . . . 64
6.2.1 Symplectic matrix constraint . . . 64
6.2.2 Symplectic trace cost function . . . 65
6.3 Unconstrained Symplectic Trace Minimization . . . 66
6.3.1 Unit triangular factorization . . . 66
6.3.1.1 Computing Gradients . . . 67
6.3.2 Numerical examples . . . 68
6.4 Quantum Symplectic Optimization . . . 70
6.4.1 Bloch-Messiah decomposition . . . 72
6.4.2 VQA for solving Eq. (2.22) . . . 73
6.5 Conclusion . . . 74

7 Conclusion **75**
7.1 Summary of work . . . 75
7.2 Outlook . . . 76

A **79**
A.1 Mixed State Pairwise Tangle . . . 79
A.2 Properties of $f(x)$ . . . 80
A.3 von Neumann Entanglement Entropy . . . 81
A.4 Entanglement Between Modes 1 and 3 in a Tripartite State . . . 81

B **82**
B.1 The General QDO Hamiltonian Applied in Material Simulation . . . 82
B.2 Binomial Coefficients . . . 84
B.3 Properties of $g(x)$ . . . 84
B.4 Negativity Bounds . . . 85
B.5 Further Bounds . . . 87

B.5.1 Tangle bounds on the CM matrix . . . 87
B.5.2 Bounds on the deviation between the MB bond energy and the reduced tangle . . . 87
B.6 Low Dimensional Trimer Approximation . . . 88
B.7 $\delta^{\mu,\mu+1}$ in Linear/Zigzag Chain . . . 89
B.8 $|\delta_4| = |\delta_3|$ Trimer Boundary . . . 89
B.9 Reduced Tangle Bounds on Lattices . . . 89
B.10 Trimer Distribution of $\tau^{\star}_{G}(i:j)$ . . . 89

C **93**
C.1 Symplectic Singular Value Decomposition (SVD) . . . 93
C.2 Unit Triangular Factorization . . . 93
C.3 Learning Entanglement in Harmonic Chain . . . 94
C.4 Hadamard Test . . . 95
C.5 Block Matrix Ansatz . . . 95
C.6 Measuring Unitary Trace . . . 95
C.7 Proof of Principle of VQA . . . 99
C.8 Symplectic Ansatz . . . 100

Bibliography **102**

List of Figures

1.1 The three QDO system (trimer) captures the features of many-body dispersion on lattices. The key result of this thesis is to show how quantum information theory forecasts the breakdown pairwise dispersion forces and determines whether the many-body interactions are attractive or repulsive. 6

3.1 Regions enclosed by the black line, show valid two modes CMs, where $\boldsymbol{\Delta} < 1 + \det(\gamma)$ and thus the Robertson-Schrödinger relation (uncertainty principle) relation is obeyed. The darker shaded regions enclosed by the red dotted lines, shows the portion of valid two mode CMs which exhibit entanglement. This condition is given by $\tilde{\boldsymbol{\Delta}} > 1 + \det(\gamma)$. In a) $a = 2.2$ and $b = 1.1$, whereas in b) $a = 8$ and $b = 4$. 22

3.2 Green circles show $(\tilde{\nu}_-^{-1})_1 = \sqrt{\langle \hat{\chi}_1^2 \rangle \langle \hat{\mathcal{P}}_1^2 \rangle} + \sqrt{\langle \hat{\chi}_1^2 \rangle \langle \hat{\mathcal{P}}_1^2 \rangle - 1}$, while black crosses indicate $(\tilde{\nu}_-^{-1})_1 = \min(|\mathrm{eig}(\mathrm{i}\sigma\tilde{\gamma}_1)|)$, with $\tilde{\gamma}_1$ obtained from Eq. (3.9). Results are shown for a 1D chain of QHOs (see Eq. (3.30)) across different nearest-neighbor coupling values κ as a function of chain length. The mode label is omitted on the y-axis due to the symmetry of the chain. 25

4.1 Coupling graph of a three mode Hamiltonian in Eq. (4.8), illustrated for $\beta = 1$. The red circle illustrates the bipartition between mode i and the other two modes, where $\tau_G(i)$ measures the entanglement across this bipartition and limits the strength of the pairwise tangle between modes i and j, to be no greater then $\tau_G^{\mathrm{sys}}(i:j)$. The reference tangle, given by $\tau_G^{\mathrm{ref}}(i:j)$, is the Gaussian tangle between i and j in the groundstate of the two mode Hamiltonian, $\hat{H}_{ij}$. 31

4.2 The monogamy/promiscuity boundary is shown by the solid black line, below which the entanglement behaves monogamously and above which, promiscuously. Both regions are shown as heat-maps, plotted on a log-scale. This is shown for different values of κ and β, see Eq. (4.8) for definitions of these parameters. The dotted lines show the contours of $\tau_G^{\rm sys}(1:2)/\tau_G^{\rm ref}(1:2) - 1$. 33

4.3 The solid orange curve is the tangle computed from solving Eq. (4.8) exactly. The dashed dotted black line, follows from the truncated Fock state approximation, with Hamiltonian given in Eq. (4.9) and $d = 3$. Below the horizontal dashed line shows where the pairwise entanglement between 1 and 2 behaves monogamously whereas above shows the promiscuous behavior. 35

4.4 (Top) Monogamous behavior of the entanglement distribution in the mean field cluster. The decay of $\tau_G^{\rm sys}(i:j)/\tau_G^{\rm ref}(i:j)$ as a function of d is shown for two different coupling strength values. (Bottom) Decay of the tangle as a function of number of modes, plotted for a range of different coupling strength values. In the limit $d \to \infty$ each mode shares no entanglement with the rest of the cluster. 36

4.5 **a)** shows that the tangle decays with $\mathcal{O}(d^{-1/2})$ in the limit $d \to \infty$. **b)** shows the decay of the pairwise tangle, where $\tau_G^{\rm sys}(i:j)$ decays to zero as $\mathcal{O}(d^{-3/2})$. 39

5.1 AT potential in the trimer at $\rho = 2.60$ (see Sec. 5.4, for a definition of ρ and the trimer). The orange crosses show δ_3 computed via the r.h.s of Eq. (5.8), whereas the solid grey curve shows δ_3 computed by the l.h.s of Eq. (5.8). 49

5.2 (Top) Depiction of the dipole interacting trimer setup. The correlated charge density fluctuations, are shown by the instantaneous dipoles $\pm\delta$. (Bottom) Above the red dotted line the sum of the pairwise tangle shared between the nearest neighbor QDOs behaves promiscuously, whereas below it behaves monogamously. The monogamy/promiscuity boundary overlaps the black line where MB energy corrections vanish and the pairwise additive approximation holds; above which MB corrections are attractive and below which are repulsive; both shown as heat-maps, plotted on a log scale. 51

5.3 **a)** Behavior of the nearest neighbor EDI, $\delta^{1,2}_{\tau_G}$, at different angles, with the dotted red line separating promiscuous and monogamous regions. **b)** Behavior of the MB potential δ_{MB}, shown for the same three angles as shown for **a)**. 52

5.4 In **a) – b)**, where $\rho = 2.60$ and $\rho = 1.55$ respectively, the cross/plus symbols show S_l, where $S_l = \sum_{k=1}^{l}(k-1)\delta_k$, normalized by $S_{l\to\infty} = \sum_{k=1}^{\infty}(k-1)\delta_k$. The latter is computable from the CM matrix elements, see Sec. 5.3 for calculation details. The dashed-dotted (black) and solid (orange) horizontal lines show the normalized value of the reduced tangle, i.e $\tilde{\tau}_G/S_{l\to\infty}$ for the respective ρ and θ values (dashed line for $\pi/3$ and dotted line for π). The dashed-dotted (green) and solid (green) horizontal lines show the normalized value of the total ground state maximal pairwise tangle. i.e $g(\tau_G^{\mathrm{sys}})/S_{l\to\infty} = g(\sum_{ij}\tau_G^{\mathrm{sys}}(i:j))/S_{l\to\infty}$. . 52

5.5 (Top) Illustration of the chain setup, with chain geometry depending on θ. (Bottom) Above the red dotted line the sum of the pairwise tangle shared between the nearest neighbor QDOs at the center of the chain behaves promiscuously, whereas below it behaves monogamously. For $\rho \geq 2$, the monogamy/promiscuity boundary overlaps the black line where MB energy corrections vanish and the pairwise additive approximation holds; above which MB corrections are attractive and below which are repulsive; both shown as heat-maps, plotted on a log scale. 53

5.6 The cross/plus symbols show S_l, where $S_l = \sum_{k=1}^{l}(k-1)\delta_k$, normalized by $S_{l\to\infty} = \sum_{k=1}^{\infty}(k-1)\delta_k$, where $\rho = 3$ in **a)** and $\rho = 1.85$ in **b)**. This is shown for the linear (cross symbols connected by dashed dotted lines) and zigzag chain (plus symbols connected by solid orange line). The horizontal lines show the reduced tangle, normalized by $S_{l\to\infty}$, for the different configurations. For large l, the series $S_l = \sum_{k=1}^{l}(k-1)\delta_k$ converges to lie above the horizontal lines, thus verifying the bound in Eq. (5.19), for the linear and zigzag chains. 55

5.7 Behavior of the MB effects and entanglement on the $N = 47 \times 47 \times 2$ honeycomb lattice. **a)** The solid line shows the MB effects, the small green dotted line the AT correction, the large orange dotted line shows four-body corrections added to the AT potential, the dashed dotted line shows the deviation between the sum of the reduced tangle of each of the $3N$ modes and the pairwise bonding energy, $(\tilde{\tau}_G - \delta_2)/2$, with the factor of $1/2$ included as $(\tilde{\tau}_G - \delta_2)/2 \to \delta_3$ for $\rho \to \infty$. All the curves have been normalized by the pairwise bond energy and have been plotted as a function of the dimensionless nearest neighbor separation ρ. **b)** The EDI between μ and $\xi = \mu + a$ on the honeycomb lattice. The dashed horizontal line shows the monogamy/promiscuity boundary, with the monogamous region lying below and the promiscuous region above. The ordering of the QDOs on the 2D lattices is shown in the inset, where $\mu = 2256$. All lattices calculations have been preformed with open boundary conditions. 56

5.8 Behavior of MB effects and entanglement on **a)** the $N = 71 \times 71$ square lattice and **b)** the $N = 71 \times 71$ triangular lattice. In **a)**–**b)**, the same quantities are plotted as those shown for the honeycomb lattice in Fig. 5.7. All the curves have been normalized by the pairwise bond energy and have been plotted as a function of the dimensionless nearest neighbor separation ρ. The EDI between μ and $\xi = \mu + a$ on the two-dimensional lattices is shown in **c)**–**d)**. The dashed horizontal line indicates the monogamy/promiscuity boundary for the respective lattices, with the monogamous region lying below and the promiscuous region above. The ordering of the QDOs on the 2D lattices is shown in the insets of **b)**–**c)**, with $\mu = 2520$ in both **c)**–**d)**. The open green square in **c)** marks the point where the PPT criterion ensures $\tau_G(3\mu : 3\xi) = 0$. All lattices calculations have been preformed with open boundary conditions. 57

5.9 Behavior of the MB effects and entanglement on **d)** $N = 19 \times 19 \times 19$ cubic lattice and **h)** $N = 4 \times 12 \times 12 \times 12$ pyrochlore lattice. The same quantities are plotted as those shown for the 2D crystal lattices in Fig. 5.7 and Fig. 5.8 . All the curves have been normalized by the pairwise bond energy and have been plotted as a function of the dimensionless nearest neighbor separation ρ. All lattices calculations have been preformed with open boundary conditions. 58

5.10 In **a) – b)**, where $\rho = 3.4$ and $\rho = 2.2$ respectively, the markers show S_l, where $S_l = \sum_{k=1}^{l}(k-1)\delta_k$, normalized by $S_{l\to\infty} = \sum_{k=1}^{\infty}(k-1)\delta_k$, for the $N = 19\times19\times19$ cubic lattice. The horizontal line shows the normalized value of the reduced tangle, $\tilde{\tau}_G/\mathcal{S}_{l\to\infty}$. 60

5.11 Finite size scaling of the MB effects in the cubic lattice, for $\rho = 2.0$ in **a)** and $\rho = 2.6$ in **b)**. Solid dashed green lines extrapolate to $N \to \infty$, with linear fits to the last two data points in **a)** and the last 10 data points in **b)**. 61

6.1 The groundstate CM of a general quadractic bosonic Hamiltonian, which minimizes the energy as per Eq. (2.22), lives in the intersection of symmetric positive definite and symplectic matrices i.e $\gamma_0 \in \mathcal{S}p(2d,\mathbb{R}) \bigcap S^{++}(2d,\mathbb{R})$. 65

6.2 Evolution of the symplectic trace cost function on lattices. **a)** shows the honeycomb lattice with $N = 2\times3\times3$ (solid line) and $N = 6\times6\times2$ (dashed line). **b)** square lattice with $N = 4\times4$ (solid) and $N = 10\times10$ (dashed). **c)** triangular lattice with $N = 4\times4$ (solid) and $N = 10\times10$ (dashed). Finally **d)** shows the cubic lattice with $N = 4\times4\times4$ (solid) and $N = 10\times10\times10$ (dashed). In **a), c)** and **d)** we set $\rho = 1.9$ and in **b)** $\rho = 1.8$. We see the convergence to the true ground-state interaction energy for all the lattice types and sizes. The horizontal green lines show $|\delta_{\text{MB}}|/E$. For all the considered lattice sizes and ρ values, $|\delta_{\text{MB}}|/E \sim 10\%$. Hence the algorithm is able to find ground-state lattice energies of systems containing non trivial MB interactions. 69

6.3 Comparison between target CM computed via ED (see Eq. (5.10)) and the CM $\gamma_0^\star$ computed by the algorithm i.e Eq. (6.16), shown for position block in **a)** where $\epsilon_{ij}^{\mathcal{X}} = (|E_1^T\gamma_0^\star E_1 - V^{-1/2}|)_{ij}$ and the momentum block in **b)**, $\epsilon_{ij}^{\mathcal{P}} = (|E_2^T\gamma_0^\star E_2 - V^{1/2}|)_{ij}$. Both **a) – b)** are shown for $\rho = 1.8$, in the $N = 4\times4$ square lattice. 71

A.1 Heatmap of $\tau_G^{\text{sys}}(i:j)$ plotted on a log-scale for for different values of κ and β, see Eq. (4.8) and Fig. 4.2 for definitions of these parameters. The white region, shows where the PPT criterion ensures modes 1 and 3 share no entanglement. 81

B.1 The function $g(x)$ shown by the solid line, is used to define the reduced tangle. The reduced tangle is used to measures the entanglement in a bipartition between mode i and the other $3N-1$ modes in the QDO groundstate. 84

B.2 Deviation between the negativity and $\sqrt{3N\delta_2}$, where δ_2 is the pairwise interaction energy. This is shown as a heatmap on a log-scale for the trimer system, depicted in Fig. 5.2. The black line shows where $\mathcal{N} = \sqrt{3N\delta_2}$, where to the right of the black line $\mathcal{N} < \sqrt{3N\delta_2}$ and to the left $\mathcal{N} > \sqrt{3N\delta_2}$. 86

B.3 Behavior of δ_{qubit}, normalized by the pairwise potential δ_2 as a function of trimer parameters ρ and θ (see main-text for trimer definition). The black line separates the phase space into regions where $\delta_{\text{qubit}} > 0$ and $\delta_{\text{qubit}} < 0$. Both regions are shown as heat-maps, plotted on a log-scale. 88

B.4 The behavior of $\delta_{\tau_G}^{\mu,\mu+1}$ in QDOs at the edge of the chain differs from those at the center. The deviation between $\delta_{\tau_G}^{1,2}$ and $\delta_{\tau_G}^{51,52}$ is apparent in both **a)** and **b)**. In comparison for $\rho = 2.8$ $\delta_{\tau_G}^{2,3} \approx \delta_{\tau_G}^{51,52}$. 89

B.5 The boundary where $E = \delta_2$ in the trimer setup is shown here by the solid black curve, $\delta_{MB} = 0$. The boundary between repulsive and attractive AT corrections is given by the horizontal black line $\delta_3 = 0$. The dashed green line shows where $\delta_3 = -\delta_4$. Above the green line $|\delta_4| > |\delta_3|$, whereas the region enclosed by the green dashed line shows the ρ and θ values where $|\delta_4| < |\delta_3|$. 90

B.6 The crosses show $\mathcal{S}_l = \sum_{k=2}^{l}(k-1)\delta_k$. The convergence to the bound in Eq. (5.19) can be seen, as for large l as the crosses lie above the brown dashed line, where this line shows the value of the groundstate entanglement, measured by $\tilde{\tau}_G$. The green open circles show the series $\sum_{k=2}^{l}\delta_k$ as a function of l, where $E = \sum_{k=1}^{l\to\infty}\delta_k$. **a)**, **b)** and **c)** look at the honeycomb lattice. **d)**, **e)** and **f)** looks at the square lattice. **g)**, **h)** and **i)** considers the triangular lattice. Finally **j)**, **k)** and **l)** shows the behavior on the cubic lattice. Going from left to the right $\rho = 4, 2.93$ and 2.29. 91

B.7 **a) – b)** shows the strength of the dipole connection between modes i and j. **c) – b)** show the maximal allowed pairwise tangle, for each pair of modes i and j in the trimer ground state, consistent with the associated monogamy inequalities. **c)** shows the linear three QDO arrangement and **d)** shows the triangular geometry. 92

C.1 Evolution of the symplectic trace cost function for different sizes of the harmonic chain. **a)** $d = 2$, **b)** $d = 4$, **c)** $d = 8$, **d)** $d = 16$, **e)** $d = 32$ and **f)** $d = 64$. 96
C.2 Hadamard test circuit useful for computing the real part of the expectation, $\langle\psi|U|\psi\rangle$, where U is an unitary matrix and $|\psi\rangle$ is a quantum state. The Hadmard test, in addition to preparation of $|\psi\rangle$ and a controlled U operation, requires measurement of an ancilla qubit. The probability of measuring the ancilla qubit in the computational basis state $|0\rangle$ equals $0.5(1 + \mathrm{Re}[\langle\psi|U|\psi\rangle])$ 97
C.3 Circuit implementing the block diagonal matrix $U_1 \oplus U_2$. 97
C.4 Circuit for computing $\mathrm{tr}(U)$, where U is a unitary matrix. 98
C.5 Ansatz circuit used in Fig. C.6. $U(\boldsymbol{\theta})$ example for $n = 2$ qubits. The parameters for each layer (one layer is highlighted in the box) are given by $(\boldsymbol{\theta})_l = \{\theta_l^1, \theta_l^2, .., \theta_l^n\}$, where $l \in \{1, .., L\}$. The parameters are fed into the single qubit rotation gates $R_x(\theta_l^i)$ and $R_z(\theta_l^i)$, with $i \in \{1, .., n\}$. Entanglement between qubits is generated by two qubit CNOT gates. 99
C.6 Benchmarking the hybrid VQA for solving Eq. (6.3), described in Sec. 6.4. Error in the cost function's approximation of the groundstate energy at a step s (defined as a call to the cost function) is given as $\epsilon_{E_0} = (E_0^\star - E_0)/E_0$, where E_0 is the true groundstate energy. We use the VQA to solve Eq. (3.30) with $d = 4$ (Left) $\kappa = 0.1$ and (Right) $\kappa = 0.4$. The number of layers in the ansatz (see Fig. C.5) is specified by the integer L. 100
C.7 Ansatz circuit which encodes a symplectic orthogonal matrix by design. The single qubit gates are R_y rotation gates and the two qubit entangling gates are R_{yx} rotation gates. 101

Acknowledgements

I would like to thank my supervisor, Dieter Jaksch, and Jason Crain for developing the ideas in this thesis with me. I would also like to thank my collaborators, Martin Kiffner and Joseph Tindall, for their help and guidance, as well as all the people I worked alongside during the course of my DPhil. Finally, I would like to thank my examiners, Alessio Serafini and Volker Deringer, for their constructive feedback, which helped me improve the thesis. I dedicate this thesis to my parents, Melissa and Nelson Willby.

Chapter 1

Introduction

The career of a young theoretical physicist consists of treating the harmonic oscillator in ever-increasing levels of abstraction.

Sidney Coleman

1.1 Background

Any pair of neutral atoms or molecules experiences an attraction due to the formation of transient electric dipoles. Though weaker than other forms of binding, this so-called dispersion force is the only inter-molecular interaction present in all materials: It spans a wide range of length-scales and its cumulative effects can exert decisive influence over many physical, chemical, and biological processes [1, 2, 3, 4, 5, 6, 7, 8, 9, 10]. These include stability of condensed phases in noble gases [11, 12, 13], hydrocarbons [14], molecular crystals [15, 16], nanomaterials [17, 18] as well as non-covalent binding of drugs to proteins [19, 20, 21, 22] and even the ability of geckos to climb up flat surfaces [23].

In many cases dispersion is approximated in material simulations as a pair-wise interaction attenuated by a $1/R^6$ distance dependence. However, failures of the pair-wise approximation and the importance of many-body corrections are now widely acknowledged in numerous contexts including supramolecular chemistry [24], clusters [25], low dimensional systems including layers, chains and wires [26], nanomaterials [27, 28, 29], inorganic [29] and alkaline earth compounds [30], as well as polymorphism in molecular crystals [31, 6, 32, 33]. In rare gas condensates, many-body effects can account for nearly 10% of the cohesive energy [34] and in layered systems, their contributions can be much larger [35].

The elementary picture of dispersion interactions between two particles is that of "flickering" dipole moments, arising from correlated zero-point fluctuations of the molecular or atomic charge density. However, such a model has no immediate or systematic generalization to the many-body case. Consequently, it is not known a-priori, when or why the pairwise approximation fails, when perturbative corrections will be sufficient, or whether or under what circumstances the net contributions from many-body effects will be attractive or repulsive.

Ultimately, the residual interactions governing both pairwise and many body dispersion are quantum phenomena with no classical analogue. The description of multipolar quantum fluctuations is a high-dimensional intrinsically complex many-body problem. Both pairwise and many-body dispersion would in principle be contained within an exact solution to the electronic Schrödinger equation. However in practice exact solutions to the Schrödinger equation, are not available for systems more complex then atomic Hydrogen. To tackle the important problem of finding electronic groundstates, a multiverse of approximate numerical methods [36, 37, 38, 39, 40, 41, 42, 43] have been developed, with varying trade-offs between computational cost and accuracy.

In this thesis, we model long-range many-body dispersion forces in molecular systems as assemblies of coupled quantum Drude oscillators (QDOs) [38, 44, 45, 46, 47, 48, 49, 50, 51, 52, 53, 54]. The QDO model provides a coarse-grained description, in which atoms or molecules are represented by parameterized quantum harmonic oscillators. These parameters are fitted to reproduce experimental observables of the corresponding atom or molecule, thereby offering a versatile framework capable of capturing different regions of a material's phase diagram. For instance, QDO-based models have been shown to accurately reproduce the response coefficients and gas-phase electrostatic moments of ice and liquid water [44].

The QDO framework can, in principle, describe correlated multipolar fluctuations between particles to all orders [48]. However, in practice, the dipole approximation is routinely employed. For the isotropic 3D Drude oscillators considered in this thesis, higher-order multipoles have been demonstrated to be negligible [55]. Within the dipole approximation, the QDO Hamiltonian has achieved considerable success in incorporating many-body dispersive corrections into density functionals [56], most prominently through the many-body dispersion (MBD) method [25]. The accuracy of MBD has been firmly established in the literature and benchmarked across a variety of chemical databases [57]. For example, MBD achieves a mean error within the "chemical accuracy" threshold of 1 kcal/mol for the S66 database [58], and exhibits

accuracy comparable to diffusion quantum Monte Carlo in predicting binding energies of C_{70} complexes [4].

Within the dipole approximation, the coupled QDO model is described by a quadratic Hamiltonian, whose ground state is a Gaussian state [59, 60, 61, 62, 63, 64, 65, 66, 67]. Gaussian states naturally arise whenever quadratic approximations are employed. Since their quantum statistics can be mapped to a classical stochastic system, Gaussian states admit both a computable and interpretable description in phase space. Importantly, the phase-space dimension scales only linearly with the number of subsystems or particles—rather than exponentially, as in the conventional Hilbert-space description of quantum systems. This reduced state-space representation has facilitated the development of an extensive toolkit for analyzing and solving many-body quantum problems within the Gaussian framework, particularly in quantum information theory [68, 69, 62, 70, 71, 72].

The ideas developed in this thesis originate from what may be viewed as an informational arbitrage between the literature on Gaussian states and that on molecular forces. Gaussian states have long played a central role in quantum optics and field theory, where they offer both experimental relevance and theoretical insight. Indeed, the theory of Gaussian states underpins much of the mathematical machinery of continuous-variable quantum physics [63], in which states are fundamentally classified according to their Gaussian or non-Gaussian character [73]. In this thesis, we demonstrate how Gaussian states provide an efficient and illuminating framework for the dipolar QDO model. Most prominently, we employ the theory of Gaussian states to gain new insights into the many-body character of dispersive potentials, exploiting the fundamental monogamy property of Gaussian entanglement (see Chapter 3 for a detailed discussion of entanglement monogamy).

Correlated vacuum fluctuations give rise to entangled ground states, where the state of each particle cannot be described independently of the others. Moving from the pairwise to the many-body case, however, imposes fundamental restrictions on the amount of entanglement that two particles may share within a multipartite system [74, 75, 76]. These restrictions—known as the monogamy of entanglement [77, 78, 79, 80, 81, 82, 83, 84, 85, 86]—are expressed as inequalities that place upper bounds on pairwise entanglement. Within these inequalities, the degree of shareable entanglement increases with the dimensionality of the local Hilbert space [87, 75]. For infinite-dimensional Gaussian states, this gives rise to a rich interplay between the enhancement of pairwise entanglement in multipartite settings and the limitations imposed by monogamy constraints [86]. Despite being regarded as a fundamental

property of quantum correlations, the consequences of entanglement monogamy for chemical binding remain largely unexplored. In particular, the relationship between binding energies and entanglement measures is still poorly understood, with only limited work connecting correlation energies to entropy-based quantities [88, 89, 90, 91].

Beyond providing physical insight, the Gaussian framework also enables the development of efficient variational algorithms for solving coupled QDO systems. Previous geometric approaches for extremalizing functions of Gaussian states have relied on gradient descent over the Gaussian state manifold, using Riemannian optimization techniques [92]. In this thesis, we propose an alternative formalism by formulating the variational ansatz for bosonic quadratic Hamiltonians as a constrained matrix optimization problem. Constrained matrix optimization problems are central to numerical linear algebra [93, 94, 95, 96, 97, 98]. The algorithms we develop exploit the symplectic structure of quantum phase space and therefore belong to the broader class of symplectic numerical methods [99, 100, 101, 102, 103, 104, 105].

Finally, we demonstrate how this approach can be extended to variational quantum computing, which has emerged as a leading strategy for harnessing noisy intermediate-scale quantum (NISQ) devices [106, 107, 108]. Our methods therefore contribute to the growing literature on quantum algorithms for tackling problems in computational biology [109] and non-covalent quantum chemistry [110, 111].

1.2 Publications

Chapters 2 and 3 heavy contributed to the following letter:

- 'Quantum information perspective on many-body dispersive forces'

See arXiv:2407.04111v1 [quant-ph] 4 Jul 2024. Accepted for publication in Physical Review Letters, DOI: https://doi.org/10.1103/f7yf-mxd5, 11 August, 2025.

1.3 Thesis Results

The major contribution of this thesis is to establish the role of entanglement in many-body dispersion. In particular we derive a bound on the pairwise and many-body dispersive energy contributions in terms of the reduced tangle, defined via a monogamous entanglement metric for Gaussian states. The tightness of this bound is demonstrated in both a trimer and arbitrary lattice structures. For the trimer, we partition the parameter space into a monogamous regime, where monogamy constraints suppress

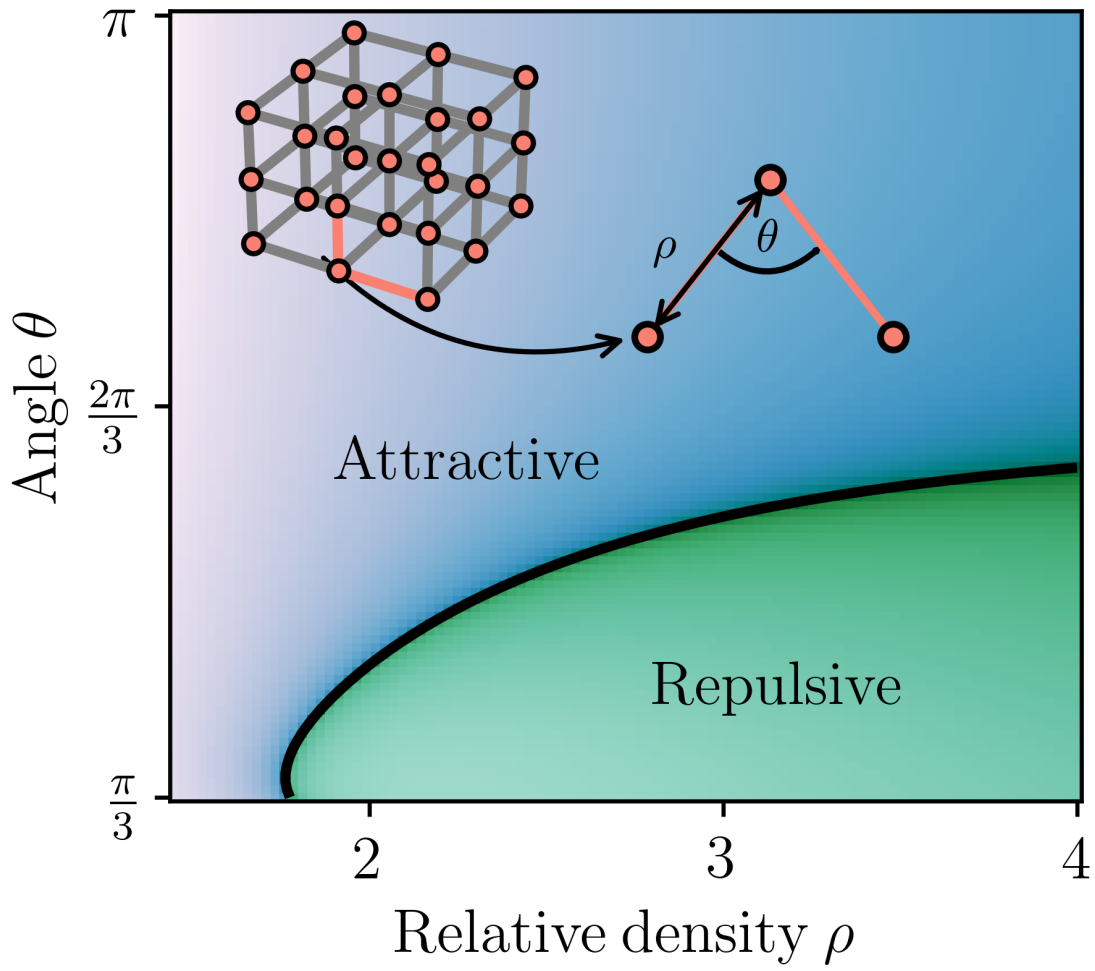

Figure 1.1: The three QDO system (trimer) captures the features of many-body dispersion on lattices. The key result of this thesis is to show how quantum information theory forecasts the breakdown pairwise dispersion forces and determines whether the many-body interactions are attractive or repulsive.

pairwise entanglement and a promiscuous regime, where the multipartite interaction allows for enhanced pairwise entanglement. The boundary separating these regimes closely aligns with the transition between repulsive and attractive many-body energy contributions, along which pairwise additivity remains valid. We further show that the relationship between monogamy constraints and many-body energy contributions persists in larger systems. Since the trimer captures key features of many-body dispersion in lattices, our findings provide a quantum information perspective on many-body energetics.

Finally, we consider how our methods and conclusions extend to realistic chemical environments. Our findings apply both to scenarios where dispersion is the sole cohesive force and to more general cases where it coexists with other forms of bonding. This generality arises because we focus on quantum fluctuations around an equilibrium configuration. While other interactions may shift the equilibrium positions, the fluctuations around these points persist. As such, our entanglement-based characterization of dispersion remains applicable across a wide range of chemical systems, from dispersion-dominated noble-gas crystals to dispersion-influenced molecular complexes.

In the second contribution of this thesis, we demonstrate that the ground states of coupled quantum Drude oscillators and, more generally, quadratic bosonic Hamiltonians can be obtained via symplectic optimization. In this framework, the symplectic matrix constraint enforces the quantum uncertainty principle. We numerically establish the efficacy of our algorithm by computing the ground states of interacting quantum dipoles arranged on a lattice. Having developed the symplectic optimization framework for Gaussian ground states, we further show how the associated cost function can be partially evaluated on a quantum computer.

1.4 Thesis Structure

The structure of this thesis is as follows:

In Chapter 2 we introduce the necessary theory, outlining the Gaussian state formalism. Chapter 3 introduces the mathematical description of entanglement monogamy, with a focus on how the monogamy property manifests in Gaussian entanglement. Entanglement's monogamy property dictates the constraints on the shareability of quantum correlations, which encompass Gaussian quantum correlations. We show how to compute monogamous entanglement monotones within the Gaussian state framework. In contrast to the qubit case, where monogamy is particularly restrictive,

Gaussian entanglement allows for a greater freedom of shareability, referred to as the simultaneous promiscuity and monogamy of Gaussian entanglement. Up until this point we have focused on explaining relevant background information, drawn from the literature on Gaussian states.

The original results of this thesis are presented from Chapter 4 onwards. In Chapter 4 we show how increasing the number of connections in coupled oscillator systems can lead to either promiscuous or monogamous entanglement distributions, depending on the properties of the Hamiltonian, illustrating the rich set of entanglement behavior in Gaussian ground states.

In Chapter 5, we show how the promiscuous or monogamous behavior of the entanglement distribution serves as a useful framework for understanding the many-body properties of dispersive bonds. We introduce the QDO model and define the many-body dispersive bond energy. We then present our analytic results, relating the entanglement distribution, to the infinite order many-body energy. Finally we use these analytic results to characterize and understand our numerical results, where we investigate the many-body energetics and entanglement in a three QDO system, chains and extended crystal lattices.

Then in Chapter 6 we focus on algorithms for finding Gaussian groundstates. We first introduce the variational principle as a constrained matrix optimization problem, before analytically showing how the uncertainty principle constraint can be efficiently enforced via symplectic matrix decompositions. We give a numerical demonstration of the efficacy of our algorithm on a lattice of interacting QDOs and then we discuss the applicability of variational quantum algorithms, for extending the method.

Finally, in the conclusion, we summarize the results of the thesis and discuss the most promising avenues of future research.

1.5 Thesis Notation

Here we will give some helpful pointers for understanding notation, which will be used throughout this thesis. In particular a large amount of this thesis will focus on matrix algebra and thus matrix notation will be key.

A diagonal matrix will be referred to as follows,

$$\mathrm{diag}(\epsilon_1, \epsilon_2, ..., \epsilon_d) = \begin{pmatrix} \epsilon_1 & 0 & \cdots & 0 & 0 \\ 0 & \epsilon_2 & \cdots & 0 & 0 \\ \vdots & \vdots & \ddots & \vdots & \vdots \\ 0 & 0 & \cdots & \epsilon_{d-1} & 0 \\ 0 & 0 & \cdots & 0 & \epsilon_d \end{pmatrix}. \tag{1.1}$$

The direct sum is defined as,

$$A \oplus B = \begin{pmatrix} A & 0 \\ 0 & B \end{pmatrix}. \tag{1.2}$$

An important class of matrices in this thesis is positive definite and positive semi-definite matrices. Formally the definition for a positive definite matrix H is

$$H > 0 \leftrightarrow \boldsymbol{x}^T H \boldsymbol{x} > 0, \forall \boldsymbol{x} \in \mathbb{R}^d \backslash \{\mathbf{0}\}, \tag{1.3}$$

where $\mathbf{0}$ is a d dimensional zero vector. Throughout $H > 0$ will be used to state that the matrix H is positive definite. Likewise a positive semi-definite matrix H is defined as

$$H \geq 0 \leftrightarrow \boldsymbol{x}^T H \boldsymbol{x} \geq 0, \forall \boldsymbol{x} \in \mathbb{R}^d \backslash \{\mathbf{0}\}. \tag{1.4}$$

As was the case with the positive definite matrices, the notation $H \geq 0$ will be used to define H as a positive semi-definite matrix.

The eigenvalues of a matrix will be written as $\lambda_i^H = \text{eig}(H)_i$, where λ_i^H is the ith eigenvalue of the matrix H. If H is a positive definite matrix the condition for $H > 0$ is equivalent to $\min(\text{eig}(H)) > 0$. Likewise if H is a positive semi-definite matrix the condition for $H \geq 0$ is equivalent to $\min(\text{eig}(H)) \geq 0$.

1.6 Computational Resources

A number of computational resources were used in the development of this thesis. For quantum circuit simulation IBMs Qiskit library [112] was used in this thesis. In addition QuTip — an open source Python-based toolbox for simulating quantum systems, was also utilized [113].

Low intensity calculations were run on a Apple laptop with an M1 chip with an 8-core CPU and 8-core GPU. Larger calculations were submitted to the University of Oxford Advanced Research Computing (ARC) facility — a high performance multi-core, multi-node computing cluster.

Chapter 2

Gaussian States

2.1 Introduction

In this chapter, we introduce the theoretical machinery required for the developments presented in the subsequent chapters. The central theme of this thesis is the application of Gaussian state theory, and we therefore begin by outlining the formalism that underpins Gaussian states.

2.2 Phase Space Representation

Gaussian states make up a subsection of continuous variable quantum states and thus have an underlying Hilbert space description. A quantum system is called a continuous-variable system when it has an infinite-dimensional Hilbert space. A general d mode or d quantum harmonic oscillator (QHO) system can be described by a Hilbert space with a tensor product structure, $\mathcal{H}^{\otimes d} = \otimes_{i=1}^{d} \mathcal{H}_i$. The quadrature field operators, for a d mode system are given by $\hat{\chi}_i$ and $\hat{\mathcal{P}}_i$, where

$$\hat{\chi}|\chi\rangle = \chi|\chi\rangle, \quad \hat{\mathcal{P}}|\mathcal{P}\rangle = \mathcal{P}|\hat{\mathcal{P}}\rangle, \tag{2.1}$$

with continuous eigenspace, $\chi \in \mathbb{R}$ and $\mathcal{P} \in \mathbb{R}$, related by a Fourier transform,

$$|\chi\rangle = \frac{1}{2\sqrt{\pi}} \int d\mathcal{P} e^{-i\chi\mathcal{P}/2} |\mathcal{P}\rangle, \quad |\mathcal{P}\rangle = \frac{1}{2\sqrt{\pi}} \int d\chi e^{i\chi\mathcal{P}/2} |\chi\rangle. \tag{2.2}$$

In addition to the quadrature operators, we can also work with bosonic field operators, which can be used to express the quadrature operators as follows,

$$\hat{\chi}_i = \frac{(\hat{a}_i^\dagger + \hat{a}_i)}{\sqrt{2}} \quad \hat{\mathcal{P}}_i = \frac{i(\hat{a}_i^\dagger - \hat{a}_i)}{\sqrt{2}}. \tag{2.3}$$

A multimodal Hilbert space $\mathcal{H}$ is spanned by the basis $\{|n\rangle\}_{n=0}^{\infty}$, known as the Fock or number basis, given by the eigenstates of the number operator $\hat{n} = \hat{a}^\dagger\hat{a}$, where $\hat{n}|n\rangle = n|n\rangle$. Over the infinite dimensional Fock space, the actions of the lowering Bosonic field operators are as follows; $\hat{a}|0\rangle = 0$ and $\hat{a}|n\rangle = \sqrt{n}|n-1\rangle, \forall n \geq 1$. Then action of the raising Bosonic field operator is $\hat{a}^\dagger|n\rangle = \sqrt{n+1}|n+1\rangle$.

For the d mode Hilbert space, we can compactly write the quadrature operators as $\hat{\boldsymbol{q}}^T = (\hat{\chi}_1, ..., \hat{\chi}_d, \hat{\mathcal{P}}_1, ..., \hat{\mathcal{P}}_d)$, where

$$\hat{\boldsymbol{q}}^T|\boldsymbol{q}\rangle = \boldsymbol{q}^T|\boldsymbol{q}\rangle, \tag{2.4}$$

thus defining a notion of *phase space*, $\boldsymbol{q} \in \mathbb{R}^{2d}$, which will allow for an efficient description of Gaussian states, without having to resort to considerations of an infinite Hilbert space. The $2d \times 2d$ matrix σ, known as the *symplectic* matrix, encodes the canonical commutation relations or CCR,

$$\sigma = \begin{pmatrix} 0 & \mathbb{1} \\ -\mathbb{1} & 0 \end{pmatrix}, \tag{2.5}$$

where

$$[\hat{\boldsymbol{q}}_i, \hat{\boldsymbol{q}}_j] = \mathrm{i}\sigma_{ij}, \tag{2.6}$$

with $\hbar = 1$ and for $i, j \in \{1, .., d\}$. The symplectic matrix has the following properties

$$\sigma = -\sigma^T, \quad \sigma^2 = -\mathbb{1}_{2d} \tag{2.7}$$

and thus $\sigma^T\sigma = -\sigma^2 = \mathbb{1}_{2d}$.

Whilst throughout this thesis we will mainly use the representation of the symplectic matrix in Eq. (2.5) an alternate representation is possible via a reordering of the position-momentum operator, which will be used for certain proofs and definitions for convenience. The position-momentum operator can be written as $\hat{\boldsymbol{s}}^T = (\hat{\chi}_1, \hat{\mathcal{P}}_1 ..., \hat{\chi}_d, \hat{\mathcal{P}}_d)$. The commutation relations and thus the symplectic matrix are thus further expressible as

$$[\hat{\boldsymbol{s}}_i, \hat{\boldsymbol{s}}_j] = \mathrm{i}\boldsymbol{\Omega}_{ij}, \quad \text{where} \quad \boldsymbol{\Omega} = \bigoplus_{i=1}^{d} w, \quad w = \begin{pmatrix} 0 & 1 \\ -1 & 0 \end{pmatrix}. \tag{2.8}$$

The matrix $\boldsymbol{\Omega}$ is an alternate representation of the symplectic matrix, which further obeys the same properties as σ in Eq. (2.7). The vector of ladder operators $\hat{\boldsymbol{a}} = (\hat{a}_1, \hat{a}_1^\dagger, ..., \hat{a}_d, \hat{a}_d^\dagger)^T$ is related to $\hat{\boldsymbol{s}}$ via a unitary transform

$$\tilde{U} = \bigoplus_{i=1}^{d} \tilde{u}, \quad \text{where} \quad \tilde{u} = \frac{1}{\sqrt{2}} \begin{pmatrix} 1 & \mathrm{i} \\ 1 & -\mathrm{i} \end{pmatrix}, \tag{2.9}$$

such that the CCR are recast as,

$$[\hat{\boldsymbol{a}}, \hat{\boldsymbol{a}}^\dagger] = [\tilde{U}\hat{\boldsymbol{s}}, \hat{\boldsymbol{s}}^\dagger\tilde{U}^\dagger] = \tilde{U}[\hat{\boldsymbol{s}}, \hat{\boldsymbol{s}}^\dagger]\tilde{U}^\dagger = \mathrm{i}\tilde{U}\boldsymbol{\Omega}\tilde{U}^\dagger = \bigoplus_{i=1}^{d}\sigma_z, \quad \sigma_z = \begin{pmatrix} 1 & 0 \\ 0 & -1 \end{pmatrix}. \tag{2.10}$$

Here σ_z is the Pauli z matrix and Eq. (2.10) has been taken from [63].

2.2.1 Quadractic Hamiltonians

Ground and thermal states of quadratic Hamiltonians are Gaussian states, having a Gaussian Wigner distribution in phase space. A quadratic bosonic Hamiltonian can be written as

$$\hat{H} = \frac{1}{2}\hat{\boldsymbol{q}}^T H \hat{\boldsymbol{q}} \quad H > 0, \tag{2.11}$$

Note that in this thesis we shall neglect quadratic Hamiltonians with a linear component. The $2d \times 2d$ matrix H is constrained to be a positive definite matrix $H > 0$ and thus $\min\left[\mathrm{eig}(H)_i\right] > 0$. The Hamiltonian matrix H (not to be confused with the Hamiltonian operator $\hat{H}$), can be written in block-matrix form as

$$H = \begin{pmatrix} H_\chi & H_{\chi,\mathcal{P}} \\ H_{\chi,\mathcal{P}}^T & H_\mathcal{P} \end{pmatrix}, \tag{2.12}$$

where sub-block H_χ couples QHOs in position space, $H_{\chi,\mathcal{P}}$ describes coupling between position and momentum operators and $H_\mathcal{P}$ describes momentum-momentum QHO couplings. Note that the block matrix form of H arises from the ordering of the position-momentum vector and thus the form of the symplectic matrix in Eq. (2.5).

2.3 Correlation Matrix and Symplectic Diagonalization

2.3.1 Gaussian density matrices

The set of valid density matrices on the Hilbert space $\mathcal{H}$, have the following properties:

$$\hat{\rho} = \hat{\rho}^\dagger \quad \textit{self adjoint} \tag{2.13}$$

$$\hat{\rho} \geq 0 \quad \textit{positive} \tag{2.14}$$

$$tr(\hat{\rho}) = 1 \quad \textit{normalized.} \tag{2.15}$$

These conditions must be met for density matrices describing Gaussian states. Gaussian states are defined as all the ground and thermal states of quadratic Hamiltonians

with positive definite Hamiltonian matrix. A Gaussian state density matrix can be written as

$$\hat{\rho} = \frac{e^{-\beta \hat{H}}}{\mathrm{tr}\left[e^{-\beta \hat{H}}\right]}, \tag{2.16}$$

where $\beta \in \mathbb{R}^+$ and $\hat{H}$ is defined in Eq. (2.11) [63].

2.3.2 Gaussian correlation matrices

Gaussian states are completely characterized by their first moments, and a correlation matrix (CM) of two point correlation functions [61, 114, 115]. The consideration of the first moments are neglected here, i.e $\langle \hat{\boldsymbol{q}}_i \rangle = 0 \ \forall i \in \{1, .., 2d\}$, as they do not effect the Gaussian entanglement [61]. The CM of two point correlation functions is described here by the $2d \times 2d$ matrix γ, an element of which is given in terms of the (Gaussian) density matrix as [116]

$$\begin{aligned} \gamma_{ij} &= \mathrm{tr}\left[\hat{\rho}\{\hat{\boldsymbol{q}}_i, \hat{\boldsymbol{q}}_j\}^+\right] \\ &= \mathrm{tr}\left[\hat{\rho}\hat{\boldsymbol{q}}_i\hat{\boldsymbol{q}}_j\right] - \sigma_{ij}, \quad \forall i, j = 1, .., 2d \end{aligned} \tag{2.17}$$

The CM γ is a real, symmetric, $2d \times 2d$ matrix. The uncertainty principle on the quadratures given in Eq. (2.6) can be written in matrix form, in the so-called Robertson-Schrödinger uncertainty relation, a multimodal matrix representation of the Heisenberg uncertainty principle,

$$\gamma + \mathrm{i}\sigma \geq 0. \tag{2.18}$$

This inequality, encapsulates both the CCR and the necessary constraints on the density matrix $\hat{\rho}$, given in Eq. (2.13). The constraint on the CM, given in Eq. (2.18) distinguishes it from the CM of a multivariate Gaussian probability distribution. A symmetric matrix describing the latter is solely constrained to be positive definite. Note that Eq. (2.18), contains within it the positive definite constraint on γ, making all quantum Gaussians, also valid classical Gaussian distributions [117]. The quantum statistics, determined by the CM, are described by the quasi-probability distribution known as the Wigner function,

$$W(q) = \frac{e^{-\frac{1}{2}\boldsymbol{q}\gamma^{-1}\boldsymbol{q}^T}}{\pi\sqrt{\mathrm{Det}(\gamma)}}. \tag{2.19}$$

Here $\boldsymbol{q}$ is the phase space vector, defined in Eq. (2.4). A pure state is guaranteed to be Gaussian if it has a non-negative Wigner function [118]. Note that any density operator has an equivalent representation in terms of a quasi-probability distribution

i.e Wigner function, but only Gaussian states, have Winger functions, which describe classical probability distributions, in the form of Eq. (2.19).

The positivity constraint on the density matrix in Eq. (2.13) is enforced in phase space by the Robertson-Schrödinger uncertainty relation on the CM. For a *pure* Gaussian state, with CM given by γ_p, we have the following extra condition on the CM [119],

$$\mathrm{Det}(\gamma_p) = 1 \leftrightarrow (\gamma_p \sigma)^2 = -\mathbb{1}_{2d}. \tag{2.20}$$

This condition provides a general parameterization for pure state CMs:

Lemma. 1 .- A real symmetric matrix γ_p is the covariance matrix of a pure Gaussian state of d modes iff there exist real symmetric $d \times d$ matrices X and Y with $X > 0$ such that,

$$\gamma_p = \begin{pmatrix} X & XY \\ YX & YXY + X^{-1} \end{pmatrix}, \quad \text{where} \quad X > 0,\ Y = Y^T \ \& \ X = X^T. \tag{2.21}$$

Proof.- See [119].

2.3.3 Gaussian variational principle

The variational principle states that the ground state energy is always less than or equal to the expectation value of the time-independent Hamiltonian with respect to a normalized trial wavefunction. Using the standard definition of the variational principle, expressed in terms of the density matrix, we can formulate the principle for a quadratic bosonic Hamiltonian—i.e., a Hamiltonian of the form given in Eq. (2.11)—as follows [61],

$$\begin{aligned} E_0 &= \inf_{\gamma} \ \tfrac{1}{4}\,\mathrm{tr}(\gamma H) \quad \text{s.t.} \quad \gamma + \mathrm{i}\sigma \geq 0, \\ \gamma_0 &= \arg\inf_{\gamma} \ \tfrac{1}{4}\,\mathrm{tr}(\gamma H) \quad \text{s.t.} \quad \gamma + \mathrm{i}\sigma \geq 0. \end{aligned} \tag{2.22}$$

The constraint $\gamma + \mathrm{i}\sigma \geq 0$, enforces the uncertainty principle, hence ensuring the argument to Eq. (2.22) represents a valid CM. The Gaussian groundstate is fully represented by the groundstate CM, given by γ_0.

2.3.4 Symplectic diagonalization

A matrix which preserves the CCR and thus σ under a transformation is a symplectic matrix [63], belonging to the symplectic matrix group,

$$S\sigma S^T = \sigma \quad S \in \mathcal{S}_p(\dim(2d, \mathbb{R}). \tag{2.23}$$

The inverse of a symplectic matrix is given by

$$S^{-1} = \sigma^{-1} S^T \sigma. \tag{2.24}$$

The product of two symplectic matrices is also symplectic and the determinant of any symplectic matrix is 1, i.e $\mathrm{Det}(S) = 1$.

Williamson's theorem [120] states there is always a symplectic matrix, which brings the positive definite matrix H into diagonal form,

$$SHS^T = \begin{pmatrix} \epsilon_1 & 0 & \cdots & 0 & 0 \\ 0 & \epsilon_1 & \cdots & 0 & 0 \\ \vdots & \vdots & \ddots & \vdots & \vdots \\ 0 & 0 & \cdots & \epsilon_d & 0 \\ 0 & 0 & \cdots & 0 & \epsilon_d \end{pmatrix}, \tag{2.25}$$

where ϵ_i are the symplectic eigenvalues of H, each repeated once along the diagonal. The ground state energy of $\hat{H}$ is given by the sum of the symplectic eigenvalues [61, 63],

$$E_0 = \frac{1}{2}\sum_{i=1}^{d} \epsilon_i = \frac{1}{4}\mathrm{tr}(SHS^T). \tag{2.26}$$

The symplectic eigenvalues are computable from the Hamiltonian matrix and σ as [117, 61],

$$\epsilon_i = \sqrt{\mathrm{eig}_i(\sigma H \sigma^T H)}, \quad \text{or} \quad \epsilon_i = \mathrm{eig}_i(|\mathrm{i}\sigma H|). \tag{2.27}$$

As the type of Hamiltonian we mainly focus on in this thesis is in the form $H = H_\chi \oplus \mathbb{1}$, $\epsilon_i = \sqrt{\mathrm{eig}_i(\sigma H \sigma^T H)} = \sqrt{\mathrm{eig}_i(H_\chi \oplus H_\chi)}$. As a result the unique symplectic eigenvalues of Hamiltonians of this form are $\epsilon_i = \sqrt{\lambda_i^{H\chi}}$.

Proof .- Applying the converse of symplectic diagonalization and using the expression for the symplectic matrix inverse in Eq. (2.24), we obtain

$$\mathrm{i}\mathbf{\Omega} H = \mathrm{i}\mathbf{\Omega} S^{-1} \mathrm{diag}(\epsilon_1, \epsilon_1, \ldots, \epsilon_d, \epsilon_d) S^{T-1} = \mathrm{i} S^T \mathbf{\Omega} \mathrm{diag}(\epsilon_1, \epsilon_1, \ldots, \epsilon_d, \epsilon_d) S^{T-1}, \tag{2.28}$$

where the Hamiltonian matrix H is ordered consistently with the form of the symplectic matrix $\mathbf{\Omega}$ defined in Eq. (2.8).

The unitary matrix $\tilde{U}$, defined in Eq. (2.9), which relates the canonical operators to the creation/annihilation operators, diagonalizes the symplectic matrix $\mathbf{\Omega}$, as shown in Eq. (2.10). Using Eq. (2.10), we can therefore rewrite Eq. (2.28) as

$$\mathrm{i}\mathbf{\Omega} H = \mathrm{i} S^T \mathbf{\Omega} \mathrm{diag}(\epsilon_1, \epsilon_1, \ldots, \epsilon_d, \epsilon_d) S^{T-1} = S^T \tilde{U}^\dagger \bigoplus_{i=1}^{d} \epsilon_i \sigma_z \tilde{U} (S^T)^{-1}, \tag{2.29}$$

where σ_z is the Pauli-z matrix, defined in Eq. (2.10).

Since $(\tilde{U}(S^T)^{-1})^{-1} = S^T\tilde{U}^\dagger$, Eq. (2.29) gives the eigendecomposition of $i\mathbf{\Omega}H$. This shows that the absolute values of the eigenvalues of $i\mathbf{\Omega}H$ are precisely the symplectic eigenvalues ϵ_i.

In addition to H, the CM, by virtue of being a positive matrix, is amenable to symplectic diagonalization,

$$S\gamma S^T = \begin{pmatrix} \nu_1 & 0 & \cdots & 0 & 0 \\ 0 & \nu_1 & \cdots & 0 & 0 \\ \vdots & \vdots & \ddots & \vdots & \vdots \\ 0 & 0 & \cdots & \nu_d & 0 \\ 0 & 0 & \cdots & 0 & \nu_d \end{pmatrix}, \tag{2.30}$$

where S is a symplectic transformation, which diagonalizes the matrix γ. Using the definition of a symplectic matrix, the Robertson-Schrödinger uncertainty relation in Eq. (2.18), can be written in terms of the symplectic eigenvalues of the CM,

$$\mathrm{diag}(\nu_1, .., \nu_d) \oplus \mathrm{diag}(\nu_1, .., \nu_d) + i\sigma \geq 0, \tag{2.31}$$

which results in the uncertainty principle constraint on the CM being expressed as,

$$\nu_i \geq 1, \quad \forall i \in \{1, .., d\}. \tag{2.32}$$

This condition determines whether γ represents a valid CM, in terms of it's symplectic eigenvalues and is equivalent to Eq. (2.18).

The condition for γ to describe a pure-state CM is given in Eq. (2.20). Using the symplectic eigendecomposition of the CM, and recalling Eq. (2.30), the condition for γ_p in Eq. (2.20) can be expressed in terms of the symplectic eigenvalues as

$$\nu_i = 1, \quad \forall i \in \{1, \ldots, d\}. \tag{2.33}$$

2.3.5 Block diagonal Hamiltonians

For Hamiltonian matrices of the form $H = H_\chi \oplus \mathbb{1}$, the ground state CM can be efficiently computed in time complexity $\mathcal{O}(d^3)$, using the formulae given in [61, 119, 62, 121, 70],

$$\gamma_0 = H_\chi^{-1/2} \oplus H_\chi^{1/2}. \tag{2.34}$$

where the matrix square root is given by

$$H_\chi^{\pm 1/2} = O_{H_\chi} \mathrm{diag}\left(\left(\sqrt{\lambda_1^{H_\chi}}\right)^{\pm 1}, .., \left(\sqrt{\lambda_d^{H_\chi}}\right)^{\pm 1}\right) O_{H_\chi}^T. \tag{2.35}$$

Note that O_{H_χ} is the orthogonal matrix that diagonalizes H_χ, i.e $O_{H_\chi} \in SO(d, \mathbb{R})$ and $H_\chi^{-1/2} = (H_\chi^{1/2})^{-1}$ is the inverse matrix of $H_\chi^{1/2}$, which is always computable as $H_\chi^{1/2}$ is a non-singular matrix, given the positive definite constraint on H in Eq. (2.11).

Proof.- Using the expression for the symplectic eigenvalue decomposition in Eq. (2.27) and the definition of the matrix square root given in Eq. (2.35), we write the symplectic eigenvalues of H as

$$\begin{aligned}\epsilon_i &= \sqrt{\mathrm{eig}_i(\sigma(H_\chi \oplus \mathbb{1})\sigma^T(H_\chi \oplus \mathbb{1}))} = \sqrt{\mathrm{eig}_i(H_\chi \oplus H_\chi)} \\ &= \mathrm{eig}_i\Big(\sqrt{H_\chi} \oplus \sqrt{H_\chi}\Big) = \mathrm{eig}_i\Big(H_\chi^{1/2} \oplus H_\chi^{1/2}\Big). \end{aligned} \tag{2.36}$$

Note that $O_{H_\chi} \oplus O_{H_\chi} \in \mathcal{S}_p(2d, \mathbb{R})$, thus constituting a valid CCR-preserving transformation of H. Moreover, $O_{H_\chi} \oplus O_{H_\chi}$ brings the matrix $H_\chi^{1/2} \oplus H_\chi^{1/2}$ into diagonal form, as per Eq. (2.35).

We can therefore use the expression for the ground state energy in terms of the sum of the symplectic eigenvalues from Eq. (2.26), together with the cyclic property of the trace, as follows:

$$E_0 = \frac{1}{2}\sum_{i=1}^{d} \epsilon_i = \frac{1}{4}\sum_{i}^{2d} \mathrm{eig}_i\Big(H_\chi^{1/2} \oplus H_\chi^{1/2}\Big) = \mathrm{tr}\Big(H_\chi^{1/2} \oplus H_\chi^{1/2}\Big). \tag{2.37}$$

The ground state CM, γ_0, is defined using the variational principle in Eq. (2.22). By equating the expression for the ground state energy obtained from symplectic diagonalization with that in Eq. (2.22), we find

$$E_0 = \tfrac{1}{4}\mathrm{tr}\left(\gamma_0 \underbrace{H_\chi \oplus \mathbb{1}}_{H}\right) = \tfrac{1}{4}\mathrm{tr}\Big(H_\chi^{1/2} \oplus H_\chi^{1/2}\Big). \tag{2.38}$$

Due to the uniqueness of the ground state, it follows that in order to satisfy Eq. (2.38), the ground state CM γ_0 must take the form given in Eq. (2.34).

2.4 Conclusion

In this chapter, we have gone over key aspects of the theory of Gaussian states. Crucially we have shown how the ground state CM, containing all of the relevant information in the ground state wavefunction, can be efficiently computed with polynomial scaling algorithms. We further showed the usefulness of symplectic methods, for decomposing quadratic bosonic Hamiltonians and their associated ground state CMs. In the next chapter we will utilize the compact representation of the Gaussian ground state, to compute entanglement monotones as a function of CM matrix elements.

Chapter 3

Entanglement Monogamy

3.1 Introduction

Quantum entanglement, a cornerstone of quantum mechanics and a central concept in quantum information theory, underpins many phenomena that distinguish quantum from classical physics and forms the basis for numerous quantum technologies, including quantum computation [122], quantum cryptography [123], and quantum teleportation [124].

Preparing a state with only local operations and classical communication (LOCC), i.e. by allowing local quantum operations supplemented with classical communication of measurement outcomes between parties [125], yields states that are only classically correlated, known as separable states. LOCC is a key concept because it encapsulates the practical limitations of manipulating quantum systems when distant parties are restricted to local interventions and classical messaging [125]. By definition, entangled states cannot be generated from separable states using only LOCC.

A striking and distinguishing property of quantum entanglement is that it cannot be freely shared among arbitrarily many parties; in other words, it is monogamous. This feature, closely related to the no-cloning theorem, highlights a sharp departure from classical correlations and stands as a distinctly quantum phenomenon. The quantitative formulation of entanglement monogamy is captured by monogamy inequalities. The first such inequality, known as the CKW inequality after Coffman, Kundu, and Wootters, was established for three-qubit systems using the entanglement measure called the tangle [77]. This result was subsequently extended to d-qubit systems [78] and to CV Gaussian states [79], with further generalizations later developed using a variety of entanglement measures [126, 127, 128, 129].

3.2 Qubit Monogamy

Consider a d qubit system. The d qubit ground state density matrix is a $2^d \times 2^d$ matrix, denoted by $\hat{\rho}^d$. The superscript on the qubit density matrix, distinguishes it as a finite dimensional matrix, given that $d \neq \infty$. This is in comparison to the infinite dimensional density matrices, (indirectly) considered mostly in this thesis.

The tangle between qubit i and $d-1$ qubits, i.e for a bipartition of the form $i : \underbrace{k, l, j, .., m}_{d-1}$, is given in terms of the concurrence, another entanglement monotone [77, 78] as

$$\tau(i) = \mathcal{C}^2(i) = 4\mathrm{Det}(\hat{\rho}_i^d) \in [0, 1], \tag{3.1}$$

where $\hat{\rho}_i^d$ is the reduced density matrix of the ith qubit, computed via tracing out modes $k, l, j, .., m$. Note that the tangle is given by a non-negative real number between 0 and 1.

The pairwise entanglement between qubits i and j is denoted by $\tau(i : j)$, which we proceed to outline how to compute. Let $\hat{\rho}_{ij}^d$ denote the two qubit reduced density matrix of qubits i and j, tracing over modes $k, l, .., m$, in the d qubit system. Defining,

$$(\hat{\rho}_{ij}^d)' = (\sigma_y \otimes \sigma_y)(\hat{\rho}_{ij}^d)^\star(\sigma_y \otimes \sigma_y), \tag{3.2}$$

where σ_y is the y Pauli gate, $\sigma_y = \begin{pmatrix} 0 & -\mathrm{i} \\ \mathrm{i} & 0 \end{pmatrix}$ and $(\hat{\rho}_{ij}^d)^\star$ is the complex conjugate of $\hat{\rho}_{ij}^d$. By computing

$$\lambda_i' = \sqrt{\mathrm{eig}_i\left((\hat{\rho}_{ij}^d)^\star(\hat{\rho}_{ij}^d)'\right)}, \quad \forall i \in \{1, 2, 3, 4\}, \tag{3.3}$$

where $\lambda_1' \geq \lambda_2' \geq \lambda_3' \geq \lambda_4'$, the pairwise tangle between qubits i and j is given as [77],

$$\tau(i : j) = \left[\max\{\lambda_1' - \lambda_2' - \lambda_3' - \lambda_4', 0\}\right]^2 \in [0, 1]. \tag{3.4}$$

The d qubit monogamy inequality is then given as

$$\tau(i) \geq \sum_{j=1}^{d} \tau(i : j), \forall j \neq i, \quad \text{where} \quad \begin{cases} \tau(i) \in [0, 1], \forall i \\ \tau(i : j) \in [0, 1], \forall i \neq j. \end{cases} \tag{3.5}$$

To intuitively understand monogamy restrictions, consider the $d = 3$ monogamy inequality, as first derived by Coffman, Kundu, and Wootters [77]:

$$\tau(1) \geq \tau(1 : 2) + \tau(1 : 3). \tag{3.6}$$

If qubits 1 and 2 share maximal entanglement, i.e., $\tau(1 : 2) = 1$, then for the monogamy inequality to hold we must have $\tau(1 : 3) = 0$, as the three-qubit monogamy equality

saturates and is given by $\tau(1) = \tau(1:2)$. Conversely, if qubits 1 and 3 are prepared in a maximally entangled state, then qubits 1 and 2 must be unentangled, i.e., $\tau(1) = \tau(1:3)$ and $\tau(1:2) = 0$. This highlights the necessity for trade-offs in entanglement sharing in multipartite systems.

3.3 Gaussian Tangle

We quantify the entanglement present in the ground state of a quadratic bosonic Hamiltonian by the Gaussian tangle which is an entanglement measure, i.e vanishing for separable states and non-increasing under local operations and classical communication (LOCC), with a verifiable monogamy property [79, 130]. The tangle quantifies the entanglement in a bipartition between mode i and the other $d-1$ modes in the system,

$$\tau_G(i) = \frac{1}{4}\left(\|\hat{\rho}^{T_i}\|_1 - 1\right)^2, \quad \text{where} \quad \tau_G(i) \in [0, \infty], \tag{3.7}$$

and $\hat{\rho}$ is a *pure* density matrix of a Gaussian state and $\hat{\rho}^{T_i}$ is the partial transpose with respect to the ith mode. Unlike the qubit tangle discussed in the previous section, $\tau_G(i)$ is unbounded due to the infinite-dimensional nature of CV systems. Throughout this work, the considered bi-partition is always of the form $(i|\text{rest})$, i.e. between a single mode and the remaining $d-1$ modes.

Computing the Gaussian tangle requires performing a partial transposition of the density matrix. The positivity of the partial transpose (PPT) criterion provides a condition for separability [131, 132]. Satisfying this criterion guarantees the absence of entanglement across the considered bipartition. In particular, the PPT criterion is both necessary and sufficient for separability in two-mode Gaussian states [132], as well as when the bipartition is between a single mode and an arbitrary collection of other modes [133]. Interestingly, the criterion can fail to characterize separability for more general bipartitions [133].

The positivity of the density matrix can be expressed in terms of the CM γ via the Robertson–Schrödinger uncertainty relation, see Eq. (2.18). For a d-mode system, the PPT criterion between mode i and the remaining $d-1$ modes is given by

$$\tilde{\gamma}_i + \mathrm{i}\sigma \geq 0, \tag{3.8}$$

where $\tilde{\gamma}_i$ is the partially transposed CM corresponding to the density matrix $\hat{\rho}^{T_i}$. Partition transposition acts on the quadratures as $\hat{\chi} \to \hat{\chi}$ and $\hat{\mathcal{P}} \to -\hat{\mathcal{P}}$ [63]. Consequently, applying partial transposition to the CM amounts to the transformation [79, 72]

$$\tilde{\gamma}_i = F_i \gamma F_i, \tag{3.9}$$

where the definition of F_i depends on the form of the CM under consideration. For example, for the symplectic matrix in canonical form [Eq. (2.5)],

$$F_1 = \mathrm{diag}(\underbrace{1,1,1,\ldots,1}_{d},\underbrace{-1,1,1,\ldots,1}_{d}). \tag{3.10}$$

In comparison using the symplectic matrix in Eq. (2.8), $F_1 = \mathrm{diag}(\underbrace{1,-1,1,1,..,1}_{2d})$.

The smallest symplectic eigenvalue of the partially transposed CM $\tilde{\gamma}_i$ is denoted by $(\tilde{\nu}_-)_i$. Recall that the condition in Eq. (2.18) is equivalent to Eq. (2.32), the latter being expressed in terms of symplectic eigenvalues. These eigenvalues can be straightforwardly computed using the symplectic diagonalization technique outlined in Sec. 2.3.4. In particular, the minimum symplectic eigenvalue of the partially transposed state is given by

$$(\tilde{\nu}_-)_i = \min\big(|\mathrm{eig}(\mathrm{i}\sigma\tilde{\gamma}_i)|\big). \tag{3.11}$$

We proceed to show, from the Gaussian state literature, necessary conditions for a two mode (mixed or pure) Gaussian state to share entanglement and give the formulae, in terms of the CM matrix elements for Eq. (3.7). This analysis of the two mode state, provides a general formulae for $\|\hat{\rho}^{T_i}\|_1$ in terms of the diagonal CM matrix elements. Note that throughout this section we will consider block diagonal CMs, of the form in Eq. (2.34).

3.3.1 Gaussian tangle in a two mode state

3.3.1.1 Standard form

Consider a two mode CM, using the quadrature ordering based on the form of the symplectic matrix in Eq. (2.8),

$$\gamma = \begin{pmatrix} \langle\hat{\chi}_1^2\rangle & 0 & \langle\hat{\chi}_1\hat{\chi}_2\rangle & 0 \\ 0 & \langle\hat{\mathcal{P}}_1^2\rangle & 0 & \langle\hat{\mathcal{P}}_1\hat{\mathcal{P}}_2\rangle \\ \langle\hat{\chi}_1\hat{\chi}_2\rangle & 0 & \langle\hat{\chi}_2^2\rangle & 0 \\ 0 & \langle\hat{\mathcal{P}}_1\hat{\mathcal{P}}_2\rangle & 0 & \langle\hat{\mathcal{P}}_2^2\rangle \end{pmatrix}. \tag{3.12}$$

Any two-mode CM can be transformed into *standard form* by local transformations which act on the CM to produce the CM in standard form

$$\gamma_{\mathrm{sf}} = \begin{pmatrix} a & 0 & c_+ & 0 \\ 0 & a & 0 & c_- \\ c_+ & 0 & b & 0 \\ 0 & c_- & 0 & b \end{pmatrix}, \quad \text{with} \quad c_+ \geq c_-. \tag{3.13}$$

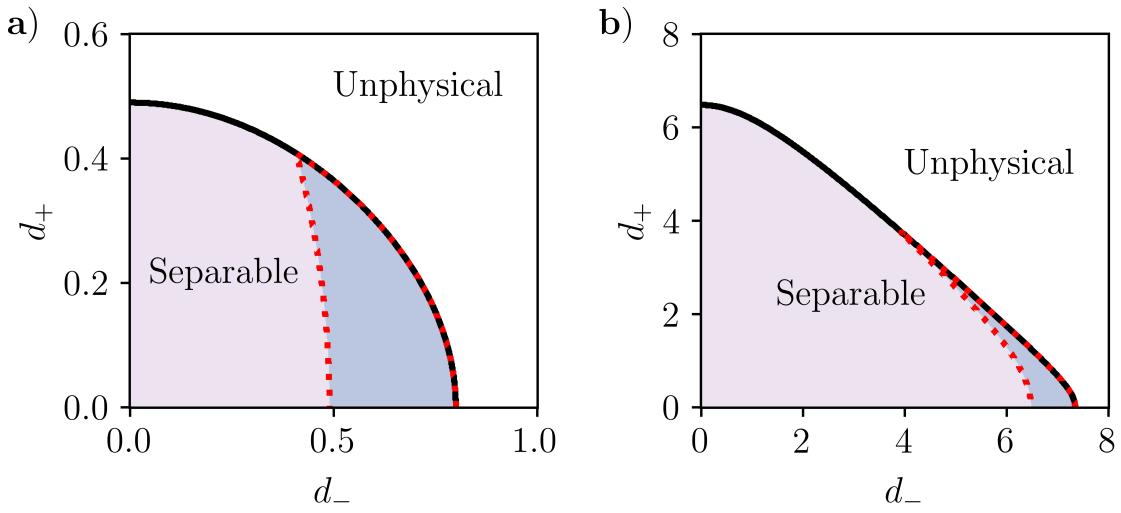

Figure 3.1: Regions enclosed by the black line, show valid two modes CMs, where $\mathbf{\Delta} < 1 + \det(\gamma)$ and thus the Robertson-Schrödinger relation (uncertainty principle) relation is obeyed. The darker shaded regions enclosed by the red dotted lines, shows the portion of valid two mode CMs which exhibit entanglement. This condition is given by $\tilde{\mathbf{\Delta}} > 1 + \det(\gamma)$. In a) $a = 2.2$ and $b = 1.1$, whereas in b) $a = 8$ and $b = 4$.

Here the real parameters a, b, c_+, c_- are *local symplectic invariants*,

$$a^2 = \langle \hat{\chi}_1^2 \rangle \langle \hat{\mathcal{P}}_1^2 \rangle, \qquad b^2 = \langle \hat{\chi}_2^2 \rangle \langle \hat{\mathcal{P}}_2^2 \rangle, \qquad c_+ c_- = \langle \hat{\chi}_1 \hat{\chi}_2 \rangle \langle \hat{\mathcal{P}}_1 \hat{\mathcal{P}}_2 \rangle. \tag{3.14}$$

The standard form of a two mode CM is unique, with the symplectic invariants a, b, c_+, c_- uniquely determining the entanglement information of the two mode state.

Note that using the representation of the symplectic matrix in Eq. (2.5), i.e. σ instead of $\mathbf{\Omega}$, we can write the two-mode CM as

$$\gamma = \begin{pmatrix} \langle \hat{\chi}_1^2 \rangle & \langle \hat{\chi}_1 \hat{\chi}_2 \rangle & 0 & 0 \\ \langle \hat{\chi}_1 \hat{\chi}_2 \rangle & \langle \hat{\chi}_2^2 \rangle & 0 & 0 \\ 0 & 0 & \langle \hat{\mathcal{P}}_1^2 \rangle & \langle \hat{\mathcal{P}}_1 \hat{\mathcal{P}}_2 \rangle \\ 0 & 0 & \langle \hat{\mathcal{P}}_1 \hat{\mathcal{P}}_2 \rangle & \langle \hat{\mathcal{P}}_2^2 \rangle \end{pmatrix}. \tag{3.15}$$

In its standard form, this can then be expressed as [63],

$$\gamma_{\text{sf}} = \begin{pmatrix} a & c_+ & 0 & 0 \\ c_+ & b & 0 & 0 \\ 0 & 0 & a & c_- \\ 0 & 0 & c_- & b \end{pmatrix}, \quad \text{with} \quad c_+ \geq c_-. \tag{3.16}$$

Proof .- The existence of the standard form for any two-mode covariance matrix follows from the action of a symplectic transformation on γ of the form,

$$\gamma_{\text{sf}} = (O \oplus O) S_{\text{sf}} \gamma S_{\text{sf}}^T (O \oplus O)^T, \qquad S_{\text{sf}} \in \text{Sp}(4, \mathbb{R}), \quad O \in SO(2, \mathbb{R}). \tag{3.17}$$

The symplectic transformation $S_{\rm sf}$ is given by a direct sum of 2×2 local symplectic matrices i.e $S_{\rm sf} = S_1 \oplus S_2$. The 2×2 matrices S_1, S_2 and O, can always be chosen, to transform the CM into its standard form. Note that $S_{\rm sf}$ is a real symplectic matrix, i.e. $S_{\rm sf} \in {\rm Sp}(4,\mathbb{R})$, as $S_1 \oplus S_2$ is symplectic by virtue of the local symplectic matrices S_1 and S_2, and $O \oplus O$ can always be shown to be symplectic for local orthogonal blocks.

By Williamson's theorem, every positive-definite matrix can be brought into diagonal form via a symplectic transformation. In particular, the single-mode reduced CMs, ${\rm diag}(\langle\hat{\chi}_1^2\rangle, \langle\hat{\mathcal{P}}_1^2\rangle)$ and ${\rm diag}(\langle\hat{\chi}_2^2\rangle, \langle\hat{\mathcal{P}}_2^2\rangle)$, can be transformed to their Williamson normal forms via S_1 and S_2, respectively, as $a\mathbb{1}_2$ and $b\mathbb{1}_2$, where a and b are the symplectic eigenvalues, each repeated once along the diagonal. The off-diagonal blocks transform under the symplectic transformation in Eq. (3.17) as

$$ {\rm diag}(\langle\hat{\chi}_1\hat{\chi}_2\rangle, \langle\hat{\mathcal{P}}_1\hat{\mathcal{P}}_2\rangle) \to O S_1\, {\rm diag}(\langle\hat{\chi}_1\hat{\chi}_2\rangle, \langle\hat{\mathcal{P}}_1\hat{\mathcal{P}}_2\rangle) S_2^T O^T, \tag{3.18} $$

which can always be made diagonal by choosing a 2×2 orthogonal matrix O to perform the singular value decomposition of the matrix $S_1\, {\rm diag}(\langle\hat{\chi}_1\hat{\chi}_2\rangle, \langle\hat{\mathcal{P}}_1\hat{\mathcal{P}}_2\rangle) S_2^T$.

3.3.1.2 Detecting two mode entanglement

The symplectic spectrum of the two mode state is given by $\{\nu_+, \nu_+, \nu_-, \nu_-\}$, following from Eq. (2.30). Any two mode Gaussian state can be written as $S\gamma S^T$ for some $S \in \mathcal{S}_p(4,\mathbb{R})$, with two unique symplectic eigenvalues $\nu_\pm$, where $\nu_+ \geq \nu_-$.

The symplectic spectrum is computable in terms of the symplectic invariants as [134, 135],

$$ \nu_\pm = \sqrt{\frac{\mathbf{\Delta} \pm \sqrt{\mathbf{\Delta}^2 - 4{\rm Det}(\gamma)}}{2}}, \tag{3.19} $$

where $\mathbf{\Delta} = a^2 + b^2 + 2c_+c_-$ and ${\rm Det}(\gamma) = (ab)^2 - ab(c_+^2 + c_-^2) + (c_+c_-)^2$. The partial transposition operation in Eq. (3.9) on the two mode Gaussian state, transforms $\hat{\rho} \to \hat{\rho}^{T_1}$ ($\gamma \to \tilde{\gamma}_1$). This operation, given in Eq. (3.9), is equivalent to flipping the sign of c_+c_-, i.e

$$ \langle\hat{\chi}_1\hat{\chi}_2\rangle\langle\hat{\mathcal{P}}_1\hat{\mathcal{P}}_2\rangle \to -\langle\hat{\chi}_1\hat{\chi}_2\rangle\langle\hat{\mathcal{P}}_1\hat{\mathcal{P}}_2\rangle. \tag{3.20} $$

As a result $\mathbf{\Delta}$ is changed to $\tilde{\mathbf{\Delta}}$ where $\tilde{\mathbf{\Delta}} = a^2 + b^2 - 2c_+c_-$. Using Eq. (3.19) the symplectic eigenvalues of the partially transposed CM are given by $\tilde{\nu}_\pm$,

$$ \tilde{\nu}_\pm = \sqrt{\frac{\tilde{\mathbf{\Delta}} \pm \sqrt{\tilde{\mathbf{\Delta}}^2 - 4{\rm Det}(\gamma)}}{2}}. \tag{3.21} $$

The PPT criterion in a two mode Gaussian state is given by a lower bound on the smallest symplectic eigenvalue of the partially transposed state,

$$\tilde{\nu}_- \geq 1. \tag{3.22}$$

This inequality is equivalent to $c_+c_- \geq 0$ [134, 79, 132]. Hence for the type of states considered in our work,

$$\langle \hat{\chi}_1 \hat{\chi}_2 \rangle \langle \hat{\mathcal{P}}_1 \hat{\mathcal{P}}_2 \rangle \geq 0, \tag{3.23}$$

ensures a generic separable two mode state. Conversely $\langle \hat{\chi}_1 \hat{\chi}_2 \rangle \langle \hat{\mathcal{P}}_1 \hat{\mathcal{P}}_2 \rangle < 0$ is a necessary and sufficient condition for modes 1 and 2 to share entanglement in both pure and mixed states.

In Fig. 3.1, we show the porition of entangled two mode state, out of the set of valid two mode states, for fixed values of a and b. Using the parametrization, given in Ref. [136],

$$d_\pm = \frac{1}{\sqrt{2}}(c_+ \pm c_-), \quad d_\pm \in \{0, \sqrt{2ab}\}. \tag{3.24}$$

The condition for the symplectic invariants a, b, c_+, c_- to describe a physically valid CM is given by $\mathbf{\Delta} \leq 1 + \det(\gamma)$, following from Eq. (2.18), which is also identical to Eq. (2.32). The black lines in Fig. 3.1, show where this inequality is saturated. Likewise the dotted red lines in Fig. 3.1 show where $c_+c_- = 1$, equivalent to $\tilde{\mathbf{\Delta}} = 1 + \det(\gamma)$, further equivalent to $\tilde{\nu}_- = 1$. Hence the dotted red lines seperate entangled from separable states, with the entangled states making up the darker enclosed regions.

3.3.1.3 Two mode entanglement in a pure state

Pure states are symmetric with $a = b$ and $c_+ = -c_- = \sqrt{a^2 - 1}$ [134, 137]. For pure states Eq. (3.21) thus simplifies to

$$\tilde{\nu}_- = a - \sqrt{a^2 - 1} = \sqrt{\langle \hat{\chi}_1^2 \rangle \langle \hat{\mathcal{P}}_1^2 \rangle} - \sqrt{\langle \hat{\chi}_1^2 \rangle \langle \hat{\mathcal{P}}_1^2 \rangle - 1}, \tag{3.25}$$

where we have used the definition of a, given in Eq. (3.14), to write the smallest symplectic eigenvalue of the partially transposed two mode state in terms of the CM matrix elements. Given that $\tilde{\nu}_-^{-1} = \|\hat{\rho}^{T_i}\|_1$ [134], Eq. (3.7) is computable in a two mode pure state via the following expression,

$$\tau_G(1) = \tau_G(1:2) = \frac{1}{4}\left(\underbrace{\sqrt{\langle \hat{\chi}_1^2 \rangle \langle \hat{\mathcal{P}}_1^2 \rangle} + \sqrt{\langle \hat{\chi}_1^2 \rangle \langle \hat{\mathcal{P}}_1^2 \rangle - 1}}_{\tilde{\nu}_-^{-1} = \|\hat{\rho}^{T_1}\|_1} - 1 \right)^2. \tag{3.26}$$

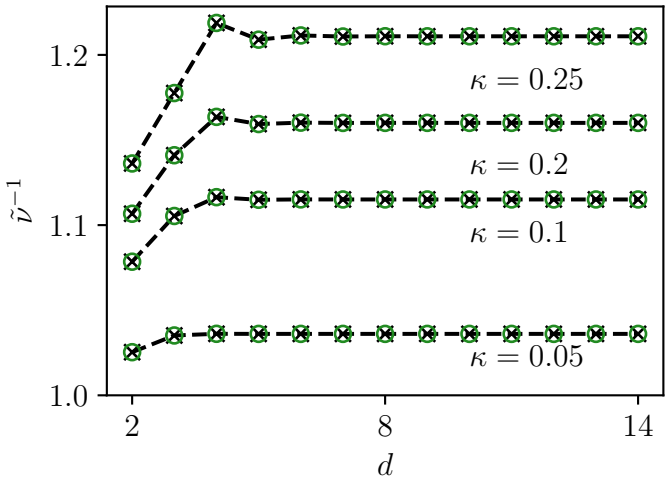

Figure 3.2: Green circles show $(\tilde{\nu}_-^{-1})_1 = \sqrt{\langle\hat{\chi}_1^2\rangle\langle\hat{\mathcal{P}}_1^2\rangle}+\sqrt{\langle\hat{\chi}_1^2\rangle\langle\hat{\mathcal{P}}_1^2\rangle - 1}$, while black crosses indicate $(\tilde{\nu}_-^{-1})_1 = \min(|\mathrm{eig}(\mathrm{i}\sigma\tilde{\gamma}_1)|)$, with $\tilde{\gamma}_1$ obtained from Eq. (3.9). Results are shown for a 1D chain of QHOs (see Eq. (3.30)) across different nearest-neighbor coupling values κ as a function of chain length. The mode label is omitted on the y-axis due to the symmetry of the chain.

3.3.2 Gaussian tangle in a multimode state

Having shown how the Gaussian tangle is computable for a two mode pure state, we use the 'modewise' decompostion to derive a formulae for Eq. (3.7), for the multipartite case.

Lemma. 1 .- Any d mode pure Gaussian state can be written as a tensor product of d two mode pure states, via local symplectic transformations, which preserve the bipartite entanglement information.

Proof .- See [138].

In the case of the bipartition between mode i and $d-1$ modes in a d mode system, the bipartite entanglement information is contained within a *single* two mode *pure* CM [138, 79, 63],

$$\gamma_i' = \begin{pmatrix} \sqrt{\langle\hat{\chi}_i^2\rangle\langle\hat{\mathcal{P}}_i^2\rangle} & 0 & \sqrt{\langle\hat{\chi}_i^2\rangle\langle\hat{\mathcal{P}}_i^2\rangle - 1} & 0 \\ 0 & \sqrt{\langle\hat{\chi}_i^2\rangle\langle\hat{\mathcal{P}}_i^2\rangle} & 0 & -\sqrt{\langle\hat{\chi}_i^2\rangle\langle\hat{\mathcal{P}}_i^2\rangle - 1} \\ \sqrt{\langle\hat{\chi}_i^2\rangle\langle\hat{\mathcal{P}}_i^2\rangle - 1} & 0 & \sqrt{\langle\hat{\chi}_i^2\rangle\langle\hat{\mathcal{P}}_i^2\rangle} & 0 \\ 0 & -\sqrt{\langle\hat{\chi}_i^2\rangle\langle\hat{\mathcal{P}}_i^2\rangle - 1} & 0 & \sqrt{\langle\hat{\chi}_i^2\rangle\langle\hat{\mathcal{P}}_i^2\rangle} \end{pmatrix}. \quad (3.27)$$

The modewise decomposition ensures that, for any bipartition between a single mode i and the remaining $d-1$ modes of a pure d-mode Gaussian state, the bipartite

entanglement is completely encoded in a *single* two-mode pure covariance matrix γ_i' given in Eq. (3.27). In other words, local symplectic operations disentangle all other modes, so that the correlations relevant for quantifying entanglement across the bipartition $(i|\text{rest})$ are captured by γ_i' alone.

Since γ_i' describes a *pure* two-mode Gaussian state, its entanglement can be evaluated using the procedure of Sec. 3.3.1. In particular, using the formulae given for the Gaussian tangle in a two mode pure state in Eq. (3.26) in sub-sec. 3.3.1.3, the tangle is computed from the trace norm of the partially transposed density operator, which for γ_i' is determined by its smallest symplectic eigenvalue under partial transposition, $(\tilde{\nu}_-)_i$. This yields

$$\|\hat{\rho}^{T_i}\|_1 = (\tilde{\nu}_-^{-1})_i = \sqrt{\langle\hat{\chi}_i^2\rangle\langle\hat{\mathcal{P}}_i^2\rangle} + \sqrt{\langle\hat{\chi}_i^2\rangle\langle\hat{\mathcal{P}}_i^2\rangle - 1}. \tag{3.28}$$

Thus, by inserting the expression for $\|\hat{\rho}^{T_i}\|_1$ into the formula for the Gaussian tangle in Eq. (3.7), we find that, by virtue of the modewise decomposition, the multipartite Gaussian tangle can be computed directly from the local variances/CM elements of mode i, in the same way as in the two-mode case, given in Eq. (3.26),

$$\tau_G(i) = \frac{1}{4}\left(\underbrace{\sqrt{\langle\hat{\chi}_i^2\rangle\langle\hat{\mathcal{P}}_i^2\rangle} + \sqrt{\langle\hat{\chi}_i^2\rangle\langle\hat{\mathcal{P}}_i^2\rangle - 1}}_{\tilde{\nu}_-^{-1} = \|\hat{\rho}^{T_1}\|_1} - 1\right)^2. \tag{3.29}$$

Example .- A well studied example of a quadratic bosonic Hamiltonian, is the discretization of the Klein-Gordon Hamiltonian in $1D$ [63, 139, 121, 140, 141] ,

$$\hat{H} = \frac{1}{2}\left(\sum_{i=1}^{d} \hat{\chi}_i^2 + \hat{\mathcal{P}}_i^2 + \kappa\hat{\chi}_i\hat{\chi}_{i+1}\right), \quad |\kappa| < 1, \tag{3.30}$$

where $\hat{\chi}_{d+1} = \hat{\chi}_1$. The resultant Hamiltonian describes a chain of QHOs with nearest neighbor couplings and periodic boundary conditions. Ref [141], looked at entanglement in the harmonic oscillator chain, between a single mode and the rest of the chain. The entanglement measure used was the von Neumann entropy, the formulae for which is given in appendix A.3. Here we will use the 1D QHO chain, to numerically show the validity of the formulae in Eq. (3.28).

The Hamiltonian matrix of the QHO chain is given by $T \oplus \mathbb{1}$, where T is a circulant matrix of the form,

$$T = \begin{pmatrix} 1 & \kappa & \cdots & 0 & \kappa \\ \kappa & 1 & \cdots & 0 & 0 \\ \vdots & \vdots & \ddots & \vdots & \vdots \\ 0 & 0 & \cdots & 1 & \kappa \\ \kappa & 0 & \cdots & \kappa & 1 \end{pmatrix}. \tag{3.31}$$

We use the formulae Eq. (2.34) to compute the groundstate CM, given that here $H^{\chi} = T$.

Fig. 3.2 shows the agreement between $\tilde{\nu}_{-}^{-1}$ computed from the minimum symplectic eigenvalue of the partially transposed CM, and from the CM matrix expression in the r.h.s of Eq. (3.29).

3.4 Gaussian Monogamy

3.4.1 Gaussian monogamy inequality

Having established how to compute the multimode tangle, we can now use this quantity to write a general monogamy inequality for the Gaussian tangle:

$$\tau_G(i) \geq \sum_{j=1}^{d} \tau_G(i:j), \forall j \neq i, \tag{3.32}$$

where $\tau_G(i:j)$ denotes the pairwise entanglement shared between modes i and j.

For mixed states, the pairwise tangle $\tau_G(i:j)$ is defined via the convex roof construction,

$$\tau_G(i:j) = \inf_{\{p_k, \hat{\rho}_k\}} \sum_k p_k \tau_G(k), \quad \text{where} \quad \tau_G(k) = \frac{1}{4}\left(\|\hat{\rho}_k^{T_1}\|_1 - 1\right)^2, \tag{3.33}$$

where the two mode Gaussian state $\hat{p}_{ij}$ has been written in terms of a *convex combination* of *pure* two mode states $\hat{p}_k$ i.e $\hat{p}_{ij} = \sum_k p_k \hat{p}_k$. Thus $\tau_G(k)$ denotes the tangle across the single bipartition in the two mode pure state $\hat{\rho}_k$. See Appendix A.1 for the full definition of $\tau_G(i:j)$, and Refs. [119, 142] for further details.

3.4.2 Proof of Gaussian monogamy inequality

Here we will here give a sketch of the proof of the monogamy inequality for distributed Gaussian entanglement from [79]. The proof relies on a tight upper bounds on the pairwise tangle, given in terms of the off-diagonal CM elements. These upper-limits on the pairwise tangle, given here as the system tangle $\tau_G^{\text{sys}}(i:j)$, are defined as

$$\tau_G^{\text{sys}}(i:j) = f(-\langle \hat{\chi}_i \hat{\chi}_j \rangle \langle \hat{\mathcal{P}}_i \hat{\mathcal{P}}_j \rangle) \geq \tau_G(i:j), \ \forall i \neq j, \tag{3.34}$$

where $f(x) = (\sqrt{x} + \sqrt{x+1} - 1)^2/4$ for $x > 0$ and $f(x) = 0$, given $x \leq 0$ [79]. This definition of $f(x)$ follows from the fact that for $i \neq j$, if $\langle \hat{\chi}_i \hat{\chi}_j \rangle \langle \hat{\mathcal{P}}_i \hat{\mathcal{P}}_j \rangle > 0$, according to Eq. (3.23), modes i and j cannot share any entanglement and therefore $\tau_G(i:j) = 0$.

Due to the uncertainty principle $\langle\hat{\chi}_i^2\rangle\langle\hat{P}_i^2\rangle \geq 1$ and hence the Gaussian tangle can always be written as $\tau_G(i) = f(\langle\hat{\chi}_i^2\rangle\langle\hat{P}_i^2\rangle - 1)$. As the CM is a pure state, Eq. (2.20) is equivalent to

$$\langle\hat{\chi}_i^2\rangle\langle\hat{P}_i^2\rangle - 1 = -\sum_{j=1}^{d}\langle\hat{\chi}_i\hat{\chi}_j\rangle\langle\hat{\mathcal{P}}_i\hat{\mathcal{P}}_j\rangle, \forall j \neq i. \tag{3.35}$$

Hence $\tau_G(i) = f(\langle\hat{\chi}_i^2\rangle\langle\hat{P}_i^2\rangle - 1) = f\left(-\sum_{\forall j\neq i}^{d}\langle\hat{\chi}_i\hat{\chi}_j\rangle\langle\hat{\mathcal{P}}_i\hat{\mathcal{P}}_j\rangle\right)$.

In appendix A.2, we include the proof that $f(x)$ is a super-additive function for inputs $x \geq 0$ [143], i.e $f(x+y) \geq f(x) + f(y)$. This directly leads to the monogamy inequality,

$$\tau_G(i) \geq \sum_{j=1}^{d}\tau_G^{\text{sys}}(i:j) = \sum_{j=1}^{d} f(-\langle\hat{\chi}_i\hat{\chi}_j\rangle\langle\hat{\mathcal{P}}_i\hat{\mathcal{P}}_j\rangle) \geq \sum_{j=1}^{d}\tau_G(i:j), \forall j \neq i. \tag{3.36}$$

3.5 Conclusion

In this chapter, we explored the monogamy property of quantum entanglement. We began by introducing the tangle, a monogamous measure of entanglement for qubit systems, and presented its corresponding monogamy inequality.

We then extended the concept of the tangle to CV Gaussian states, demonstrating how to compute it for a two-mode pure state. Leveraging the modewise decomposition, we showed how the formulae for the Gaussian tangle in a two-mode setting can be generalized to evaluate the tangle across a bipartition between a single mode and the rest of an arbitrary multimode system.

Having established a method to compute this monogamous Gaussian entanglement measure, we introduced its associated monogamy inequality. Finally, we outlined the proof of the monogamy of distributed Gaussian entanglement, showing how a simple function of the off-diagonal CM elements—defined here as the system tangle—imposes a strict bound on pairwise entanglement, thereby yielding the monogamy inequality.

Chapter 4

Promiscuity and Monogamy in Gaussian States

4.1 Introduction

A qubit can share at most one unit of entanglement with other qubits. Consequently, the monogamy property can lead to frustration effects in certain condensed matter systems, such as Heisenberg antiferromagnets. In contrast, in Gaussian state systems a mode can, in principle, share an unbounded amount of entanglement with other modes [62], owing to the infinite dimensionality of the local Hilbert space associated with each mode. This can lead to more freely shareable promiscuous entanglement patterns in Gaussian states, compared to qubit systems.

In Sec. 4.2, we first derive a simple formula for the tangle between two modes in a pure two-mode state, corresponding to a two-mode Hamiltonian with a given intermodal coupling strength. This formula provides a reference entanglement value for the two-mode subsystem, which will play a crucial role in our definition of promiscuous and monogamous entanglement-sharing behaviors in this and the following chapter. In Sec. 4.3 we proceed to investigate the distribution of entanglement in a three-mode state.

Although an exact description of the Gaussian ground state requires an infinite-dimensional Hilbert space, away from the critical point the effective state space becomes finite-dimensional. In Sec. 4.4 we contrast the entanglement behavior of the three-mode Gaussian ground state with that of a truncated Fock space approximation of the three mode Hamiltonian. Finally in Sec. 4.5 we study the thermodynamic limit of a Hamiltonian where identical intermodal couplings lead to a high degree of symmetry. Exploiting this symmetry, we derive and analyze compact expressions for the entanglement.

4.2 Two Mode State

A general two mode quadratic Hamiltonian, with inter-modal coupling only in position coordinates, is given by

$$\hat{H} = \frac{1}{2}\left(\hat{\chi}_1^2 + \hat{\chi}_2^2 + \hat{\mathcal{P}}_1^2 + \hat{\mathcal{P}}_2^2\right) + \kappa\hat{\chi}_1\hat{\chi}_2, \quad |\kappa| < 1. \tag{4.1}$$

In order for the positive definite constraint on the Hamiltonian matrix to be obeyed, $|\kappa| < 1$. The Hamiltonian matrix for the two mode state is given as

$$H = \underbrace{\begin{pmatrix} 1 & \kappa \\ \kappa & 1 \end{pmatrix}}_{H_\chi} \oplus \mathbb{1}_2. \tag{4.2}$$

The symplectic eigenvalues of H can be computed from As such the symplectic spectrum $\{\epsilon_+, \epsilon_-, \epsilon_+, \epsilon_-\}$ is given by,

$$\epsilon_\pm = \sqrt{1 \pm \kappa}. \tag{4.3}$$

Using Eq. (5.10), the two mode groundstate correlation matrix is given by

$$\gamma_0 = \frac{1}{2}\begin{pmatrix} \epsilon_+^{-1} + \epsilon_-^{-1} & \epsilon_+^{-1} - \epsilon_-^{-1} \\ \epsilon_+^{-1} - \epsilon_-^{-1} & \epsilon_+^{-1} + \epsilon_-^{-1} \end{pmatrix} \oplus \begin{pmatrix} \epsilon_+ + \epsilon_- & \epsilon_+ - \epsilon_- \\ \epsilon_+ - \epsilon_- & \epsilon_+ + \epsilon_- \end{pmatrix}, \tag{4.4}$$

where $2\langle\hat{\chi}_1^2\rangle = 2\langle\hat{\chi}_2^2\rangle = \epsilon_+^{-1} + \epsilon_-^{-1}$, $2\langle\hat{\chi}_1\hat{\chi}_2\rangle = \epsilon_+^{-1} - \epsilon_-^{-1}$, $2\langle\hat{\mathcal{P}}_1^2\rangle = 2\langle\hat{\mathcal{P}}_2^2\rangle = \epsilon_+ + \epsilon_-$ and $2\langle\hat{\mathcal{P}}_1\hat{\mathcal{P}}_2\rangle = \epsilon_+ - \epsilon_-$. Using the formulae for the inverse of smallest symplectic eigenvalue of the partially transposed CM in Eq. (3.26),

$$\tilde{\nu}_-^{-1} = \sqrt{\frac{1}{4}(\epsilon_+^{-1} + \epsilon_-^{-1})(\epsilon_+ + \epsilon_-)} + \sqrt{\frac{1}{4}(\epsilon_+^{-1} + \epsilon_-^{-1})(\epsilon_+ + \epsilon_-) - 1}, \tag{4.5}$$

which simplifies to,

$$\tilde{\nu}_-^{-1} = \max\left(\sqrt{\epsilon_+^{-1}\epsilon_-}, \sqrt{\epsilon_+\epsilon_-^{-1}}\right) = \sqrt{\frac{\epsilon_+}{\epsilon_-}}. \tag{4.6}$$

From the definition of the Gaussian tangle in Eq. (3.26),

$$\tau_G(1) = \tau_G(2) = \tau_G(1:2) = \frac{1}{4}\left(\underbrace{\sqrt{\frac{\epsilon_+}{\epsilon_-}}}_{\tilde{\nu}_-^{-1}} - 1\right)^2. \tag{4.7}$$

This entanglement value, as computed by the tangle between modes 1 and 2 in the two-mode Hamiltonian of Eq. (4.1), will serve as a *reference* entanglement value as we proceed to consider multipartite systems.

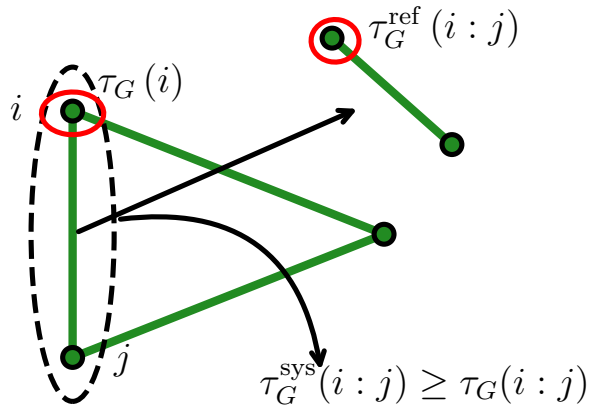

Figure 4.1: Coupling graph of a three mode Hamiltonian in Eq. (4.8), illustrated for $\beta = 1$. The red circle illustrates the bipartition between mode i and the other two modes, where $\tau_G(i)$ measures the entanglement across this bipartition and limits the strength of the pairwise tangle between modes i and j, to be no greater then $\tau_G^{\text{sys}}(i:j)$. The reference tangle, given by $\tau_G^{\text{ref}}(i:j)$, is the Gaussian tangle between i and j in the groundstate of the two mode Hamiltonian, $\hat{H}_{ij}$.

4.3 Three Mode State

Here we will extend the Hamiltonian looked at in Eq. (4.1). The three mode Hamiltonian we will consider here is

$$\hat{H} = \frac{1}{2}\left(\hat{\chi}_1^2 + \hat{\chi}_2^2 + \hat{\chi}_3^2 + \hat{\mathcal{P}}_1^2 + \hat{\mathcal{P}}_2^2 + \hat{\mathcal{P}}_3^2\right) + \kappa\hat{\chi}_1\hat{\chi}_2 + \kappa\beta\hat{\chi}_1\hat{\chi}_3 + \kappa\hat{\chi}_2\hat{\chi}_3, \quad |\kappa|, \beta \in [0,1]. \tag{4.8}$$

We investigate how the interaction with the third mode modifies the shareability of the entanglement between modes 1 and 2. In the tripartite Hamiltonian, modes 1 and 2 are coupled with strength κ. Modes 2 and 3 are coupled with the same strength, while the coupling between modes 1 and 3 varies with the parameter β. When $\beta = 0$, modes 1 and 3 are uncoupled, while $\beta = 1$ corresponds to the case where each mode interacts identically with the other two.

In the ground state of the tripartite Hamiltonian, the maximal pairwise tangle between modes 1 and 2 is given by $\tau_G^{\text{sys}}(1:2)$, which accounts for the correlations present in the full system ground state. In contrast, the pairwise tangle between modes 1 and 2 in isolation from the third mode is given by $\tau_G^{\text{ref}}(1:2)$, computed using the formulae of Eq. (4.7). Figure 4.1 illustrates the definitions of $\tau_G^{\text{ref}}(1:2)$ and $\tau_G^{\text{sys}}(1:2)$ in the three-mode system.

The ratio $\tau_G^{\text{sys}}(1:2)/\tau_G^{\text{ref}}(1:2)$ determines whether there exists a trade-off between the maximal tangle shared by modes 1 and 2 for a given coupling strength and the

residual entanglement these modes share with the rest of the system, i.e., mode 3. We refer to these two regimes as monogamous and promiscuous behavior, respectively. Note that due to the symmetry of the tripartite system, the entanglement between modes 1 and 2 must be identical to that shared between modes 2 and 3.

Figure 4.2 shows a heatmap of $\tau_G^{\text{sys}}(1:2)/\tau_G^{\text{ref}}(1:2) - 1$ as a function of positive κ and β. The plot is obtained for 2000 values of β with $\beta \in [0, 0.7]$, and 2000 values of κ with $\kappa \in [0.001, 0.7]$. In the limit $\kappa \to 0$, the ratio $\tau_G^{\text{sys}}(1:2)/\tau_G^{\text{ref}}(1:2) \to 1$. In Appendix A.4, we further analyze the behavior of $\tau_G^{\text{sys}}(1:3)$, showing the region of parameter space where modes 1 and 3 become unentangled.

At $\beta = 0$, we find $\tau_G^{\text{sys}}(1:2) > \tau_G^{\text{ref}}(1:2)$, indicating that the three-mode system allows for an enhancement of the pairwise tangle between nearest-neighbor modes, i.e., promiscuous behavior. By contrast, for large β—when the coupling strength between modes 1 and 3 becomes comparable to that between modes 1 and 2 (and modes 2 and 3)—the pairwise tangle is suppressed relative to its isolated reference value, corresponding to monogamous behavior.

For $\beta > 0$ and weak couplings, the pairwise entanglement is restricted. As κ increases, the behavior shifts to promiscuous. The solid black line in Fig. 4.2 indicates the boundary where $\tau_G^{\text{sys}}(1:2) = \tau_G^{\text{ref}}(1:2)$, dividing the parameter space into monogamous and promiscuous regions. For strong couplings (large κ), and for most of the β values considered, the pairwise entanglement behaves promiscuously. To better understand the transition from monogamous to promiscuous behavior as a function of coupling strength, we next examine a reduced Hilbert space description of the three-mode Hamiltonian.

4.4 Low Dimensional Approximation

4.4.1 Multipartite state

Ref. [110] investigated the approximation error in the correlation energy for the two mode Hamiltonian in Eq. (4.1), arising from a finite truncation of the Hilbert space, and found it to be negligible away from the critical point.

Using the truncated Fock state approach (see [110]), a quadratic d mode Hamiltonian with coupling only between position coordinates — using only the first two Fock states i.e $|0\rangle$ and $|1\rangle$ — leads to the following d *qubit* Hamiltonian,

$$\hat{H}^d_{\text{qubit}} = \frac{1}{2}\sum_{i=1}^{d}\left(2\mathbb{1}_2^i - \sigma_z^i\right) + \sum_{j>i}^{d} w_{ij}\sigma_x^i \otimes \sigma_x^j. \tag{4.9}$$

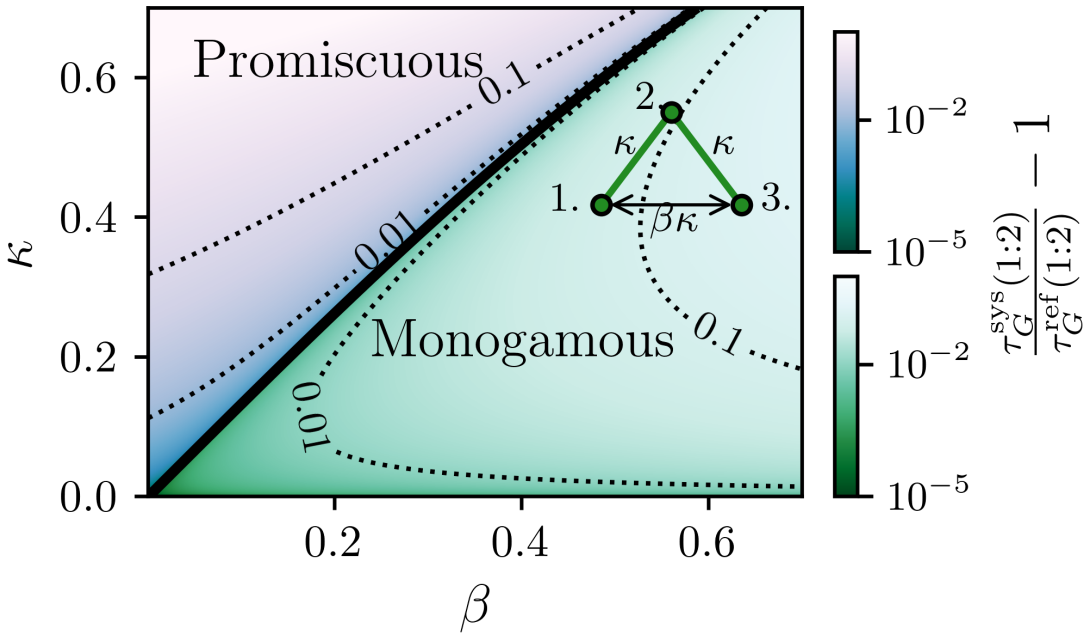

Figure 4.2: The monogamy/promiscuity boundary is shown by the solid black line, below which the entanglement behaves monogamously and above which, promiscuously. Both regions are shown as heat-maps, plotted on a log-scale. This is shown for different values of κ and β, see Eq. (4.8) for definitions of these parameters. The dotted lines show the contours of $\tau_G^{\mathrm{sys}}(1:2)/\tau_G^{\mathrm{ref}}(1:2) - 1$.

Here σ_z^i (σ_x^i) is the z (x) Pauli matrix, acting on the ith qubit, w_{ij} is determined by the coupling strength between modes and $\otimes$ denotes the tensor product. By introducing the qubit Hamiltonian in Eq. (4.9), we will be able to contrast the monogamy/promiscuity behavior in the infinite dimensional CV Gaussian, with the monogamy/promiscuity behavior in a two state approximation of the infinite Hilbert space.

4.4.1.1 Three mode state

Here we solve for the qubit approximation of Eq. (4.8), $\hat{H}^{d=3}_{\rm qubit}$, given in Eq. (4.9). When $d = 2$, Eq. (4.9) is a two qubit Hamiltonian, with $w_{12} = \kappa$. The general ground-state density matrix is a $2^d \times 2^d$ matrix, denoted by $\hat{\rho}^d$. The 4×4 ground state density matrix of $\hat{H}^{d=2}_{\rm qubit}$ is written as $\hat{\rho}^2$. The tangle between qubits 1 and 2, can be straightforwardly computed from the reduced density matrix, tracing out qubit 2, giving the 2×2 reduced density matrix $\hat{\rho}_2^2$. From Eq. (3.1) the tangle between qubits 1 and 2 is given by,

$$\tau^{\rm ref}(1:2) = 4{\rm Det}(\hat{\rho}_1^2) = 4{\rm Det}(\hat{\rho}_2^2) \tag{4.10}$$

This is analogously labeled to the Gaussian tangle in the two mode pure state, denoted here as $\tau_G^{\rm ref}(1:2)$. Given $d = 3$, $\hat{H}^3_{\rm qubit}$ is a three qubit Hamiltonian, where $w_{12} = w_{23} = \kappa$ and $w_{13} = \beta\kappa$. The ground state density matrix is given by $\hat{\rho}^3$. The monogamy inequality for distributed qubit entanglement, is given in terms of the tangle as $\tau(1) \geq \tau(1:2) + \tau(1:3)$, where $\tau(1) = 4{\rm Det}(\hat{\rho}_1^3)$ and $\hat{\rho}_1^3$ is a 2×2 matrix, found by tracing out qubits 2 and 3. The pairwise tangle $\tau(1:2)$ and $\tau(1:3)$ in the three qubit state is computed from Eq. (3.4).

In Fig. 4.3, we show how $\tau_G^{\rm ref}(1:2)$ and $\tau^{\rm ref}(1:2)$ are modified, due to the tripartite interaction, setting $\beta = 1/4$, and for negative and positive coupling κ, i.e a) and b). Note that the $x-$axis in Fig. 4.3 is written in terms of $|\kappa|^{-1/3}$, which is done in order for a convenient comparison with later chapters. From Fig. 4.3 a), both $\tau_G^{\rm sys}(1:2) > \tau_G^{\rm ref}(1:2)$ and $\tau(1:2) > \tau^{\rm ref}(1:2)$, for $|\kappa|^{-1/3} \leq 2$. In comparison for $0 \leq \kappa^{-1/3} \leq 2$, shown in b), both $\tau_G^{\rm sys}(1:2) < \tau_G^{\rm ref}(1:2)$ and $\tau(1:2) < \tau^{\rm ref}(1:2)$. Thus for a three mode (qubit) state, with positive inter-modal couplings, mode (qubit) 3 restricts the shared tangle between modes (qubits) 1 and 2. In b), for increased coupling strength, a sign change occurs in $\tau_G^{\rm sys}(1:2) - \tau_G^{\rm ref}(1:2)$ but not in $\tau(1:2) - \tau^{\rm ref}(1:2)$. The pairwise tangle between qubits becomes increasing restricted as a function of coupling strength.

In the limit of $\kappa \to 0$ for negative inter-modal (inter-qubit) coupling, the pairwise entanglement behaves promiscuously. Conversely in the of $\kappa \to 0$ for positive

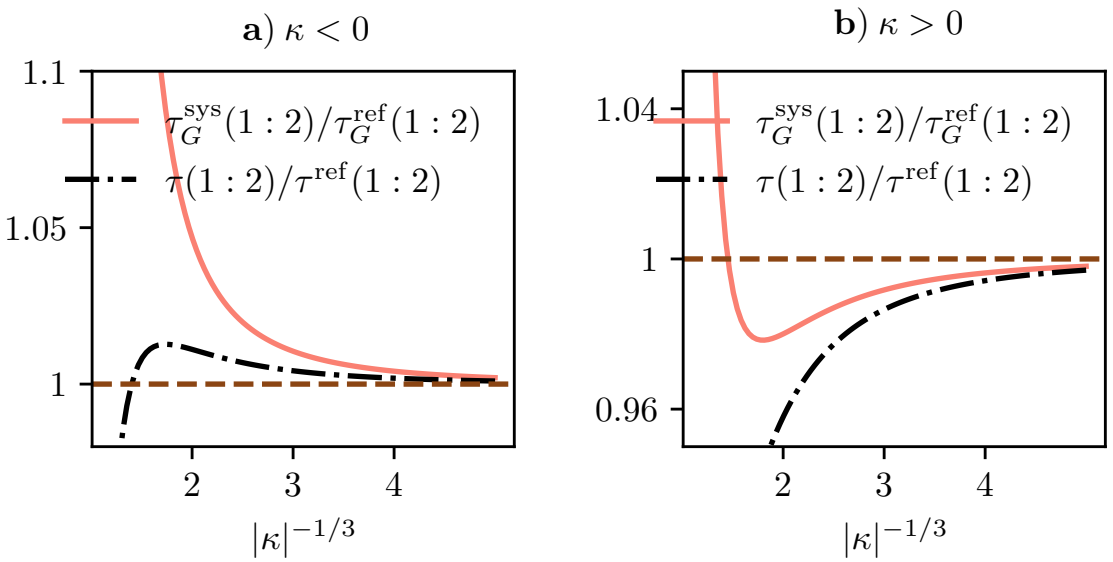

Figure 4.3: The solid orange curve is the tangle computed from solving Eq. (4.8) exactly. The dashed dotted black line, follows from the truncated Fock state approximation, with Hamiltonian given in Eq. (4.9) and $d = 3$. Below the horizontal dashed line shows where the pairwise entanglement between 1 and 2 behaves monogamously whereas above shows the promiscuous behavior.

inter-modal (inter-qubit) coupling, the pairwise entanglement behaves monogamously, where here the pairwise tangle in both the multi-qubit and multimode groundstate is suppressed. We thus find that in the non-interacting limit, truncating the bosonic Hilbert space to a two-level system, captures the asymptotic monogamy/promiscuity entanglement behavior. In comparison, for strong couplings, for both the positive and negative coupling, we observe promiscuous behavior, not captured by the two-level approximation.

4.5 Mean-Field Cluster

Having looked at a system of a small number of modes, we will now look at a toy model example where the number of modes grows toward infinity. This is possible to handle analytically for certain highly connected systems. Here we will look at the so called mean field cluster, which describes an all to all coupled Hamiltonian where every mode is equally coupled to every other mode. Such a state will have complete permutation symmetry, allowing for simplified expressions for quantities of interest. The d mode mean field cluster Hamiltonian is

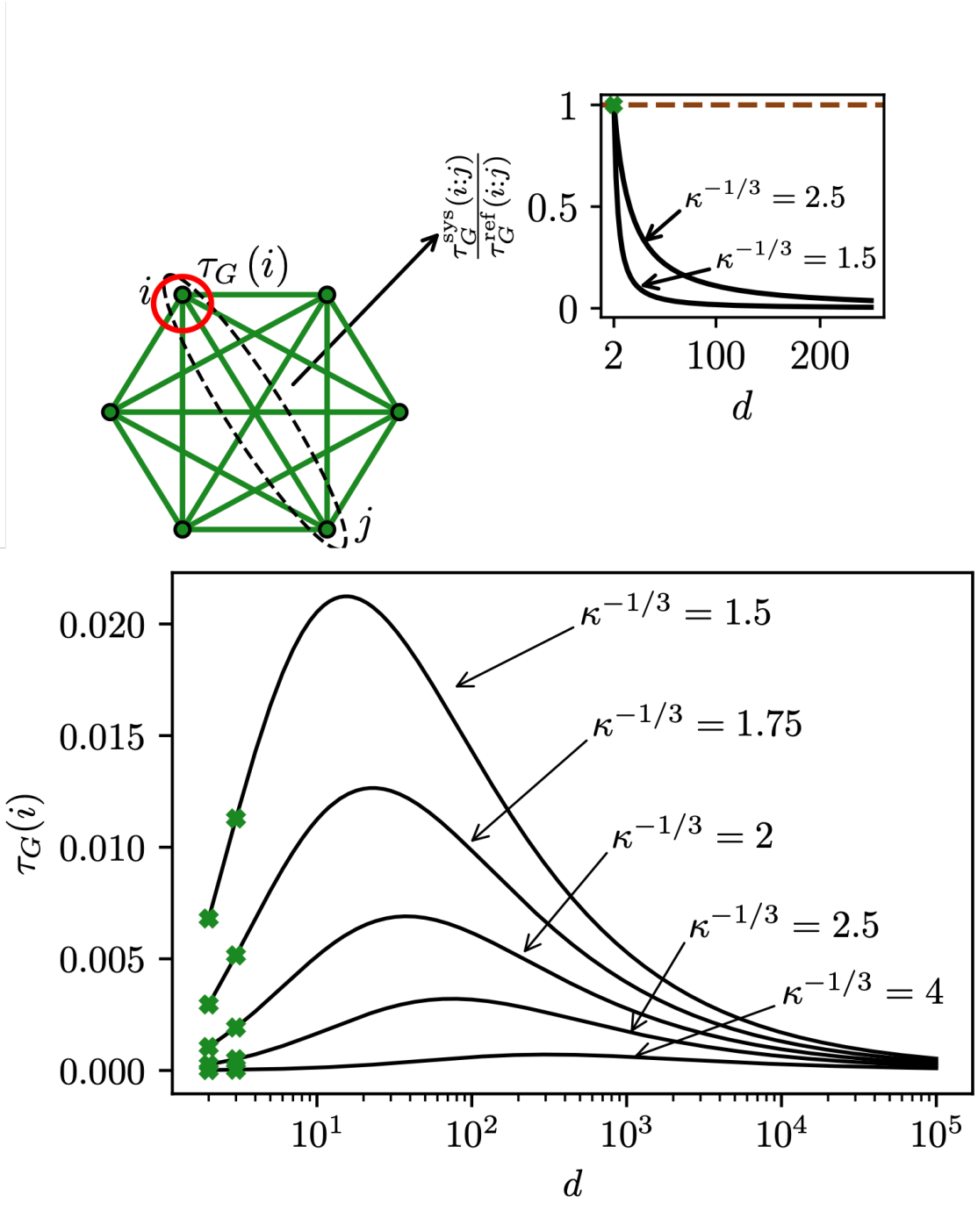

Figure 4.4: (Top) Monogamous behavior of the entanglement distribution in the mean field cluster. The decay of $\tau_G^{\mathrm{sys}}(i:j)/\tau_G^{\mathrm{ref}}(i:j)$ as a function of d is shown for two different coupling strength values. (Bottom) Decay of the tangle as a function of number of modes, plotted for a range of different coupling strength values. In the limit $d \to \infty$ each mode shares no entanglement with the rest of the cluster.

$$\hat{H} = \sum_{i=1}^{d} \frac{\hat{\chi}_i^2}{2} + \frac{\hat{\mathcal{P}}_i^{\,2}}{2} + \kappa \sum_{i>j}^{d} \hat{\chi}_i \hat{\chi}_j, \quad \text{with} \quad |\kappa| < 1. \tag{4.11}$$

Here each oscillator is equally coupled to every other oscillator, with coupling constant κ. The coupling matrix $H = H_\chi \otimes \mathbb{1}_d = C \oplus \mathbb{1}_d$, where C is a circulant matrix $C = \text{circ}(\underbrace{1, \kappa, ..., \kappa}_{d})$, and thus has a analytically soluble [144] eigenspectrum. When $\kappa > 0$, the symplectic spectrum (recall the symplectic eigenvalues are each repeated once in the spectrum) is given by

$$\{\underbrace{\sqrt{1+(d-1)\kappa}}_{\epsilon_+}, \underbrace{\underbrace{\sqrt{1-k}}_{\epsilon_-}, ..., \underbrace{\sqrt{1-k}}_{\epsilon_-}}_{d-1}, \underbrace{\sqrt{1+(d-1)\kappa}}_{\epsilon_+}, \underbrace{\underbrace{\sqrt{1-k}}_{\epsilon_-}, ..., \underbrace{\sqrt{1-k}}_{\epsilon_-}}_{d-1}\}. \tag{4.12}$$

Thus the unique symplectic eigenvalues are given by $\epsilon_+ = \sqrt{1+(d-1)\kappa}$ and $\epsilon_- = \sqrt{1-k}$, where $\epsilon_+ \geq \epsilon_-$, $\epsilon_+ \propto \sqrt{d}$ and ϵ_- is independent of d, occurring $2(d-1)$ times in the mean field cluster's symplectic spectrum. Conversely if $k < 0$, $\epsilon_\pm$ switch expressions i.e $\epsilon_+ = \sqrt{1-\kappa}$, $\epsilon_- = \sqrt{1+(d-1)\kappa}$. Hence in the negatively coupled cluster, in the limit where $d \to \infty$, $\epsilon_- \to 0$, scaling as $\sqrt{d}$. Thus in the infinite limit the positive definite constraint on the Hamiltonian matrix in Eq. (2.11) will not hold and the entanglement diverges. This is in comparison to the positive coupling regime, where for $|\kappa| < 1$, the lowest eigenvalue of C remains greater then zero for $d \to \infty$. We will thus focus here on the positive coupling regime.

The ground state CM is given by $\gamma_0 = C^{-1/2} \oplus C^{1/2}$ as per Eq. (5.10), where $C^{1/2} = O_c \text{diag}(\sqrt{\lambda_+^C}, \sqrt{\lambda_-^C}, .., \sqrt{\lambda_-^C}) O_c^T$ and $C^{-1/2} = O_c \text{diag}(\sqrt{1/\lambda_+^C}, \sqrt{1/\lambda_-^C}, .., 1/\sqrt{\lambda_-^C}) O_c^T$, with O_c the orthogonal matrix which diagonalizes C and $\lambda_\pm^C$ are the normal eigenvalues of C. Recall the relationship between the normal and symplectic eigenvalues are given as $\epsilon_\pm = \sqrt{\lambda_\pm^C}$. As the eigenvectors of a circulant matrix are the Fourier modes, we derive the following expression for the matrix elements of the ground state CM in terms of $\epsilon_\pm$,

$$(C)^{1/2} = \frac{1}{d} \begin{pmatrix} (d-1)(\epsilon_+ + \epsilon_-) & \epsilon_+ - \epsilon_- & \cdots \\ \epsilon_+ - \epsilon_- & (d-1)(\epsilon_+ + \epsilon_-) & \cdots \\ \vdots & \vdots & \ddots \end{pmatrix}, \tag{4.13}$$

$$(C)^{-1/2} = \frac{1}{d} \begin{pmatrix} (d-1)(\frac{1}{\epsilon_+} + \frac{1}{\epsilon_-}) & \frac{1}{\epsilon_+} - \frac{1}{\epsilon_-} & \cdots \\ \frac{1}{\epsilon_+} - \frac{1}{\epsilon_-} & (d-1)(\frac{1}{\epsilon_+} + \frac{1}{\epsilon_-}) & \cdots \\ \vdots & \vdots & \ddots \end{pmatrix}. \tag{4.14}$$

These matrix elements can further be written explicitly in terms of κ and d, using the definitions for $\epsilon_\pm$,

$$(C^{-1/2})_{ii} = \langle \hat{\chi}_i^2 \rangle = \frac{1}{d} \left(\frac{(d-1)}{\sqrt{1-\kappa}} + \frac{1}{\sqrt{\kappa(d-1)+1}} \right), \tag{4.15}$$

$$(C^{-1/2})_{ij} = \langle \hat{\chi}_i \hat{\chi}_j \rangle = \frac{1}{d}\left(-\frac{1}{\sqrt{1-\kappa}} + \frac{1}{\sqrt{\kappa(d-1)+1}} \right), \ \forall i \neq j. \tag{4.16}$$

and

$$(C^{-1/2})_{ii} = \langle \hat{\mathcal{P}}_i^2 \rangle = \frac{1}{d}\left((d-1)\sqrt{1-\kappa} + \sqrt{\kappa(d-1)+1} \right), \tag{4.17}$$

$$(C^{-1/2})_{ij} = \langle \hat{\mathcal{P}}_i \hat{\mathcal{P}}_j \rangle = \frac{1}{d}\left(-\sqrt{1-\kappa} + \sqrt{\kappa(d-1)+1} \right), \ \forall i \neq j. \tag{4.18}$$

From the expression in Eq. (4.17) and Eq. (4.15), we can see that in the limit $d \to \infty$, $\langle \hat{\mathcal{P}}_i^2 \rangle \langle \hat{\chi}_i^2 \rangle \to 1$, $\forall i \in \{1, .., d\}$. Hence from the expression for the Gaussian tangle in Eq. (3.7) and Eq. (3.28), $\tau_G(i) \to 0$, $\forall i \in \{1, .., d\}$. This is shown in Fig. 4.4, for different κ values. Interestingly, Fig. 4.4, shows that at small d, there is an initial increase in the tangle as a function of connected modes.

Due to the monogamy inequality, the decay of the d mode tangle necessitates that the pairwise tangle decays to zero in the limit $d \to \infty$. The decay of the pairwise tangle is evident from Eq. (4.18)-Eq. (4.16). In the limit $d \to \infty$, the off-diagonal elements of the CM vanish. In the limit $d \to \infty$, $\langle \hat{\mathcal{P}}_i \hat{\mathcal{P}}_j \rangle \to 0$ scaling as $\mathcal{O}(d^{-1/2})$ and $\langle \hat{\chi}_i \hat{\chi}_j \rangle \to 0$, scaling as $\mathcal{O}(d^{-1})$. Due to the decay of the inter-modal correlation elements, the maximal pairwise tangle between any two modes in the cluster $\tau_G^{\text{sys}}(i:j)$, decays to zero in the limit $d \to \infty$, following from the expression for $\tau_G^{\text{sys}}(i:j)$, given in terms of the off-diagonal CM matrix elements in Eq. (3.34).

In Fig. 4.4, the inset shows the monogamous behavior of the cluster entanglement distribution for two different κ values. A stronger coupling strength, results in a more rapid decay of $\tau_G^{\text{sys}}(i:j)/\tau_G^{\text{ref}}(i:j)$. Note that $\tau_G^{\text{ref}}(i:j)$, computed via Eq. (4.7), is simply the bipartite tangle for $d = 2$ in the mean-field cluster Hamiltonian in Eq. (4.11).

Fig. 4.5 shows the numerical scaling of the decay of the tangle. In a) we observe the $\mathcal{O}(d^{-1/2})$ decay of $\tau_G(i)$, and in b) the $\mathcal{O}(d^{-3/2})$ decay of the pairwise tangle upper bound. Whilst Fig. 4.5 b) concerns $\tau_G^{\text{sys}}(i:j)$, showing the monogamous behavior in the cluster, the associated monogamous behavior in the thermodynamic limit follows directly from the monogamy inequality together with the fact that $\tau_G(i)$ remains finite as $d \to \infty$ for $\kappa > 0$, where in this limit it is also found to vanish.

4.6 Conclusion

We investigated the entanglement properties of a three mode state. We showed that increasing the connectivity of the three-mode system, limited (monogamy) or enhanced (promiscuity) the allowed amount of entanglement the two mode reduced

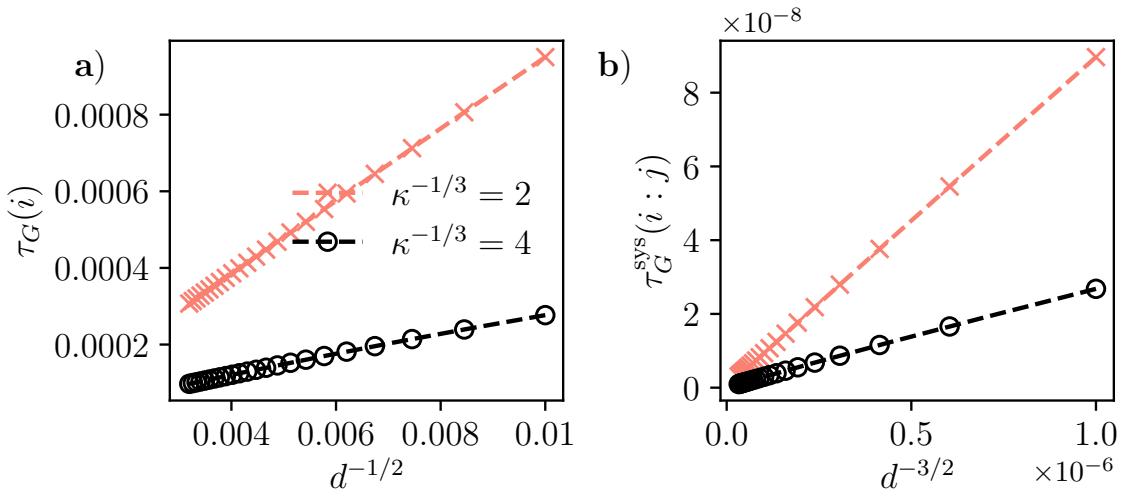

Figure 4.5: **a)** shows that the tangle decays with $\mathcal{O}(d^{-1/2})$ in the limit $d \to \infty$. **b)** shows the decay of the pairwise tangle, where $\tau_G^{\mathrm{sys}}(i:j)$ decays to zero as $\mathcal{O}(d^{-3/2})$.

state was able to share, depending on the magnitude and sign of the coupling constants.

We further looked at an all-to-all connected system, i.e the mean field cluster and showed the decay of the entanglement in the cluster and resultant monogamous behavior, as a function of increasing connectivity. This limiting case illustrates how the monogamy of entanglement causes a highly connected system to share less entanglement, compared to a less connected one. This is in accord with results looking at high connectivity in both Gaussian states [86] and quantum many-body systems more generally [145]. Our results extend the findings in Ref. [86], to show that not only can increasing the connectivity of a harmonic system reduce entanglement, but in the limit of certain infinitely connected harmonic networks, all forms of entanglement vanish completely.

In the next chapter, we use the monogamy/promiscuity framework developed here, to characterize the behavior of the many-body contributions to the dispersive interaction energy.

Chapter 5

A Quantum Information Perspective on Many-Body Dispersive Forces

5.1 Introduction

Here we apply the theory of Gaussian entanglement to understand the properties of the many-body effects in dispersive bonding. In Sec. 5.2 we introduce the QDO model, central to the work in this thesis and show how it is used to compute pairwise and many-body dispersive interaction energies.

We show how the expression for the dispersive bond energy is consistent with the symplectic eigenvalue expression introduced in Chapter 2. We show how the Gaussian state framework provides access to the quantum correlations in the QDO groundstate and thus how to efficiently apply the Gaussian tangle from Chapter 3.

Using the definition of the Gaussian tangle, we define an entanglement monotone, we call the reduced tangle. In Sec. 5.3, we derive an inequality that captures the relation and dependence of pairwise and many-body contributions to the binding energy and the distribution of the reduced tangle. Then in Sec. 5.4 we numerically show the relationship between many-body effects and the entanglement distribution, using examples of a trimer, a chain, 2D and 3D lattices.

5.2 QDO Model

In the QDO model a particle, molecule or molecular fragment is treated as a three dimensional quantum harmonic oscillator (given by three quantum harmonic oscillators or modes per QDO), with mass m_μ, frequency ω_μ, nuclear charge $+q_\mu$ and Drude

quasi-particle of charge $-q_\mu$. The instantaneous dipole moment $q_\mu \hat{\boldsymbol{r}}_\mu$ is proportional to the displacement, $\hat{\boldsymbol{r}}_{\boldsymbol{\mu}} = (\hat{r}^x_\mu, \hat{r}^y_\mu, \hat{r}^z_\mu)$ of the QDO from its equilibrium, determined by the center position of the particle. The corresponding momentum vector is given by $\hat{\boldsymbol{p}}_\mu = (\hat{p}^x_\mu, \hat{p}^y_\mu, \hat{p}^z_\mu)$.

Dipolar interactions between the QDOs arise from the Coulomb potential and are described by a $3N \times 3N$ coupling matrix $\mathcal{T}$. Individual 3×3 blocks of $\mathcal{T}$ describe the interaction between QDO μ and ξ, given by

$$e^T_\mu \mathcal{T} e_\xi = \frac{1}{R^3_{\mu\xi}} \left(\mathbb{1}_3 - \frac{3\boldsymbol{R}_{\mu\xi} \otimes \boldsymbol{R}_{\mu\xi}}{R^2_{\mu\xi}} \right) \quad \text{for} \quad \mu \neq \xi, \tag{5.1}$$

and $e^T_\mu \mathcal{T} e_\mu = 0_3$, where 0_3 is the 3×3 zero matrix. Here $\otimes$ denotes the outer product, e^T_μ is a $3 \times 3N$ matrix, e.g $e^T_1 = [\mathbb{1}_3, 0_3, ..0_3], e^T_2 = [0_3, \mathbb{1}_3, ..0_3]$ etc and $\boldsymbol{R}_{\mu\xi} = (x_\mu - x_\xi, y_\mu - y_\xi, z_\mu - z_\xi)$, where (x_μ, y_μ, z_μ) is the position of the QDO in Cartesian space.

For simplicity, we consider here the case where all QDO parameters are identical, given by (q, m, ω). For the general case, as well as a more detailed discussion of the applicability of the dipole QDO model to amending many-body dispersive corrections into density functionals via the so-called MBD method, see Appendix B.1.

We define operators $\hat{\boldsymbol{\chi}}_\mu = \hat{\boldsymbol{r}}_\mu \sqrt{\omega m/\hbar}$, $\hat{\boldsymbol{\mathcal{P}}}_\mu = \hat{\boldsymbol{p}}_\mu / \sqrt{\hbar m \omega}$. Then by introducing the polarizability $\alpha = q^2/(m\omega^2 4\pi\epsilon_0)$, the QDO Hamiltonian, (also called the coupled fluctuating dipole model) units of $\hbar\omega$ is

$$\hat{H} = \frac{1}{2} \left(\sum_{i=1}^{3N} \hat{\mathcal{P}}^2_i + \sum_{i=1}^{3N} \hat{\chi}^2_i \right) + \alpha \sum_{i>j}^{3N} \hat{\chi}_i \mathcal{T}_{ij} \hat{\chi}_j. \tag{5.2}$$

We use the indices i, j to label the individual harmonic oscillators or modes.

5.2.1 Many-Body effects

The dispersive binding energy is the difference between the ground state energy of the non-interacting and interacting QDOs. The dispersive binding energy, inclusive of the many-body contributions is written as

$$E = \frac{3N}{2} - \frac{1}{2} \sum_{i=1}^{3N} \sqrt{\lambda_i}, \tag{5.3}$$

where λ_i are the normal eigenvalues of the $3N \times 3N$ potential matrix V, with $V_{ii} = 1$ and $V_{ij} = \alpha \mathcal{T}_{ij}$, $\forall i \neq j$. The expression for the dispersive binding energy E follows from the adiabatic connection fluctuation dissipation theorem and can be found in [146, 147]. The binding energy E is always positive, which we prove in sub-sec. 5.2.2. In order for the energy to be real, the matrix V must be positive definite. This

enforces the constraint $\alpha t_i > -1 \ \forall i$, where t_i are the eigenvalues of the real symmetric matrix dipole coupling $\mathcal{T}$.

The dispersive binding energy is often treated as a perturbative correction to the non-interacting groundstate [3, 148, 149, 150], leading to the familiar pair-potential. This is derived by a second order Taylor expansion of $\sqrt{\lambda_i}$ in small parameters αt_i. This is possible when $\alpha\|\mathcal{T}\|_2 < 1$, equivalent to $\max(\alpha|t_1|, .., \alpha|t_{3N}|) < 1$. We will assume $\alpha\|\mathcal{T}\|_2 < 1$ holds throughout, explicitly stating instances when this is not the case. As $\sum_{i=1}^{3N} t_i^k = \mathrm{tr}(\mathcal{T}^k)$ and $\mathcal{T}$ is traceless, the full power series expansion of E in terms of αt_i can be written as follows,

$$E = \sum_{k=2}^{\infty} \delta_k, \quad \delta_k = \frac{(-1)^k(2k-3)!!}{2^{k+1}k!}\alpha^k \mathrm{tr}(\mathcal{T}^k). \tag{5.4}$$

This expression for the dispersive correlation energy can be derived from the total electronic correlation energy, via the adiabatic connection fluctuation dissipation theorem [146, 147], using the random phase approximation [151, 152, 153, 154]. See Ref [149], for the rate of convergence of the power series expansion of the dispersive interaction energy, for variously arranged nano-clusters.

The pairwise potential, aptly named as it can be written additively over all pairs in the system, gives the leading order correction to the non-interacting energy [155, 49],

$$\delta_2 = \frac{\alpha^2}{16}\mathrm{tr}(\mathcal{T}^2) = \frac{3\alpha^2}{4}\sum_{\mu>\xi}^{N} R_{\mu\xi}^{-6} > 0. \tag{5.5}$$

The many-body (MB) correction to the binding energy is thus given by

$$\delta_{\mathrm{MB}} = E - \delta_2 \tag{5.6}$$

and can be repulsive or attractive. The so called Axilrod-Teller (AT) triple dipole approximation is given by δ_3 [156, 54]. The MB effect can thus be written in terms of the higher order corrections to the pairwise potential,

$$\delta_{\mathrm{MB}} = \sum_{k=3}^{\infty} \delta_k. \tag{5.7}$$

5.2.1.1 Axilrod-Teller potential

The AT correction is written as a sum over triplets of QDOs,

$$\delta_3 = \frac{-\alpha^3}{32}\mathrm{tr}(\mathcal{T}^3) = \frac{-9\alpha^3}{16}\sum_{\phi>\xi>\mu=1}^{N} \frac{[1+3\cos(\theta_{\mu\xi})\cos(\theta_{\mu\phi})\cos(\theta_{\xi\phi})]}{R_{\mu\xi}^3 R_{\mu\phi}^3 R_{\xi\phi}^3}. \tag{5.8}$$

The angles $\theta_{\mu\xi}$ is given by,

$$\cos(\theta_{\mu\xi}) = \frac{-R_{\mu\xi}^2 + R_{\mu\phi}^2 + R_{\xi\phi}^2}{2R_{\mu\phi}R_{\xi\phi}}. \tag{5.9}$$

5.2.2 Gaussian state CM

The perturbative approach, can be readily compared to the exact solution of the quadratic QDO Hamiltonian, which has a Gaussian ground state, that can be calculated efficiently. As the equilibrium displacement of the QDOs is set to zero, we can describe the properties of the groundstate, solely by the CM. From Eq. (2.34) the groundstate CM can be written in terms of the potential matrix V

$$\gamma_0 = V^{-1/2} \oplus V^{1/2}, \tag{5.10}$$

where the matrix square root is given by $V^{1/2} = O\text{diag}(\sqrt{\lambda_1}, .., \sqrt{\lambda_{3N}})O^T$, and O is the orthogonal matrix that diagonalizes V, where $(V^{-1/2})_{ij} = \langle \hat{\chi}_i \hat{\chi}_j \rangle$ and $(V^{1/2})_{ij} = \langle \hat{\mathcal{P}}_i \hat{\mathcal{P}}_j \rangle$,

$$V^{-1/2} = \underbrace{\begin{pmatrix} \langle \hat{\chi}_1^2 \rangle & \langle \hat{\chi}_1 \hat{\chi}_2 \rangle & \cdots & \langle \hat{\chi}_1 \hat{\chi}_{3N} \rangle \\ \langle \hat{\chi}_2 \hat{\chi}_1 \rangle & \langle \hat{\chi}_2^2 \rangle & \cdots & \vdots \\ \vdots & \vdots & \ddots & \vdots \\ \langle \hat{\chi}_{3N} \hat{\chi}_1 \rangle & \cdots & \cdots & \langle \hat{\chi}_{3N}^2 \rangle \end{pmatrix}}_{3N}, \tag{5.11}$$

$$V^{1/2} = \underbrace{\begin{pmatrix} \langle \hat{\mathcal{P}}_1^2 \rangle & \langle \hat{\mathcal{P}}_1 \hat{\mathcal{P}}_2 \rangle & \cdots & \langle \hat{\mathcal{P}}_1 \hat{\mathcal{P}}_{3N} \rangle \\ \langle \hat{\mathcal{P}}_2 \hat{\mathcal{P}}_1 \rangle & \langle \hat{\mathcal{P}}_2^2 \rangle & \cdots & \vdots \\ \vdots & \vdots & \ddots & \vdots \\ \langle \hat{\mathcal{P}}_{3N} \hat{\mathcal{P}}_1 \rangle & \cdots & \cdots & \langle \hat{\mathcal{P}}_{3N}^2 \rangle \end{pmatrix}}_{3N}. \tag{5.12}$$

Note that we drop the usual superscript for the notation for eigenvalues and eigenvectors of V, i.e $\lambda_i^V \to \lambda_i$, due to the central importance of this eigendecomposition, in this thesis.

As the $d = 3N$ mode Hamiltonian matrix for the QDO model is given by $H = V \oplus \mathbb{1}$, the unique symplectic eigenvalues of the QDO Hamiltonian are given by $\epsilon_i = \sqrt{\lambda_i}$. Hence due to the properties of the trace, the dispersive binding energy can be equivalently written as $E = 3N/2 - (1/2)\text{tr}(V^{1/2})$, also equal to $E = 3N/2 - (1/2)\sum_{i=1}^{3N} \langle \hat{\mathcal{P}}_i^2 \rangle$.

Access to the QDO ground state CM, allows for efficiently extracting entanglement information. The Gaussian tangle $\tau_G(i)$ quantifying the entanglement in a bipartition between mode i and the other $3N-1$ modes in the QDO groundstate can be computed from CM elements via applying the formulae in Eq. (3.28) and Eq. (3.7), using the diagonal elements $(V^{1/2})_{ii}$ and $(V^{-1/2})_{ii}$.

5.2.2.1 Bounds in the QDO CM

Lemma. 2 .- $(V^{1/2})_{ii} \leq 1 \; \forall i \in \{1, 2, ..., 3N\}$.

Proof. The matrix V is a symmetric matrix, $V = V^T$, with positive eigenvalues λ. It is therefore diagonalized by a orthogonal matrix, O ($OO^T = \mathbb{1}$). The diagonal elements of the matrix square root of V are given by

$$(V^{1/2})_{ii} = \sum_{j=1}^{3N} O_{ij}^2 \sqrt{\lambda_j}, \quad \sum_{j=1}^{3N} O_{ij}^2 = 1. \tag{5.13}$$

The diagonal elements of $V^{1/2}$ are given by a *convex combination* of the square root of the eigenvalues of V. We apply Jensen's inequality [157], which states that

$$\left(\sum_{j=1}^{3N} O_{ij}^2 \sqrt{\lambda_j}\right)^2 \leq \sum_{j=1}^{3N} O_{ij}^2 \left(\sqrt{\lambda_j}\right)^2, \tag{5.14}$$

which gives the result, as by definition,

$$\sum_{j=1}^{3N} O_{ij}^2 \lambda_j = V_{ii} = 1. \tag{5.15}$$

Lemma. 3 .-The dispersive binding energy is always *net* attractive , i.e $E \geq 0$.

Proof. This follows from Lemma. 1, as the bond energy is

$$E = \frac{3}{2}N - \frac{1}{2}\sum_{i=1}^{3N} (V^{1/2})_{ii}, \tag{5.16}$$

where $E \geq 0$, directly follows from the fact that $(V^{1/2})_{ii} \leq 1 \forall i \in \{1, .., 3N\}$.

Lemma. 4 .- $(V^{-1/2})_{ii} \geq [(V^{1/2})_{ii}]^{-1}$, $\forall i \in \{1, .., 3N\}$.

Proof. As $V^{1/2}$ is the unique symmetric positive definite matrix such that $(V^{1/2})^2 = V$ [158], there is a unique symmetric positive matrix C where $V^{1/2} = CC$ and thus also $V^{-1/2} = (C^{-1})^2$. Note that as C is a symmetric matrix, $C_{ij} = C_{ji}$ and $(C^{-1})_{ij} = (C^{-1})_{ji}$. We can thus employ the Cauchy-Schwartz inequality to complete the proof,

$$\underbrace{\left(\sum_{j=1}^{3N} C_{ij}(C^{-1})_{ji}\right)^2}_{=1} \leq \underbrace{\left(\sum_{j=1}^{3N} C_{ij}^2\right)}_{(V^{1/2})_{ii}} \underbrace{\left(\sum_{j=1}^{3N} (C^{-1})_{ji}^2\right)}_{(V^{-1/2})_{ii}}. \tag{5.17}$$

Note that lemma 3, further follows from the constraint on the CM in Eq. (2.18) and Eq. (2.32), where the latter sets the constraint on the symplectic eigenvalues of the CM. A single mode reduced CM is given by the diagonal matrix, $\text{diag}(\langle\hat{\chi}_i\hat{\chi}_i\rangle, \langle\hat{\mathcal{P}}_i\hat{\mathcal{P}}_i\rangle)$, the single unique symplectic eigenvalue of which is given by $\epsilon_i = \sqrt{\langle\hat{\chi}_i\hat{\chi}_i\rangle\langle\hat{\mathcal{P}}_i\hat{\mathcal{P}}_i\rangle}$. Hence in order for Eq. (2.32) to hold, $\langle\hat{\chi}_i\hat{\chi}_i\rangle\langle\hat{\mathcal{P}}_i\hat{\mathcal{P}}_i\rangle = (V^{-1/2})_{ii}(V^{1/2})_{ii} \geq 1$.

5.3 Multipartite Gaussian Entanglement and Energy

5.3.1 Reduced tangle

We use the definition of the tangle to introduce the reduced tangle,

$$\tilde{\tau}_G(i) = g(\tau_G(i)), \quad \text{where} \quad g(x) = \frac{x(1+\sqrt{x})^2}{(1+2\sqrt{x})^2}. \tag{5.18}$$

The function $g(x)$ is monotonically increasing for all positive x (see Fig. B.1 and lemma B.3), ensuring the reduced tangle is an entanglement monotone under LOCC [159].

5.3.2 Reduced tangle bound on the MB energy

Having defined the reduced tangle in terms of the Gaussian tangle, we have a new proper measure of pure-state bipartite entanglement. Here we will use this entanglement measure, to connect the sum of the entanglement of all $3N$ modes in the QDO ground-state, with the infinite series of energy terms in Eq. (5.4).

For a QDO Hamiltonian of the form in Eq. (5.2) and given that $\alpha\|\mathcal{T}\|_2 < 1$,

$$\tilde{\tau}_G = \sum_{i=1}^{3N} \tilde{\tau}_G(i) \leq \sum_{k=2}^{\infty} (k-1)\delta_k, \tag{5.19}$$

where δ_k is the kth body contribution to the dispersive binding energy, as per Eq. (5.4).

Proof-. We can write $\Delta_i = \langle \hat{\chi}_i \hat{\chi}_i \rangle \langle \hat{\mathcal{P}}_i \hat{\mathcal{P}}_i \rangle - 1$. From the definition of the tangle $\tau_G(i)$ and Δ_i,

$$\tilde{\tau}_G = \frac{1}{4} \sum_{i=1}^{3N} \Delta_i = \sum_{i=1}^{3N} g(\tau_G(i)). \tag{5.20}$$

By defining $\delta_i^{\chi} = \langle \hat{\chi}_i^2 \rangle - 1$, $\delta_i^{\mathcal{P}} = 1 - \langle \hat{\mathcal{P}}_i^2 \rangle$, we write Δ_i as follows,

$$\Delta_i = \delta_i^{\chi} - \delta_i^{\mathcal{P}} - \delta_i^{\chi}\delta_i^{\mathcal{P}}. \tag{5.21}$$

By using the unitary invariance of the trace operator and writing $(\lambda_i)^{\pm 1/2} = (1+\alpha t_i)^{\pm 1/2}$, the binomial expansion (see appendix B.2) of $(\lambda_i)^{\pm 1/2}$ in small parameter αt_i is

$$\sum_{i=1}^{3N} \delta_i^{\chi} = \sum_{i=1}^{3N} \left(\left(\sqrt{\lambda_i} \right)^{-1} - 1 \right) = \sum_{k=2}^{\infty} \binom{-0.5}{k} \alpha^k \mathrm{tr}(\mathcal{T}^k), \tag{5.22}$$

and

$$\sum_{i=1}^{3N}\delta_i^{\mathcal{P}} = \sum_{i=1}^{3N}\left(1-\sqrt{\lambda_i}\right) = -\sum_{k=2}^{\infty}\binom{0.5}{k}\alpha^k \mathrm{tr}(\mathcal{T}^k). \tag{5.23}$$

By inserting Eq. (5.22) and Eq. (5.23) into Eq. (5.21) and Eq. (5.20), then simplifying the resultant expression we arrive at

$$\tilde{\tau}_G = \sum_{k=2}^{\infty}(k-1)\delta_k - \frac{1}{4}\sum_{i=1}^{3N}\delta_i^{\chi}\delta_i^{\mathcal{P}}. \tag{5.24}$$

As $\delta_i^{\chi} = \langle\hat{\chi}_i^2\rangle - 1 \geq 0$ and $\delta_i^{\mathcal{P}} = 1 - \langle\hat{\mathcal{P}}_i^2\rangle \geq 0$, both $\forall i \in \{1,..,3N\}$, due to a combination of lemma 5.2.2.1 and lemma 5.2.2.1,

$$\Delta_i \leq \delta_i^{\chi} - \delta_i^{\mathcal{P}}, \forall i \in \{1,..,3N\}. \tag{5.25}$$

By applying Eq. (5.25) to Eq. (5.24), we get our final result in Eq. (5.19).

5.3.3 Pairwise tangle bound on MB energy

Using the definition of the reduced tangle and the bound in Eq. (5.19), we here extend the bound in Eq. (5.19), to connect the net pairwise tangle in the QDO groundstate, to the pairwise and many-body bond energies.

Proof-. The lemmas in appendix B.3 proving properties of the function $g(x)$, allow for relating the r.h.s of the Eq. (5.19) to the pairwise tangle. Given that $g(x)$ is a subadditive function (i.e $g(x+y) \leq g(x) + g(y)$ see lemma B.3 for proof)

$$g\left(\tau_G = \sum_{i=1}^{3N}\tau_G(i)\right) \leq \sum_{i=1}^{3N} g(\tau_G(i)) = \tilde{\tau}_G. \tag{5.26}$$

This sub-additive property of $g(x)$ can be extend to the inequality in Eq. (5.19),

$$g(\tau_G) \leq \tilde{\tau}_G \leq \sum_{k=2}^{\infty}(k-1)\delta_k. \tag{5.27}$$

The sum of each of the $3N$ monogamy inequalities, see Eq. (3.32) and Eq. (3.34) in the QDO ensemble are given by

$$\tau_G = \sum_{i=1}^{3N}\tau_G(i) \geq \sum_{\substack{i,j=1\\ j\neq i}}^{3N} \underbrace{f(-\langle\hat{\chi}_i\hat{\chi}_j\rangle\langle\hat{\mathcal{P}}_i\hat{\mathcal{P}}_j\rangle)}_{\tau_G^{\mathrm{sys}}(i:j)} \geq \sum_{\substack{i,j=1\\ j\neq i}}^{3N}\tau_G(i:j), \tag{5.28}$$

Inserting (5.28) into (5.27) and assuming $\alpha||\mathcal{T}||_2 < 1$, we retrieve

$$g\left(\sum_{\substack{i,j=1\\ j\neq i}}^{3N}\tau_G(i:j)\right) \leq g\left(\sum_{\substack{i,j=1\\ j\neq i}}^{3N}\tau_G^{\mathrm{sys}}(i:j)\right) \leq \sum_{k=2}^{\infty}(k-1)\delta_k. \tag{5.29}$$

In addition to this bound and the bound in Eq. (5.19), we derive similar bounds in terms of the negativity in appendix B.4 and some other noteworthy entanglement bounds in B.5. In the next section, we illustrate the tightness of the entanglement-energy relation derived here, for different exemplary systems. This relation further provides an analytic justification for applying the monogamy/promiscuity framework developed in the previous chapter, to understand the MB energy in terms of the entanglement.

5.4 Trimer, Chains and Extended Lattices

5.4.1 Relative density

We study the entanglement and energy in terms of a dimensionless parameter $\rho = R/\alpha^{1/3}$, with $R = \min_{\mu,\xi} R_{\mu\xi} \forall \mu \neq \xi$. In addition to ρ, the entanglement and energy depend on the geometry of the fixed equilibrium positions of the N QDOs. By using the simple cubic lattice as a reference frame, the authors in [49], estimated the region $2.3 \leq \rho \leq 3$, to be an interval of primary importance, for solids and liquids.

For the two mode Hamiltonian setup in Sec. 4.2, $\kappa < 1$. This constraint enforced the definite positivity constraint on the Hamiltonian matrix. In the same way, we are here restricted to focus on regimes where $\rho > \rho_c$, for a critical value ρ_c. At ρ_c, $\min(\mathrm{eig}(V)) = 0$, hence V is no longer a positive definite matrix. This is a limitation on the model, as for very dense systems the harmonic response of the charge density breaks down, as well as the validity of the multipole expansion and thus the leading order dipole coupling between QDOs.

5.4.2 Entanglement distribution index

In the ground state of the two-mode Hamiltonian $\hat{H}_{ij} = \frac{1}{2}(\hat{\chi}_i + \hat{\chi}_j + \hat{\mathcal{P}}_i + \hat{\mathcal{P}}_j) + \alpha \mathcal{T}_{ij} \hat{\chi}_i \hat{\chi}_j$, the tangle between modes i and j is given, using the expressions in Eq. (4.7), as

$$\tau_G^{\mathrm{ref}}(i:j) = \frac{(\sqrt{\epsilon_+/\epsilon_-} - 1)^2}{4}, \quad \text{with} \quad \epsilon_\pm = \sqrt{1 \pm \alpha |\mathcal{T}_{ij}|}. \tag{5.30}$$

We label this pairwise tangle, computed from the ground state of the *bipartite* Hamiltonian $\hat{H}_{ij}$, as the reference tangle $\tau_G^{\mathrm{ref}}(i:j)$. It captures the entanglement shared between modes i and j due to the dimensionless dipole bond $\alpha \mathcal{T}_{ij}$, as if all other modes were *screened away*.

In contrast, in the ground state of the *multipartite* QDO Hamiltonian in Eq. (5.2), the upper bound on the pairwise tangle is

$$\tau_G^{\mathrm{sys}}(i:j) = f\big(-(V^{1/2})_{ij}(V^{-1/2})_{ij}\big) \geq \tau_G(i:j), \quad \forall i \neq j, \tag{5.31}$$

as given in Eq. (3.34) by inserting the off-diagonal CM elements. The system tangle $\tau_G^{\mathrm{sys}}(i:j)$ accounts for indirect contributions and collective correlations present in the full ground state.

In order to numerically demonstrate the geometric and ρ dependence of the monogamy constraints on the pairwise tangle, contained within a given two QDO subsystem, we define the two QDO entanglement distribution index (EDI),

$$\delta_{\tau_G}^{\mu,\xi} = \frac{\sum_{i,j} \tau_G^{\mathrm{sys}}(i:j)}{\sum_{i,j} \tau_G^{\mathrm{ref}}(i:j)} \quad \forall i \in \mu, j \in \xi. \tag{5.32}$$

The EDI quantifies how monogamy constraints shape the entanglement distribution in a two QDO subsystem. For sufficiently weak interactions only the lowest two levels of each QDO can be occupied. The monogamy constraint can then limit the pairwise tangle leading to $\delta_{\tau_G}^{\mu,\xi} < 1$, reflecting the monogamous behavior of entanglement in qubit systems. For stronger interactions higher lying QDO levels may be occupied thus increasing the size of the accessible local Hilbert space and the overall amount of shareable entanglement. In this promiscuous regime $\delta_{\tau_G}^{\mu,\xi} > 1$. See Sec. 4.3, for the behavior of $\tau_G^{\mathrm{sys}}(i:j)/\tau_G^{\mathrm{ref}}(i:j)$ in the simple three mode exmaple.

5.4.3 Trimer

5.4.3.1 Trimer setup

Illustration of the three QDO trimer setup, in Fig. 5.2 *a*). The coordinates of the three QDOs 1, 2 and 3 are $(0,0,0)$, $(R\sin[\theta/2], R\cos[\theta/2], 0)$ and $(2R\sin[\theta/2], 0, 0)$, where $R_{12} = R_{23} = R$ and $\theta \in \{\pi/3, \pi\}$. The trimer depends on a dimensionless nearest neighbor separation ρ and geometry, θ. The ρ and θ dependence can be seen explicity by rewriting dipole-dipole interaction matrix in Eq. (5.1) as

$$e_1^T \mathcal{T} e_2 = \rho^{-3} \left(\mathbb{1}_3 - \begin{bmatrix} \sin^2[\theta/2] & \cos[\theta/2]\sin[\theta/2] & 0 \\ \cos[\theta/2]\sin[\theta/2] & \cos^2[\theta/2] & 0 \\ 0 & 0 & 0 \end{bmatrix} \right), \tag{5.33}$$

where $\rho = R/\alpha^{1/3} = R_{12}/\alpha^{1/3} = R_{23}/\alpha^{1/3}$.

Due to the symmetry of the trimer the dipole sub-matrix, connecting QDOs 2 and 3 is identical to that coupling QDOs 1 and 2. Likewise the dipole coupling matrix

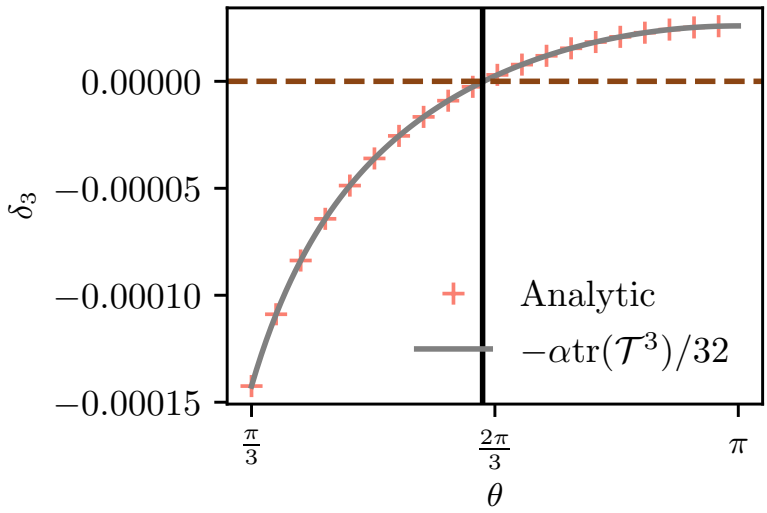

Figure 5.1: AT potential in the trimer at $\rho = 2.60$ (see Sec. 5.4, for a definition of ρ and the trimer). The orange crosses show δ_3 computed via the r.h.s of Eq. (5.8), whereas the solid grey curve shows δ_3 computed by the l.h.s of Eq. (5.8).

between QDOs 1 and 3 can be written explicitly in terms of θ and ρ as

$$e_1^T \mathcal{T} e_3 = \rho^{-3} \left(\frac{1}{8 \sin^3[\theta/2]} \mathrm{diag}(-2, 1, 1) \right). \tag{5.34}$$

Importantly whilst we have shown how to pull out a factor of ρ^{-3} from the dipole interaction matrix of the 3 QDO trimer system, this technique is possible for any arbitrary N QDO arrangement of homogenous QDOs i.e identical frequency and polarizabilities.

5.4.3.2 Axilrod-Teller in the trimer

In Fig. 5.1, we show the correspondence for the AT potential computed via the expression for $\delta_3 = -\alpha \mathrm{tr}(\mathcal{T}^3)/32$ and the analytic formulae in the r.h.s of Eq. (5.8), which for the trimer setup has a sole angular depedance on θ. As has been well known since the days of Axilrod and Teller, the AT trimer correction is attractive in the linear arrangement and repulsive in the triangular configuration. The vertical black line in Fig. 5.1, shows where $\delta_3 = 0$, where to the right of the black line the AT potential is positive and to the left of the black line, the AT potential is negative. Whilst in Fig. 5.1, we have looked at a particular ρ value i.e $\rho = 2.3$, the sign depedance of δ_3 is *indepedant* of the coupling strength, with the latter only affecting the magnitude of the correction.

5.4.3.3 EDI and MB effects

We consider three QDOs (trimer); see Fig. 5.2 a) for a depiction of the setup. We focus on the EDI between QDOs 1 and 2 in the trimer. By symmetry, this is identical to the subsystem of QDOs 2 and 3, highlighted by the two QDOs encircled by the dashed line within the three-QDO trimer in Fig. 5.2 a).

In Fig. 5.2 we show a heatmap of δ_{MB}, plotted as a function of 100 θ values for $\theta \in \{\pi/3, \pi\}$, and 100 ρ values for $\rho \in \{1.45, 4\}$. Fig. 5.2 shows that both the geometric and ρ dependence of the entanglement distribution directly correlates with the MB potential in the trimer. The parameter space of the trimer is partitioned into its promiscuous and monogamous regions, separated by the dotted red line. The boundary between these two regions approximates the locus of points that separate the attractive and repulsive MB energies. For any $\rho \geq 2.3$, the deviation in θ between the two boundaries is less than 1.2% of the θ value where $\delta_{\mathrm{MB}} = 0$. This correspondence becomes exact in the limit $\rho \to \infty$, where the boundary between the promiscuous and monogamous regimes asymptotically overlaps with the parameter space where the AT potential vanishes, i.e., $\delta_3 = 0$, indicated by the horizontal black line. We thus find that the nearest neighbor EDI well matches the sign of the MB energy. Fig 5.3 further illustrates the tight correlation between the behavior of the EDI in a) and MB potential in b), shown for a select few angles.

5.4.3.4 Reduced tangle bounds

Next we show the tightness of the bound in Eq. (5.19), for both the linear and triangular geometries. Fig. 5.4 shows the convergence to the bound in Eq. (5.19) for different couplings strengths. Fig. 5.4 *a*) shows that for $\rho = 2.6$, $\tilde{\tau}_G < \delta_2 + 2\delta_3 + 3\delta_4$, for both the linear and triangular geometries, where $\tilde{\tau}_G < \delta_2$ in the triangular case, whereas $\tilde{\tau}_G > \delta_2$ in the linear geometry. In comparison Fig. 5.4 *b*), shows that for strong coupling, $\tilde{\tau}_G > \delta_2$, for both arrangements. Taking δ_2 away from both sides of Eq. (5.19), shows that $\tilde{\tau}_G - \delta_2 \leq \sum_{k=3}^{\infty}(k-1)\delta_k$. Comparing this bound with the definition of the MB energy and the form of E in Eq. (5.4) explains the qualitative correspondence between the dashed-dotted black line in Fig. 5.2 and the sign of δ_{MB}, where the former divides the parameter space, into the regions where $\tilde{\tau}_G < \delta_2$ (below) and the regions where $\tilde{\tau}_G > \delta_2$.

The close correspondence between the horizontal lines and the markers at high l in Fig. 5.4, illustrate the tightness of the bound in Eq. (5.19). This is the case even at strong couplings, as can be seen in Fig. 5.4 *b*). The residual difference between

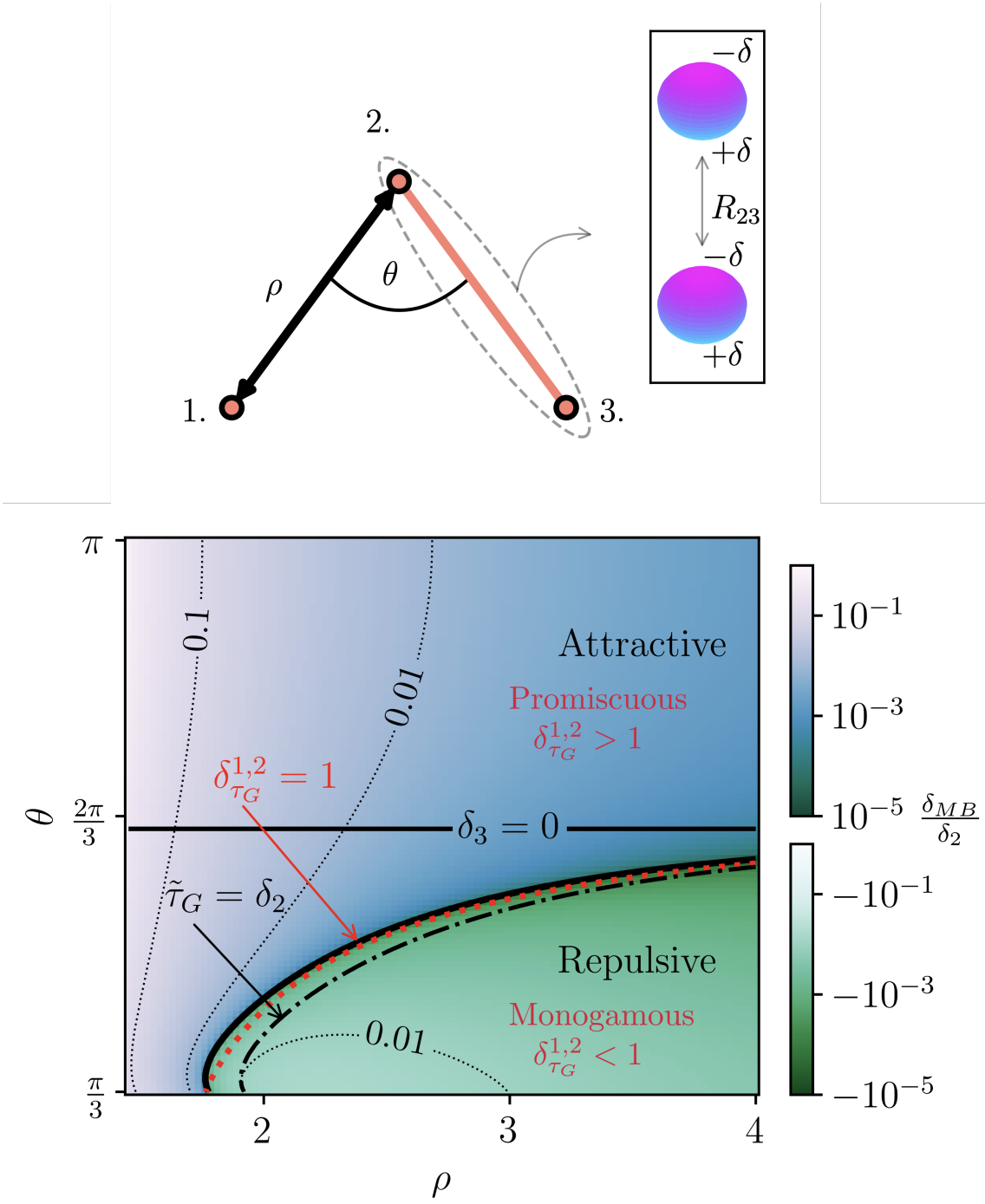

Figure 5.2: (Top) Depiction of the dipole interacting trimer setup. The correlated charge density fluctuations, are shown by the instantaneous dipoles $\pm\delta$. (Bottom) Above the red dotted line the sum of the pairwise tangle shared between the nearest neighbor QDOs behaves promiscuously, whereas below it behaves monogamously. The monogamy/promiscuity boundary overlaps the black line where MB energy corrections vanish and the pairwise additive approximation holds; above which MB corrections are attractive and below which are repulsive; both shown as heat-maps, plotted on a log scale.

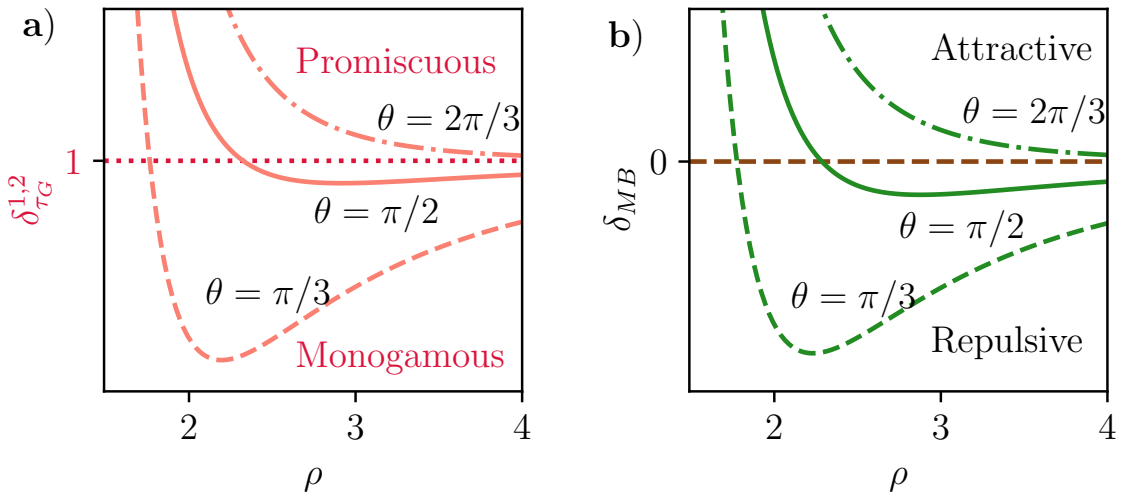

Figure 5.3: **a)** Behavior of the nearest neighbor EDI, $\delta^{1,2}_{\tau_G}$, at different angles, with the dotted red line separating promiscuous and monogamous regions. **b)** Behavior of the MB potential δ_{MB}, shown for the same three angles as shown for **a)**.

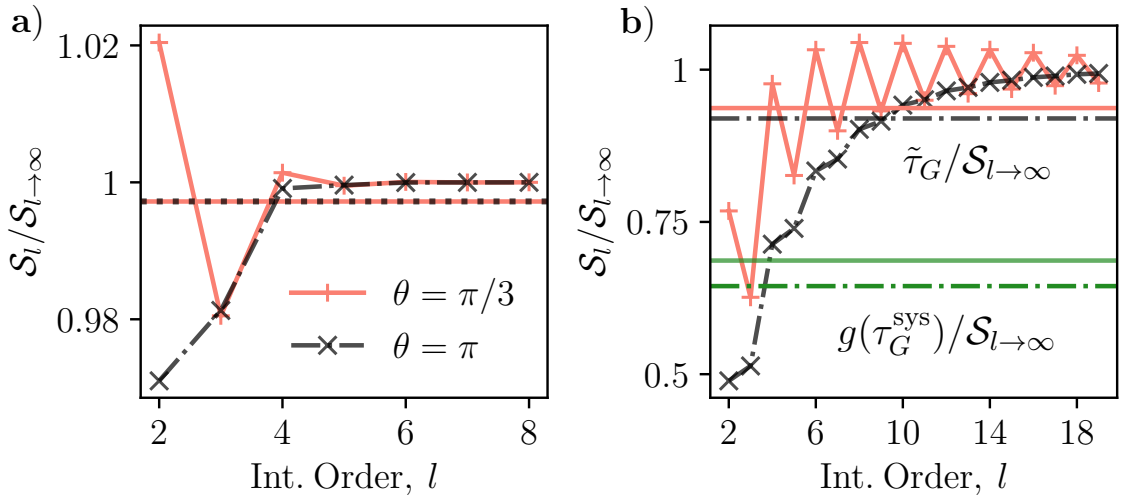

Figure 5.4: In **a) – b)**, where $\rho = 2.60$ and $\rho = 1.55$ respectively, the cross/plus symbols show S_l, where $S_l = \sum_{k=1}^{l}(k-1)\delta_k$, normalized by $S_{l\to\infty} = \sum_{k=1}^{\infty}(k-1)\delta_k$. The latter is computable from the CM matrix elements, see Sec. 5.3 for calculation details. The dashed-dotted (black) and solid (orange) horizontal lines show the normalized value of the reduced tangle, i.e $\tilde{\tau}_G/S_{l\to\infty}$ for the respective ρ and θ values (dashed line for $\pi/3$ and dotted line for π). The dashed-dotted (green) and solid (green) horizontal lines show the normalized value of the total ground state maximal pairwise tangle. i.e $g(\tau_G^{\text{sys}})/S_{l\to\infty} = g(\sum_{ij}\tau_G^{\text{sys}}(i:j))/S_{l\to\infty}$.

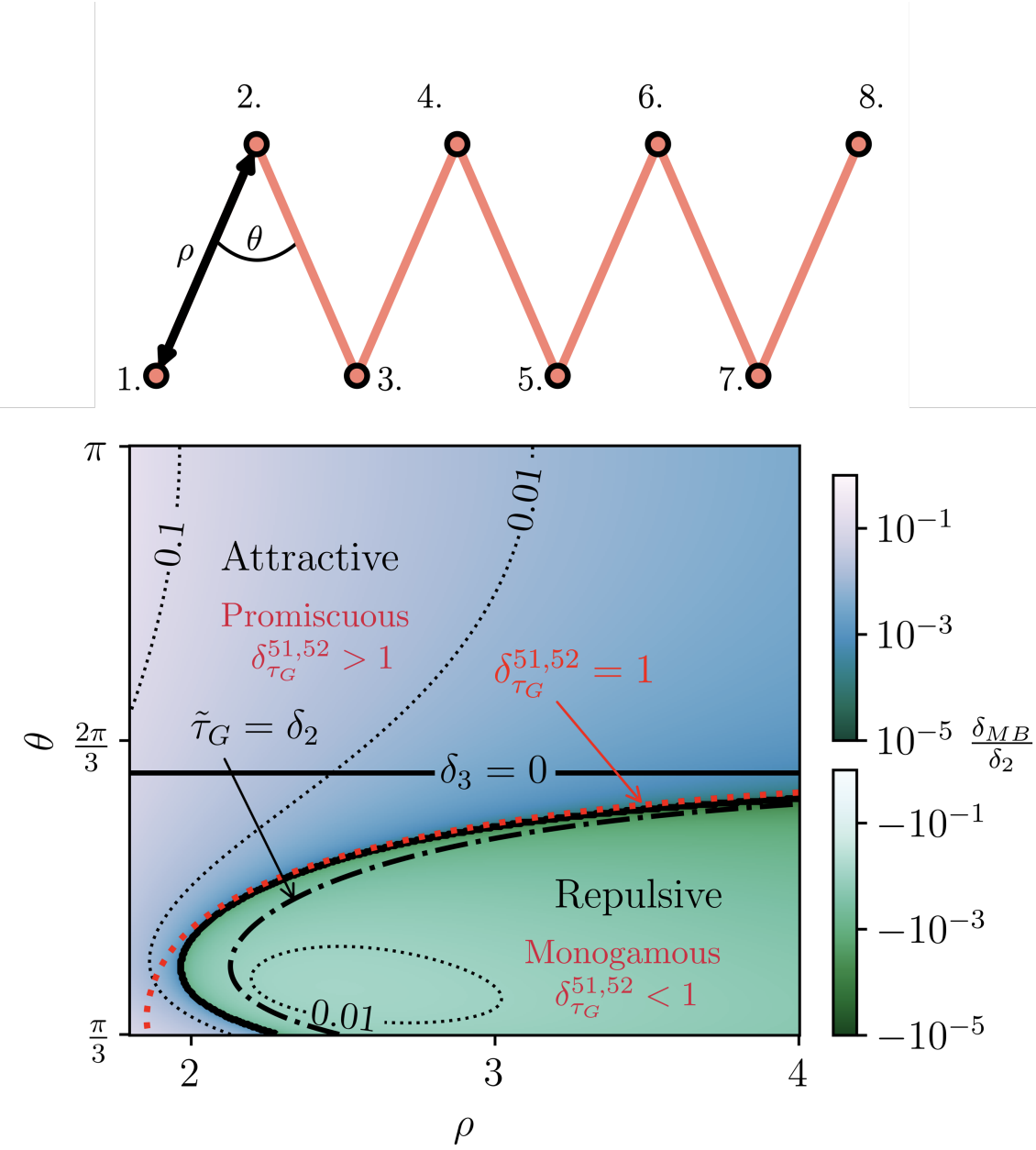

Figure 5.5: (Top) Illustration of the chain setup, with chain geometry depending on θ. (Bottom) Above the red dotted line the sum of the pairwise tangle shared between the nearest neighbor QDOs at the center of the chain behaves promiscuously, whereas below it behaves monogamously. For $\rho \geq 2$, the monogamy/promiscuity boundary overlaps the black line where MB energy corrections vanish and the pairwise additive approximation holds; above which MB corrections are attractive and below which are repulsive; both shown as heat-maps, plotted on a log scale.

the l.h.s and r.h.s in the bound on the pairwise tangle in Eq. (5.29) is shown in Fig. 5.4 *b*), by the position of dashed and solid green horizontal lines, relative to where $\mathcal{S}_l/\mathcal{S}_{l\to\infty} = 1$.

5.4.4 Linear and zigzag chain

Having established the close correlation between the monogamous or promiscuous behavior of the entanglement distribution and the sign of the MB effects in the trimer, we extend this analysis to a chain of QDOs, as depicted in Fig. 5.5.

Given that $R_{\mu,\mu+1} = R$, the coordinates of the QDOs are as follows: $(0,0,0)$, $(R\sin[\theta/2], R\cos[\theta/2], 0)$, $(2R\sin[\theta/2], 0, 0)$, $(3R\sin[\theta/2]), R\cos[\theta/2], 0)$, ... , $((N+1)R\sin[\theta/2]$, $R\cos[\theta/2], 0)$. Fig. 5.5, depicts the chain in it's zigzag configuration, where $\theta = \pi/3$. Here we focus on the MB effects and entanglement properties of the chain, going from the linear to zigzag configuration, determined by θ.

5.4.4.1 EDI and MB effects

Figure 5.5 shows a heat map of $\delta_{\mathrm{MB}}/\delta_2$ as a function of ρ and θ in the linear–zigzag chain, where we set $N = 100$. We consider 400 values of θ in the range $\theta \in \{\pi, \pi/3\}$ and 400 values of ρ in the range $\rho \in \{4, 1.8\}$. Note that in the trimer the lowest ρ value considered was $\rho = 1.45$, whereas here it is $\rho = 1.8$. This difference arises from the higher critical value ρ_c for the chain compared to the trimer. Moreover, we sample 400 values of both θ and ρ for the chain, compared to 100 values each in the trimer, in order to capture the slower convergence to a smooth boundary separating positive and negative δ_{MB} values.

We define the promiscuous or monogamous entanglement distribution in the quasi-1D chain, based on the EDI of two QDOs, chosen to be close to the center of the chain. Note that here the open boundary conditions mean that there are discrepancies, in the pairwise tangle shared between nearest neighbor QDOs near the end of the chain, compared with pairs of QDOs near the center. See appendix B.7 for more details on the inhomogeneous distributed of entanglement between pairs of QDOs.

Fig. 5.5 shows how the parameter space of the linear-zigzag chain is partitioned into regions, separated by the dotted red line, where $\delta_{\tau_G}^{N/2+1,N/2+2}$ is either enhanced (above) or suppressed (below). The red dotted line, partitioning the parameter space in promiscuous and monogamous entanglement, as a function of ρ and θ is given by $\delta_{\tau_G}^{51,52} = 1$, in the 100 QDO chain. For $\rho \geq 2$, this red dotted line closely overlaps where $\delta_{\mathrm{MB}} = 0$. At $\rho = 2.3$, the deviation in θ value between the two boundaries is less than

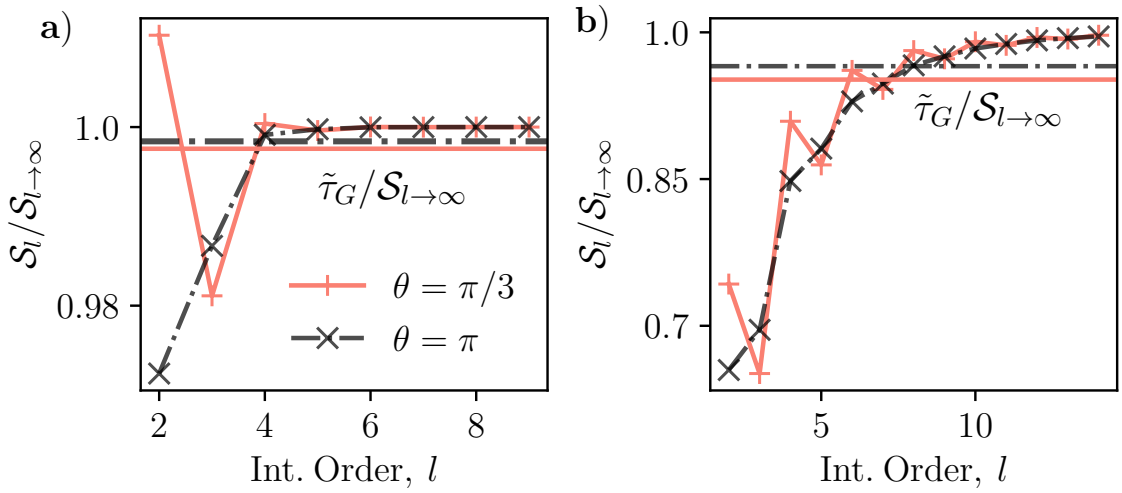

Figure 5.6: The cross/plus symbols show S_l, where $S_l = \sum_{k=1}^{l}(k-1)\delta_k$, normalized by $S_{l\to\infty} = \sum_{k=1}^{\infty}(k-1)\delta_k$, where $\rho = 3$ in **a)** and $\rho = 1.85$ in **b)**. This is shown for the linear (cross symbols connected by dashed dotted lines) and zigzag chain (plus symbols connected by solid orange line). The horizontal lines show the reduced tangle, normalized by $S_{l\to\infty}$, for the different configurations. For large l, the series $S_l = \sum_{k=1}^{l}(k-1)\delta_k$ converges to lie above the horizontal lines, thus verifying the bound in Eq. (5.19), for the linear and zigzag chains.

1% of the θ value where the MB effects vanish. Away from strong couplings, we thus see how the EDI in a central pair of QDOs in the chain, well captures the sign of the MB potential.

5.4.4.2 Reduced tangle bounds

The region of the phase space where $\tilde{\tau}_G < \delta_2$ ($\tilde{\tau}_G > \delta_2$) approximates where $\delta_{\text{MB}} < 0$ ($\delta_{\text{MB}} > 0$), with the black dashed dotted line showing where $\tilde{\tau}_G = \delta_2$. Note that the region of phase space where $\tilde{\tau}_G < \delta_2$ is completely enclosed by the repulsive MB region, as was the case for the trimer. In Fig. 5.6, we highlight the tightness of the bound in Eq. (5.19), for the linear and zigzag chains, at both strong and weak coupling. In Fig. 5.6 a), we see that at $\rho = 3.0$, $\tilde{\tau}_G < \delta_2$ in the zigzag chain whereas $\tilde{\tau}_G > \delta_2$ in the linear chain. In comparison in Fig. 5.6 b), $\tilde{\tau}_G < \delta_2 + 2\delta_3 + 3\delta_4$, for both geometries at $\rho = 1.85$.

5.4.5 2D crystal lattices

The Gaussian state framework can be directly extended to arbitrary assemblies such as layered systems and 3D lattices, which we consider next.

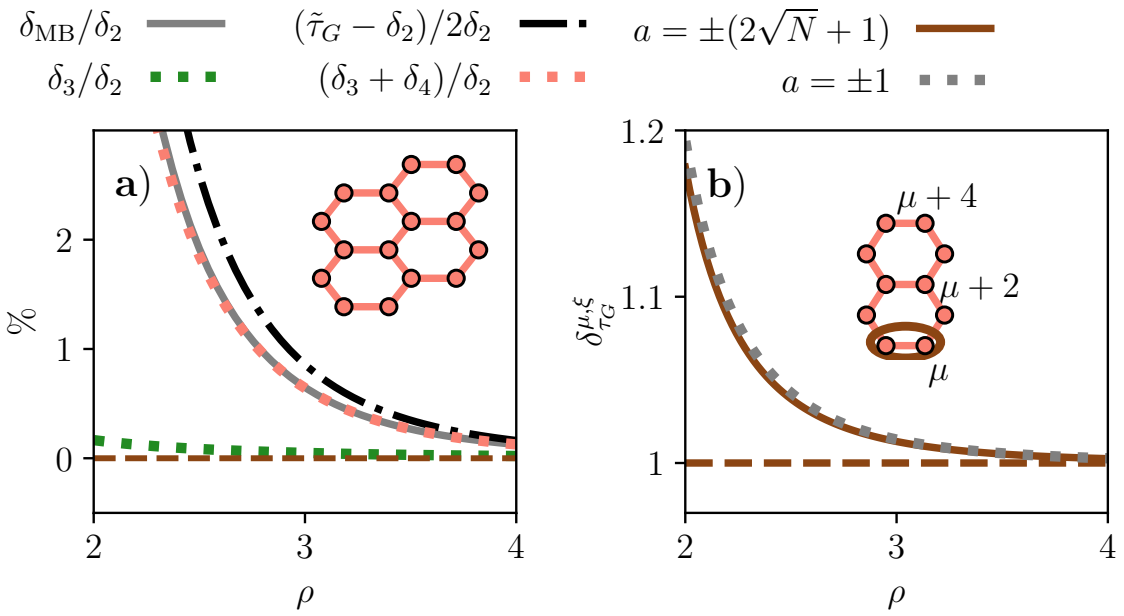

Figure 5.7: Behavior of the MB effects and entanglement on the $N = 47 \times 47 \times 2$ honeycomb lattice. **a)** The solid line shows the MB effects, the small green dotted line the AT correction, the large orange dotted line shows four-body corrections added to the AT potential, the dashed dotted line shows the deviation between the sum of the reduced tangle of each of the $3N$ modes and the pairwise bonding energy, $(\tilde{\tau}_G - \delta_2)/2$, with the factor of 1/2 included as $(\tilde{\tau}_G - \delta_2)/2 \to \delta_3$ for $\rho \to \infty$. All the curves have been normalized by the pairwise bond energy and have been plotted as a function of the dimensionless nearest neighbor separation ρ. **b)** The EDI between μ and $\xi = \mu + a$ on the honeycomb lattice. The dashed horizontal line shows the monogamy/promiscuity boundary, with the monogamous region lying below and the promiscuous region above. The ordering of the QDOs on the 2D lattices is shown in the inset, where $\mu = 2256$. All lattices calculations have been preformed with open boundary conditions.

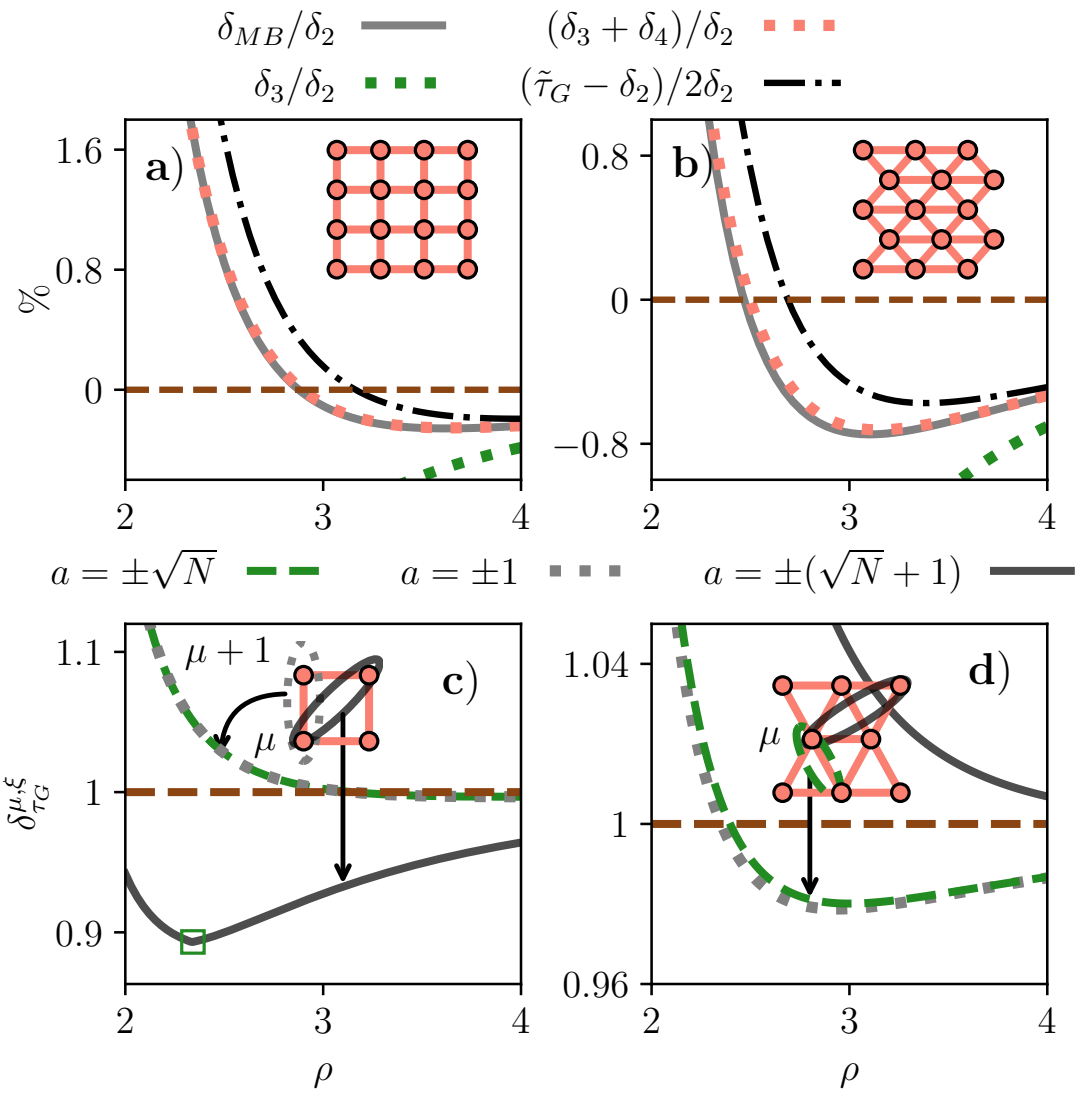

Figure 5.8: Behavior of MB effects and entanglement on **a)** the $N = 71 \times 71$ square lattice and **b)** the $N = 71 \times 71$ triangular lattice. In **a)**–**b)**, the same quantities are plotted as those shown for the honeycomb lattice in Fig. 5.7. All the curves have been normalized by the pairwise bond energy and have been plotted as a function of the dimensionless nearest neighbor separation ρ. The EDI between μ and $\xi = \mu + a$ on the two-dimensional lattices is shown in **c)**–**d)**. The dashed horizontal line indicates the monogamy/promiscuity boundary for the respective lattices, with the monogamous region lying below and the promiscuous region above. The ordering of the QDOs on the 2D lattices is shown in the insets of **b)**–**c)**, with $\mu = 2520$ in both **c)**–**d)**. The open green square in **c)** marks the point where the PPT criterion ensures $\tau_G(3\mu : 3\xi) = 0$. All lattices calculations have been preformed with open boundary conditions.

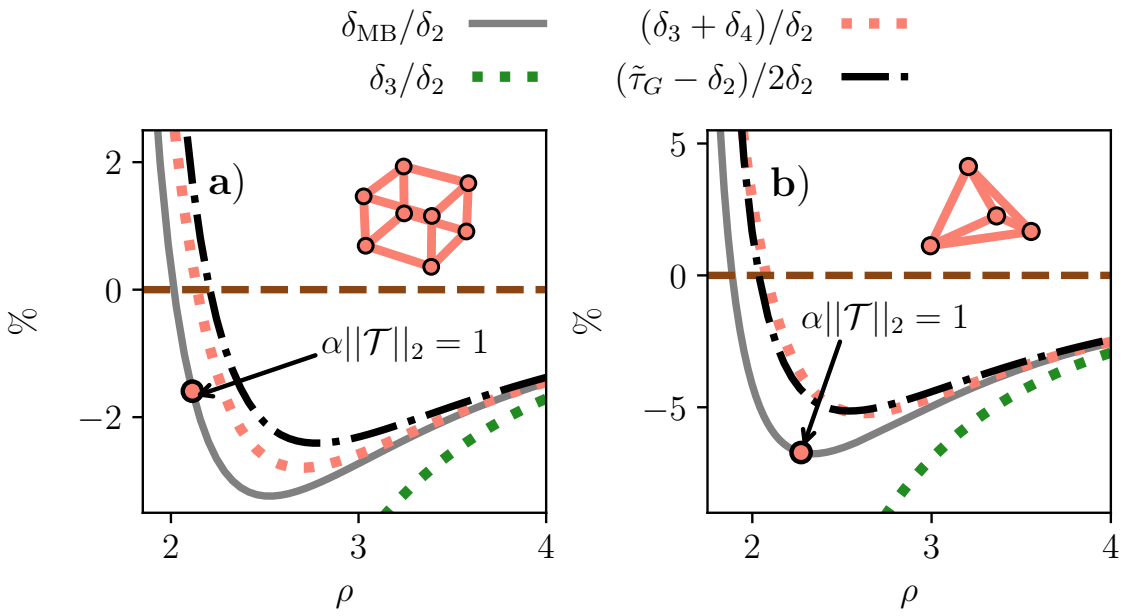

Figure 5.9: Behavior of the MB effects and entanglement on **d)** $N = 19\times19\times19$ cubic lattice and **h)** $N = 4\times12\times12\times12$ pyrochlore lattice. The same quantities are plotted as those shown for the 2D crystal lattices in Fig. 5.7 and Fig. 5.8 . All the curves have been normalized by the pairwise bond energy and have been plotted as a function of the dimensionless nearest neighbor separation ρ. All lattices calculations have been preformed with open boundary conditions.

5.4.5.1 EDI and MB effects

The features of the trimer, shown in Fig. 5.2, can be used to explain the sign of the MB contributions in the more complex 2D lattices, shown in Fig. 5.7 and Fig. 5.8. At weak coupling, the sign of the MB effects are determined by the AT potential in the lattices. The honeycomb lattice has a positive and negligible AT potential, following from where $\delta_3 = 0$ in Fig. 5.2 c), where the primitive translation vectors of the honeycomb lattice form an angle of $2\pi/3$. As the honeycomb lattice has a negligible AT potential, the MB effects in this lattice geometry only become visible through higher order terms, as can be seen in Fig. 5.7. Fig. 5.7 **b)** displays the EDI for nearest- and next-nearest-neighbor QDO pairs near the center of honeycomb lattice. In the honeycomb lattice, promiscuous entanglement sharing persists among its three nearest neighbors across all ρ values, reflecting its exclusively attractive MB potential.

In Fig. 5.8a)–b), where the AT potential is repulsive, a sign change occurs at strong coupling and the MB effects become attractive. A similar sign change is observed in the trimer in Fig. 5.2, as a function of ρ, for all geometries with repulsive AT corrections. Figure 5.8a)–b) further shows that $(\tilde{\tau}_G - \delta_2)/2 \approx \delta_{\mathrm{MB}}$ on all lattices at $\rho = 4$, as indicated by the overlap of the solid and dash-dotted lines. Moreover, $(\tilde{\tau}_G - \delta_2)/2 > \delta_{\mathrm{MB}}$ for all ρ values shown. Similar behavior is observed in the trimer [Fig. 5.2], where the dash-dotted line corresponding to $\tilde{\tau}_G = \delta_2$ lies within the repulsive (green) region, where $\delta_{\mathrm{MB}} < 0$. This can be understood from a rearrangement of Eq. (5.19), as $(\tilde{\tau}_G - \delta_2)/2 \leq \delta_3 + (3/2)\delta_4 + \ldots$, while Fig. 5.8 a)-b) further shows that $\delta_{\mathrm{MB}} \approx \delta_3 + \delta_4$ on the lattices. Appendix B.8 demonstrates that, in the trimer, the boundary separating attractive and repulsive MB effects is approximated by the curve $|\delta_3| = |\delta_4|$.

Figure 5.8 c)-d) displays the EDI for nearest- and next-nearest-neighbor QDO pairs near the center of the square and triangular lattices. In contrast to the honeycomb lattice looked at in Fig. 5.7, the square and triangular lattices exhibit a transition from monogamous to promiscuous entanglement sharing as ρ decreases and the interaction strength increases. The deviation between the ρ value with average nearest neighbor EDI value equal to 1 and the ρ value at which the MB potential vanishes is 2.98% for the triangular lattice and 9.01% for the square lattice, relative to the ρ value where $\delta_{\mathrm{MB}} = 0$. This suggests that the boundary between monogamous and promiscuous regions provides a good approximation for the ρ value at which the pairwise additive approximation holds on 2D lattices.

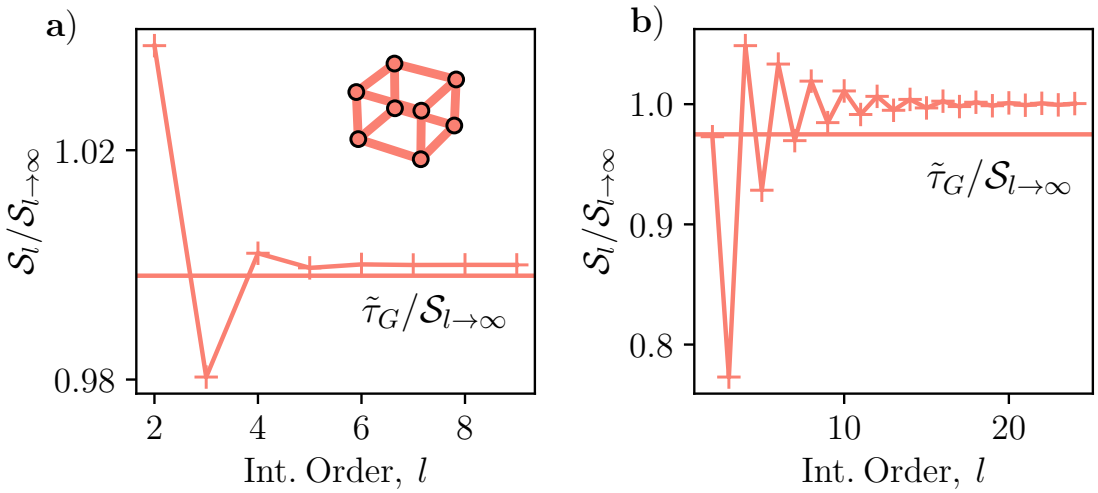

Figure 5.10: In **a) – b)**, where $\rho = 3.4$ and $\rho = 2.2$ respectively, the markers show S_l, where $S_l = \sum_{k=1}^{l}(k-1)\delta_k$, normalized by $S_{l\to\infty} = \sum_{k=1}^{\infty}(k-1)\delta_k$, for the $N = 19\times19\times19$ cubic lattice. The horizontal line shows the normalized value of the reduced tangle, $\tilde{\tau}_G/\mathcal{S}_{l\to\infty}$.

5.4.6 3D crystal lattices

In Fig. 5.9, we extend the analysis of MB effects and entanglement to the 3D cubic and pyrochlore lattices. For weak couplings, the MB potential is initially repulsive, becoming attractive for decreasing ρ and thus increasing coupling strength, as was also the case for the square and triangular lattices.

Having shown the tightness of the bound in Eq. (5.19) for different geometries in the trimer (see Fig. 5.4) and for the linear and zigzag chains (Fig. 5.6), we now demonstrate its tightness for different coupling strengths in the cubic lattice. See Fig. B.6 in Appendix B.6 for evidence of the tightness of the bound on all lattices shown in Fig. 5.8.

We consider the same lattices and setups (i.e., open boundary conditions and numbers of QDOs) as in Fig. 5.8. In Fig. 5.10 we show that, for the cubic lattice at $\rho = 3.4$, one finds $\delta_2 > \tilde{\tau}_G$ but $\delta_2 + 2\delta_3 < \tilde{\tau}_G$. This is the same behavior observed in the zigzag chain and the triangular trimer at the same value of ρ. For stronger couplings in the cubic lattice, in Fig. 5.10 b), we observe the slow convergence of $\mathcal{S}_l$ to $\mathcal{S}_{l\to\infty}$, where $\delta_2 + 2\delta_3 + 3\delta_4 + 4\delta_5 + 5\delta_6 + 6\delta_7 < \tilde{\tau}_G$.

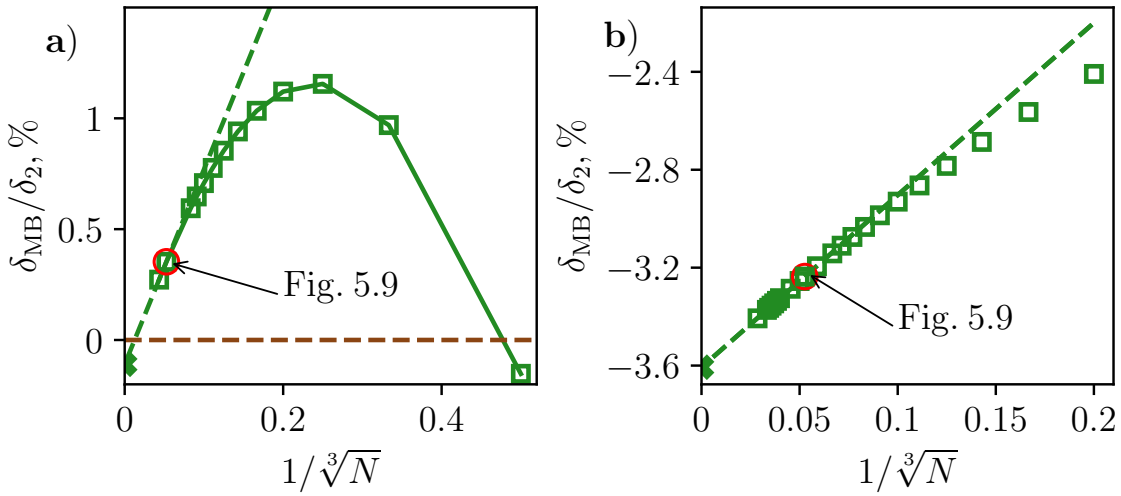

Figure 5.11: Finite size scaling of the MB effects in the cubic lattice, for $\rho = 2.0$ in **a)** and $\rho = 2.6$ in **b)**. Solid dashed green lines extrapolate to $N \to \infty$, with linear fits to the last two data points in **a)** and the last 10 data points in **b)**.

5.4.7 Finite size effects

We have here considered the entanglement distribution and MB effects on *finite* lattices. We assume that the lattice sizes considered in Fig. 5.8 are sufficient for approximating the limit $N \to \infty$, for the 2D honeycomb, square and triangular lattices. Here we consider the finite size effects in the 3D cubic crystal, where in Fig. 5.11, we show finite size effects in the MB potential in the 3D cubic lattice, for two different ρ values. In Fig. 5.11 a), we go up to $N = 23^3$, where $\rho = 2.6$. Note that for $N = 19^3$, the MB effects are attractive, for this value of ρ. In Fig. 5.11 b), we go up to $N = 35^3$, where here $\rho = 2.0$. This value of ρ has a repulsive MB potential for $N = 19^3$.

Interestingly, at small N, a sign change occurs in δ_{MB}, as a function of increasing number of QDOs. The linear extrapolation to the limit $N \to \infty$ in Fig. 5.11 a), predicts another sign change, from positive to negative MB potential. In both a) and b) our linear extrapolation, predicts $\sim -0.4\%$ deviation of the MB effects compared with Fig. 5.8, a not insignificant amount, considering the homogeneous and regular nature of the lattice.

5.5 Conclusion

Here we have looked at dipolar bound systems, with the QDO model. We show that the MB dispersive interaction energy is controlled, via an inequality, by an

entanglement monotone defined in terms of a monogamous entanglement measure for Gaussian states.

We characterize the MB energetics through the monogamous or promiscuous behavior of entanglement distributions. Across a physically motivated parameter range, this classification accurately predicts the sign of many-body effects in the trimer, chains and extended lattices. Our findings go beyond the AT approximation, showing how AT predicts the wrong sign for the MB potential in the trimer. This may explain the failure of the AT potential to predict the attractive sign of the three-body effect in the para-hydrogen trimer at short range, compared to high level quantum chemistry methods [160, 161, 162, 163].

Chapter 6

Symplectic Optimization

6.1 Introduction

So far in this thesis, we have employed numerical diagonalization techniques to compute both the dispersive interaction energy and the Gaussian ground-state CM. In particular, in Eq. (5.10) and Eq. (2.34), we outlined methods for obtaining Gaussian ground states via diagonalization of the potential or Hamiltonian matrix. Likewise, the ground-state energy in Eq. (2.26) is numerically accessible through diagonalization, and, by extension, so is the many-body dispersive binding energy E.

The computation of Gaussian ground-state properties—such as entanglement—requires evaluating the eigenspectrum of a generally non-sparse matrix. This procedure scales polynomially with the number of modes, i.e. $\mathcal{O}(d^3)$, where d denotes the number of modes in the system.

Although this cubic scaling is far more efficient than the exponential scaling characteristic of diagonalization algorithms in generic many-body Hilbert-space formulations, it nevertheless imposes practical restrictions on the number of QDOs that can be simulated. For instance, in Fig. 5.11, extrapolation to the thermodynamic limit resulted in a sign change in the many-body potential, underscoring the importance of large-scale simulations for accurately capturing many-body effects. See also Ref. [164] for a discussion of the role of large-scale QDO simulations and the limitations of current state-of-the-art methods.

To this end, we investigate novel numerical methods for large scale simulation of quantum dipoles. We look at utilizing the Gaussian state form of the variational principle. In Sec. 6.2, we will show how to reformulate the variational principle for paramterized pure state CMs in terms of the symplectic matrix constraint. Then in Sec. 6.3, we further reformulate the symplectic constraint into an unconstrained form and are thus able to show the efficacy of the symplectic optimization approach for

finding ground-states of dipole interacting QDOs on lattices. Finally in Sec. 6.4, we show how our methods are readily transferable to quantum hardware, showing how our symplectic trace cost function can be partially evaluated with parametrized quantum circuits. To achieve this, we develop a method of encoding arbitrary symplectic orthogonal matrices, into paramterized quantum circuits.

6.2 Symplectic Trace Minimization

6.2.1 Symplectic matrix constraint

In lemma. 2.3.2, we showed how the CM of a *pure*, state can be parameterized in terms of symmetric positive definite matrices X and symmetry matrix Y. Here we use lemma. 2.3.2 to prove the following;

$$\gamma_p(2d \times 2d, \mathbb{R}) = \mathcal{S}_p(2d, \mathbb{R}) \bigcap S^{++}(2d, \mathbb{R}), \tag{6.1}$$

where $S^{++}(2d, \mathbb{R})$ denotes the set of matrices which are both positive definite and symmetric. Hence Eq. (6.1) states that any $2d \times 2d$ symmetric, positive definite and symplectic matrix is a valid pure state CM, obeying the Schrödinger uncertainty constraint.

Proof-. Any symmetric positive definite symplectic matrix can be written as

$$\mathcal{S}_p(2d, \mathbb{R}) \bigcap S^{++}(2d, \mathbb{R}) = \begin{pmatrix} \mathbb{1} & 0 \\ Y & \mathbb{1} \end{pmatrix} \begin{pmatrix} X & 0 \\ 0 & X^{-1} \end{pmatrix} \begin{pmatrix} \mathbb{1} & Y \\ 0 & \mathbb{1} \end{pmatrix}, \tag{6.2}$$

where X is symmetric positive definite i.e $X > 0$ and $X = X^T$ and Y is symmetric, see [165, 166] for proof. By expanding out the expression in Eq. (6.2) and applying lemma. 2.3.2, we can thus prove that a symmetric positive definite symplectic matrix, represents a valid pure state CM.

The result that a pure state CM is parameterized by a symplectic and symmetric positive definite matrix, can be inferred from the symplectic eigenvalue decomposition. Inserting the condition for the symplectic eigenvalues of a pure CM in Eq. (2.33) (the symplectic eigenvalues of γ_p are all equal to one), into the symplectic eigendecomposition of the CM in Eq. (2.30), implies that the pure state CM can be written as $\gamma_p = S^T S$, with $S \in \mathcal{S}_p(2d, \mathbb{R})$ [61, 167, 63].

As any positive definite matrix can be written as a invertible matrix multiplied by its transpose [158] and as a symplectic matrix is always invertible, with the formulae for the inverse of S given in Eq. (2.24), the parameterization of γ_p in terms of symplectic matrices guarantees that the CM is a positive definite symmetric and

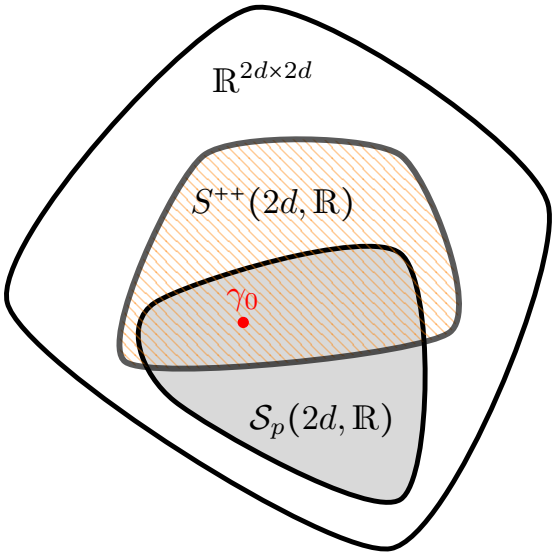

Figure 6.1: The groundstate CM of a general quadractic bosonic Hamiltonian, which minimizes the energy as per Eq. (2.22), lives in the intersection of symmetric positive definite and symplectic matrices i.e $\gamma_0 \in \mathcal{S}p(2d,\mathbb{R}) \bigcap S^{++}(2d,\mathbb{R})$.

symplectic matrix and thus represents a valid CM, obeying the uncertainty principle constraint.

6.2.2 Symplectic trace cost function

The parameterization of the CM in Eq. (6.2) shows that the uncertainty principle constraint on a pure Gaussian state can be guaranteed by writing the CM in terms of a positive definite and symplectic matrix i.e $S^T S$. We can thus reformulate the Gaussian variational principle in Eq. (2.22) as a symplectic optimization problem,

$$\begin{aligned} E_0 &= \inf_{\gamma} \tfrac{1}{4}\mathrm{tr}(\gamma H) \quad \text{s.t.} \quad \gamma + \mathrm{i}\sigma \geq 0, \\ E_0 &= \inf_X \frac{1}{4}\mathrm{tr}(XHX^T) \quad \text{s.t.} \quad X \in \mathcal{S}_p(2d,\mathbb{R}). \end{aligned} \tag{6.3}$$

The Robertson-Schrödinger uncertainty constraint on a valid pure state CM has been encoded as a symplectic constraint on the real $2d \times 2d$ variable matrix X. The statement in Eq. (6.3) is concurrent with lemma 2 in [168], which proved the symplectic eigenvalue problem is equivalent to the symplectic trace minimization problem, studied in Refs [169, 127].

In other words, due to the constraint on the matrix argument in Eq. (6.3), finding the ground-state energy of general bosonic quadratic Hamiltonians can be formulated

as a trace minimization problem over the space of symmetric, positive definite, and symplectic real square matrices of even dimension.

It is worth noting that the equivalence between Eq. (6.3) and Eq. (2.22) implies that the symplectic matrix which diagonalizes the positive definite CM in Eq. (2.30) is the same symplectic matrix that diagonalizes H in Eq. (2.25).

6.3 Unconstrained Symplectic Trace Minimization

6.3.1 Unit triangular factorization

The elementary decomposition utilized here, are the so-called unit triangular matrices,

$$\mathcal{L}_1 = \begin{pmatrix} \mathbb{1} & M_1 \\ 0 & \mathbb{1} \end{pmatrix}, \mathcal{L}_1^T = \begin{pmatrix} \mathbb{1} & 0 \\ M_1 & \mathbb{1} \end{pmatrix}, M_1 \in \mathbb{R}^{d\times d} \quad \text{and} \quad M_1^T = M_1. \tag{6.4}$$

Note that unit triangular matrices are symplectic matrices, which can be trivially shown via the definition of a symplectic matrix in Eq. (2.23). A product of alternating unit triangular matrices is given as

$$\mathcal{L}_\nu = \begin{pmatrix} \mathbb{1} & M_\nu \\ 0 & \mathbb{1} \end{pmatrix} \begin{pmatrix} \mathbb{1} & 0 \\ M_{\nu-1} & \mathbb{1} \end{pmatrix} \cdots \begin{pmatrix} \mathbb{1} & 0 \\ M_2 & \mathbb{1} \end{pmatrix} \begin{pmatrix} \mathbb{1} & M_1 \\ 0 & \mathbb{1} \end{pmatrix}, \quad M_i \in \mathbb{R}^{d\times d}\, M_i^T = M_i. \tag{6.5}$$

Any symmetric matrix M can be freely paramterized as $A + A^T$, where $A \in \mathbb{R}^{d\times d}$.

Proofs in [170] show that $\mathcal{L}_9 = \mathcal{S}_p(2d, \mathbb{R})$ and $\mathcal{L}_5^2 = \mathcal{S}_p(2d, \mathbb{R}) \bigcap S^{++}(2d, \mathbb{R})$ where $\mathcal{L}_\nu^2 = \mathcal{L}_\nu^T \mathcal{L}_\nu$. See appendix C.2 for a partial reproduction of the relevant proofs. A generic symplectic matrix can be parameterized by 9 unit triangular matrices and a positive definite symplectic matrix required 5 unit triangular matrices. In Ref. [171], these numbers were reduced to 5 and 3 respectively, showing that $\mathcal{L}_5 = \mathcal{S}_p(2d, \mathbb{R})$ and $\mathcal{L}_3 \mathcal{L}_3^T = \mathcal{S}_p(2d, \mathbb{R}) \bigcap S^{++}(2d, \mathbb{R})$. As a result, we use 3 parameterized unit triangular matrices in our symplectic trace cost function. Using this decomposition of positive definite symplectic matrices, we rewrite Eq. (6.3) as

$$E_0 = \min_{M_1, M_2, M_3 \in \mathbb{R}^{d\times d}} \mathcal{C}(M_1, M_2, M_3) = \frac{1}{4} \mathrm{tr}(\mathcal{L}_3^T H \mathcal{L}_3), \tag{6.6}$$

$$\mathcal{L}_3 = \begin{pmatrix} \mathbb{1} & M_1 \\ 0 & \mathbb{1} \end{pmatrix} \begin{pmatrix} \mathbb{1} & 0 \\ M_2 & \mathbb{1} \end{pmatrix} \begin{pmatrix} \mathbb{1} & M_3 \\ 0 & \mathbb{1} \end{pmatrix} \quad \text{and} \quad \mathcal{L}_3^T = \begin{pmatrix} \mathbb{1} & 0 \\ M_3 & \mathbb{1} \end{pmatrix} \begin{pmatrix} \mathbb{1} & M_2 \\ 0 & \mathbb{1} \end{pmatrix} \begin{pmatrix} \mathbb{1} & 0 \\ M_1 & \mathbb{1} \end{pmatrix}. \tag{6.7}$$

The symmetry constraint on M_p with $p \in \{1,2,3\}$ is trivial to enforce,

$$M_p = \begin{pmatrix} 0.5(M_p)_{11} & (M_p)_{12} & (M_p)_{13} & \cdots & (M_p)_{1d} \\ 0 & 0.5(M_p)_{22} & (M_p)_{23} & \cdots & (M_p)_{2d} \\ 0 & 0 & 0.5(M_p)_{33} & \cdots & (M_p)_{3d} \\ \vdots & \vdots & \vdots & \ddots & \vdots \\ 0 & 0 & 0 & \cdots & 0.5(M_p)_{dd} \end{pmatrix} + \begin{pmatrix} 0.5(M_p)_{11} & (M_p)_{12} & (M_p)_{13} & \cdots & (M_p)_{1d} \\ 0 & 0.5(M_p)_{22} & (M_p)_{23} & \cdots & (M_p)_{2d} \\ 0 & 0 & 0.5(M_p)_{33} & \cdots & (M_p)_{3d} \\ \vdots & \vdots & \vdots & \ddots & \vdots \\ 0 & 0 & 0 & \cdots & 0.5(M_p)_{dd} \end{pmatrix}^T .$$

Parameterization of the $d \times d$ matrices M_1, M_2, M_3 each require $d(d+1)/2$ parameters, due to the symmetry of the matrices. In total therefore the matrix $\mathcal{L}_3$ and thus the paramerization of the CM requires $3d(d+1)/2$ parameters. In general, the convariance of an d mode pure Gaussian state is characterized by $d^2 + d$ independent parameters [63]. This implies that the $\mathcal{L}_3\mathcal{L}_3^T$ factorization of pure Gaussian states is overparamterization and hence the possibility of further more efficient representations.

6.3.1.1 Computing Gradients

Next we show how to compute the gradients of the cost function in Eq. (6.6), i.e $\mathrm{tr}(\mathcal{L}_3^T H \mathcal{L}_3)$ with respect to the variational matrix elements $(M_p)_{kl}$ with $p \in \{1,2,3\}$. This allows for efficient computation of the Jacobian vector $\boldsymbol{J}^T$, given by

$$\boldsymbol{J}^T = \left[\underbrace{\frac{\partial \mathcal{C}}{\partial (M_1)_{1,1}}, .., \frac{\partial \mathcal{C}}{\partial (M_1)_{d,d}}}_{d(d+1)/2}, \underbrace{\frac{\partial \mathcal{C}}{\partial (M_2)_{1,1}}, .., \frac{\partial \mathcal{C}}{\partial (M_2)_{d,d}}}_{d(d+1)/2}, \underbrace{\frac{\partial \mathcal{C}}{\partial (M_3)_{1,1}}, .., \frac{\partial \mathcal{C}}{\partial (M_3)_{d,d}}}_{d(d+1)/2} \right], \quad (6.8)$$

where we write $\frac{1}{4}\mathrm{tr}(\mathcal{L}_3^T H \mathcal{L}_3) = \mathcal{C}(M_1, M_2, M_3) = \mathcal{C}$ for convenience. The cost function of Eq. (6.3) can be written by employing a block matrix decomposition with basis matrices $E_1 = \begin{bmatrix} \mathbb{1}_d \\ 0 \end{bmatrix}$ and $E_2 = \begin{bmatrix} 0 \\ \mathbb{1}_d \end{bmatrix}$. The gradient of Eq. (6.6) with respect to $\mathcal{L}_3$ is [172],

$$\frac{\partial \mathrm{tr}(\frac{1}{4}\mathcal{L}_3^T H \mathcal{L}_3)}{\partial \mathcal{L}_3} = \frac{1}{2}\mathcal{L}_3 H. \quad (6.9)$$

The matrix $\mathcal{L}_3$ can be written, using the matrices (E_1, E_2). Using the following identity [172],

$$\frac{\partial \mathrm{tr}(\mathcal{L}_3^T H \mathcal{L}_3)}{\partial (\mathcal{L}_3)_{kl}} = \mathrm{tr}\left(\left[\frac{\partial \mathrm{tr}(\mathcal{L}_3^T H \mathcal{L}_3)}{\partial \mathcal{L}_3} \right]^T \frac{\partial \mathcal{L}_3}{\partial (\mathcal{L}_3)_{kl}} \right), \quad (6.10)$$

the expression in Eq. (6.9) and the cyclic property of the trace operator, we thus find the following analytic expressions for the gradient of Eq. (6.6) with respect to M_1, M_2 and M_3,

$$\frac{\partial \mathrm{tr}(\frac{1}{4}\mathcal{L}_3^T H \mathcal{L}_3)}{\partial(M_1)} = E_1^T \mathcal{L}_3 H E_2 (M_2 M_3)^T + E_1^T \mathcal{L}_3 H E_2 + E_1^T \mathcal{L}_3 H E_1 M_2^T, \tag{6.11}$$

$$\frac{\partial \mathrm{tr}(\frac{1}{4}\mathcal{L}_3^T H \mathcal{L}_3)}{\partial(M_2)} = M_1^T E_1^T \mathcal{L}_3 H E_2 M_3^T + M_1^T E_1^T \mathcal{L}_3 H E_1 + E_2^T \mathcal{L}_3 H E_2 M_3^T + E_2^T \mathcal{L}_3 H E_1, \tag{6.12}$$

and

$$\frac{\partial \mathrm{tr}(\frac{1}{4}\mathcal{L}_3^T H \mathcal{L}_3)}{\partial(M_3)} = (M_1 M_2)^T E_1^T \mathcal{L}_3 H E_2 + E_1^T \mathcal{L}_3 H E_2 + M_2^T E_1^T \mathcal{L}_3 H E_2. \tag{6.13}$$

The matrix elements of these expressions are used to provide the elements of $\boldsymbol{J}^T$ in Eq. (6.8).

6.3.2 Numerical examples

Using the unconstrained cost function in Eq. (6.6) and analytic expressions for the associated gradients of the $\frac{3}{2}d(d+1)$ parameters we proceed to demonstrate the algorithm. We focus on the QDO Hamiltonian in Eq. (5.2), although we stress the approach is valid for any general quadractic bosonic Hamiltonian of the form in Eq. (2.11). We use a Python script, using Numpy and Scipy libraries to numerically solve Eq. (6.6). We use the conjugate gradient (CG) algorithm in-build in Scipy [173]. The CG algorithm in Scipy uses the Fletcher-Reeves method [174, 175]. As we have an analytic expression for the Jacobian, derived in the previous section, we need not resort to expensive finite difference methods for approximating the gradients. The tolerance of the CG descent algorithm is set to $\mathrm{tol} = 1 \times 10^{-7}$.

Here we consider the QDO Hamiltonian in Eq. (5.2), on the square and cubic lattice, hence here $d = 3N$. The relative error, per optimization step, is defined as

$$\epsilon_E = \frac{|\mathcal{C} - E|}{E}, \tag{6.14}$$

where E is the MB inclusive lattice bond energy as per Eq. (5.4). Recall this is computed via diagonalizing the matrix V. The cost function $\mathcal{C} = \mathcal{C}(M_1, M_2, M_3)$ is the value of Eq. (6.6), computed at step s. A step is defined as a call to the cost function. We warm start the CG algorithm, with initial input matrices $M_1 = \mathbb{1}, M_2 = \mathbb{1}$ and $M_3 = \mathcal{T}$, with $\mathcal{T}$ defined in Eq. (5.1).

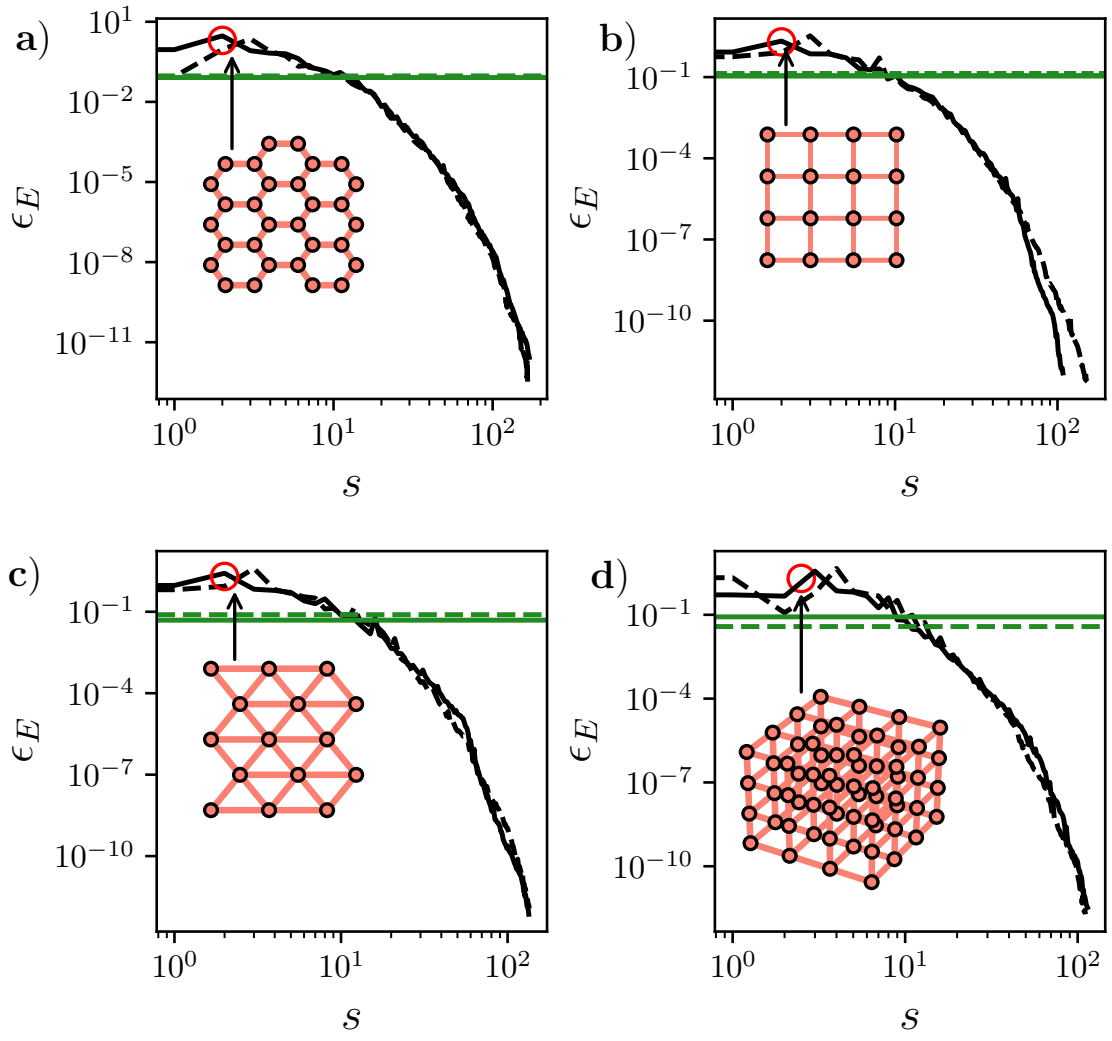

Figure 6.2: Evolution of the symplectic trace cost function on lattices. **a)** shows the honeycomb lattice with $N = 2 \times 3 \times 3$ (solid line) and $N = 6 \times 6 \times 2$ (dashed line). **b)** square lattice with $N = 4 \times 4$ (solid) and $N = 10 \times 10$ (dashed). **c)** triangular lattice with $N = 4 \times 4$ (solid) and $N = 10 \times 10$ (dashed). Finally **d)** shows the cubic lattice with $N = 4 \times 4 \times 4$ (solid) and $N = 10 \times 10 \times 10$ (dashed). In **a)**, **c)** and **d)** we set $\rho = 1.9$ and in **b)** $\rho = 1.8$. We see the convergence to the true ground-state interaction energy for all the lattice types and sizes. The horizontal green lines show $|\delta_{\mathrm{MB}}|/E$. For all the considered lattice sizes and ρ values, $|\delta_{\mathrm{MB}}|/E \sim 10\%$. Hence the algorithm is able to find ground-state lattice energies of systems containing non trivial MB interactions.

In Fig. 6.2, we demonstrate the capability of the algorithm to find accurate MB inclusive dispersive interaction energies on different lattices. The horizontal green lines shows the absolute value of the error inherent in the pair-potential compared with the MB solution. Fig. 6.2 therefore shows the efficacy of the symplectic optimization algorithm at retrieving the accurate MB lattice energies, requiring approximately 100 steps, for all the considered lattices.

The largest number of QDOs we consider with the algorithm is for the cubic lattice in Fig. 6.2 *d*). Convergence on the 4^3 cubic lattice required 115 steps and convergence on the larger 10^3 cubic lattice required 112 steps. This suggests the number of steps required for convergence of the algorithm is independent of the lattice size. Weaker ρ values however, required a greater number of steps for converge e.g at $\rho = 3$ on the 4^3 cubic lattice 336 steps were required for termination of the CG algorithm.

In addition to the groundstate energy, solving Eq. (6.6), allows for access to the groundstate CM. Given that,

$$M_1^\star, M_2^\star, M_3^\star = \text{argmin}_{M_1,M_2,M_3}\mathcal{C}(M_1, M_2, M_3) \tag{6.15}$$

with $\mathcal{C}(M_1, M_2, M_3)$, given in Eq. (6.6), the groundstate CM γ_0 is therefore approximated as

$$\gamma_0^\star = (\mathcal{L}^\star)_3^T \mathcal{L}_3^\star. \tag{6.16}$$

$$\mathcal{L}_3^\star = \begin{pmatrix} \mathbb{1} & M_1^\star \\ 0 & \mathbb{1} \end{pmatrix}\begin{pmatrix} \mathbb{1} & 0 \\ M_2^\star & \mathbb{1} \end{pmatrix}\begin{pmatrix} \mathbb{1} & M_3^\star \\ 0 & \mathbb{1} \end{pmatrix} \quad \text{and} \quad (\mathcal{L}^\star)_3^T = \begin{pmatrix} \mathbb{1} & 0 \\ M_3^\star & \mathbb{1} \end{pmatrix}\begin{pmatrix} \mathbb{1} & M_2^\star \\ 0 & \mathbb{1} \end{pmatrix}\begin{pmatrix} \mathbb{1} & 0 \\ M_1^\star & \mathbb{1} \end{pmatrix}. \tag{6.17}$$

In Fig. 6.3, we show the element wise deviation between the target CM elements and the reconstructed CM, learned from symplectic optimization, after the convergence of the CG algorithm. In Appendix C.3, we use Eq. (6.16) to show how the symplectic optimization converges to accurate values for the entanglement in the $1D$ discretization of the Klein-Gordon Hamiltonian, previously looked at in example 3.3.2 in Sec. 3.32.

6.4 Quantum Symplectic Optimization

Having shown the ability of symplectic optimization to accurately find Gaussian groundstates, we here extend the method to develop a variant of the algorithm, which can run on a quantum computer. Such an approach falls under the umbrella of variational quantum algorithms (VQAs). In a generic VQA the cost function is prepared

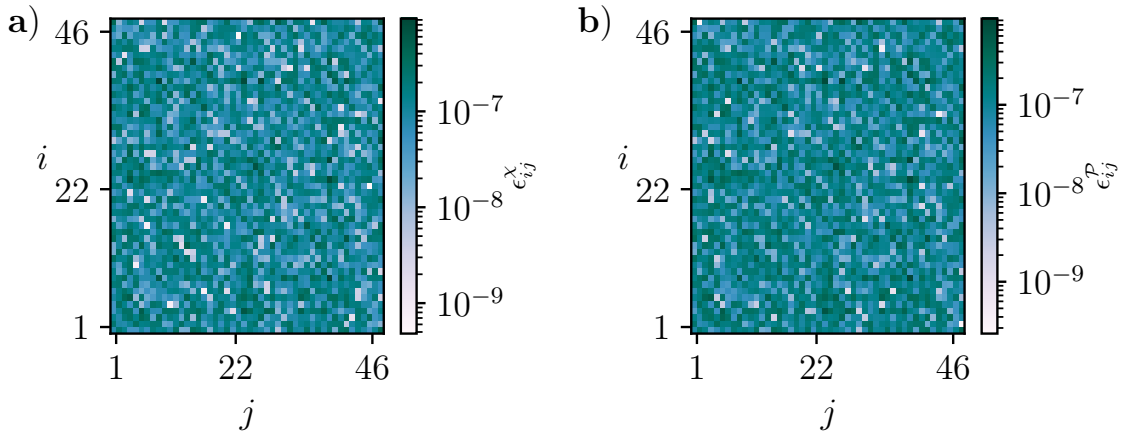

Figure 6.3: Comparison between target CM computed via ED (see Eq. (5.10)) and the CM $\gamma_0^\star$ computed by the algorithm i.e Eq. (6.16), shown for position block in **a)** where $\epsilon^{\chi}_{ij} = (|E_1^T \gamma_0^\star E_1 - V^{-1/2}|)_{ij}$ and the momentum block in **b)**, $\epsilon^{\mathcal{P}}_{ij} = (|E_2^T \gamma_0^\star E_2 - V^{1/2}|)_{ij}$. Both **a)** – **b)** are shown for $\rho = 1.8$, in the $N = 4 \times 4$ square lattice.

and evaluated on a quantum computer, the result of which is fed to a classical computer. The classical computer is tasked with optimizing the variational parameters. The VQA procedure thus consists of an iteratively applied quantum-classical feedback loop.

Here, we show how the symplectic trace cost function in Eq. (6.3) can be decomposed into a linear combination of trace functions of unitaries. Each trace term is weighted by a variational parameter, and thus our approach amounts to evaluating a hybrid quantum-classical cost function. Specifically, the cost function is partially off-loaded to the quantum computer and partially evaluated classically. See Refs. [176, 177, 178] for VQAs with similar trace-based cost functions.

For an n-qubit circuit, the problem of trace estimation, up to inverse polynomial precision, for $2^{\mathrm{poly}(n)} \times 2^{\mathrm{poly}(n)}$ unitary matrices that can be constructed by $\mathrm{poly}(n)$-sized quantum circuits, is DQC1-complete [179, 180]. Therefore, under certain complexity-theoretic assumptions, estimating the trace of exponentially large unitary matrices is efficient on a quantum computer but inefficient for any classical algorithm.

Representing the $2d \times 2d$ matrices in Eq. (6.3) scales logarithmically with the number of qubits n, and is thus efficient in terms of quantum resources, assuming the required circuit depth is also polynomial in n. Specifically, this assumes the existence of $\mathcal{O}(\mathrm{poly}(n))$-depth circuits for representing the symplectic orthogonal component of γ_p.

6.4.1 Bloch-Messiah decomposition

Here we will look at a method for quantum circuit parameterization of pure Gaussian state CMs. Our parameterization is based on the Bloch-Messiah decomposition (see appendix C.1) and the fact that pure state CMs are positive definite. We can use the Bloch-messiah decomposition to decompose any arbitrary pure state CM as [63],

$$\gamma_p = O_s \tilde{D} O_s^T, \quad \text{where} \quad O_s \in \mathcal{S}p(2d, \mathbb{R}) \bigcap SO(2d, \mathbb{R}), \tag{6.18}$$

and $\tilde{D} = D \oplus D^{-1} = \text{diag}(d_1, d_2, .., d_d, 1/d_1, 1/d_2, .., 1/d_d)$ with $d_i > 0$. The Bloch-Messiah decomposition, allows one to write any pure state CM in terms of a symplectic orthagonal matrix O_s and the diagonal matrix $\tilde{D}$. Using this decomposition, γ_p can be represented as a quantum circuit. We show how an arbitrary symplectic orthagonal matrix can be written as a parameterized quantum circuit, due to an isometry between the set of symplectic orthogonal matrices and the set of unitary matrices. This allows us to write an arbitrary pure Gaussian state CM as a linear combination of unitary matrices.

A general $2d \times 2d$ orthogonal symplectic matrix can always be written as [63],

$$O_s = \begin{pmatrix} X & Y \\ -Y & X \end{pmatrix}, \quad \text{where} \quad XY^T - YX^T = 0 \quad \text{and} \quad XX^T + YY^T = \mathbb{1}. \tag{6.19}$$

Orthogonal symplectic matrices can be written directly in terms of $d \times d$ unitary matrix U [181],

$$O_s = \begin{pmatrix} X & Y \\ -Y & X \end{pmatrix} = \frac{1}{2} \begin{pmatrix} U^\star + U & i(U^\star - U) \\ i(U - U^\star) & U^\star + U \end{pmatrix}. \tag{6.20}$$

The above can equivalently be written as

$$O_s = \begin{pmatrix} X & Y \\ -Y & X \end{pmatrix} = \bar{U}^\dagger \begin{pmatrix} U^\star & 0 \\ 0 & U \end{pmatrix} \bar{U}, \quad \text{where} \quad \bar{U} = \frac{1}{\sqrt{2}} \begin{pmatrix} \mathbb{1}_d & i\mathbb{1}_d \\ \mathbb{1}_d & -i\mathbb{1}_d \end{pmatrix}. \tag{6.21}$$

Thus applying Eq. (6.21) to Eq. (6.18), we can write the CM as

$$\gamma_p = \underbrace{\bar{U}^\dagger \begin{pmatrix} U^\star & 0 \\ 0 & U \end{pmatrix} \bar{U}}_{O_s} \tilde{D} \underbrace{\bar{U}^T \begin{pmatrix} U^\dagger & 0 \\ 0 & U^T \end{pmatrix} \bar{U}^\star}_{O_s^T}, \tag{6.22}$$

where we have used the fact that $(A_1 A_2 .. A_{k-1} A_k)^T = A_k^T A_{k-1}^T ... A_2^T A_1^T$ for $A \in \mathbb{C}^{d \times d}$. From this decomposition we are able to write the CM of an arbitrary pure Gaussian state in terms of d real positive parameters $\boldsymbol{d} = (d_1, ..., d_d)$ and a $d \times d$ unitary matrix, U, where the diagonal matrix in Eq. (6.18), is parametrized in terms of $\boldsymbol{d}$ as $\tilde{D} = \text{diag}(\boldsymbol{d}, \boldsymbol{d}^{-1})$.

6.4.2 VQA for solving Eq. (2.22)

The $d \times d$ unitary matrix U can be parameterized by a quantum circuit $U(\boldsymbol{\theta})$ where $\boldsymbol{\theta}$ is a set of trainable parameters e.g $\boldsymbol{\theta} = (\theta_1, \theta_2, ...)$. The parameterized quantum circuit or variational ansatz $U(\boldsymbol{\theta})$ is given as

$$U(\boldsymbol{\theta}) = U_1((\boldsymbol{\theta})_1)U_2((\boldsymbol{\theta})_2)...U_{L-1}((\boldsymbol{\theta})_{L-1})U_L((\boldsymbol{\theta})_L), \tag{6.23}$$

The integer L specifies the *depth* of the quantum circuit. Hence $U(\boldsymbol{\theta})$ can be generically written as the product of L layers of sequentially applied unitaries. The ansatz has a repeating structure, with variational parameters, given by the elements of the vector $\boldsymbol{\theta}$, typically fed into single or two qubit rotation gates.

The implement of the block matrix unitaries $U(\boldsymbol{\theta}) \oplus U^\star(\boldsymbol{\theta})$ and $U^\dagger(\boldsymbol{\theta}) \oplus U^T(\boldsymbol{\theta})$, in circuit form is shown in appendix C.5 in Fig. C.3. The circuits for $U(\boldsymbol{\theta}) \oplus U^\star(\boldsymbol{\theta})$ and $U^\dagger(\boldsymbol{\theta}) \oplus U^T(\boldsymbol{\theta})$ each require an additional ancilla qubit and thus $n+1$ qubits, in total, to be expected as the dimension of γ_p is $2d \times 2d$.

In order to apply the matrix γ_p as a series of quantum circuits, we must further be able to implement the $2d \times 2d$ matrices, $\bar{U}, \bar{U}^\dagger, \bar{U}^T$ and $\bar{U}^\star$. This is possible as these matrices are unitary and can thus be represented as circuits with $n+1$ qubits. We rewrite $\bar{U}$ in Eq. (6.22) as

$$\bar{U} = \frac{1}{\sqrt{2}} \begin{pmatrix} 1 & i1 \\ 1 & -i1 \end{pmatrix} \otimes \mathbb{1}_{2^n = d}, \tag{6.24}$$

where the single qubit matrix $\frac{1}{\sqrt{2}} \begin{pmatrix} 1 & i1 \\ 1 & -i1 \end{pmatrix}$ can be decomposed into a product of elementary quantum gates.

Having shown how to represent a symplectic orthogonal matrix, as given in Eq. (6.21), in terms of a block encoded parameterized quantum circuit, $O_s = \bar{U}^\dagger U(\boldsymbol{\theta}) \oplus U^\star(\boldsymbol{\theta})\bar{U}$, we can express Eq. (2.22), as a hybrid quantum-classical cost function,

$$\mathcal{C}(\boldsymbol{\theta}, \boldsymbol{d}) = \frac{1}{4}\mathrm{tr}\left(\bar{U}^\dagger \underbrace{\begin{pmatrix} U^\star(\boldsymbol{\theta}) & 0 \\ 0 & U(\boldsymbol{\theta}) \end{pmatrix}}_{\text{quantum parameters}} \bar{U} \underbrace{\mathrm{diag}(\boldsymbol{d}, \boldsymbol{d}^{-1})}_{\text{classical parameters}} \bar{U}^T \underbrace{\begin{pmatrix} U(\boldsymbol{\theta})^\dagger & 0 \\ 0 & \bar{U}(\boldsymbol{\theta})^T \end{pmatrix}}_{\text{quantum parameters}} \bar{U}^\star H \right). \tag{6.25}$$

The hermitian matrices $2d \times 2d$ diagonal matrix $\tilde{D}$ and the hermitian $2d \times 2d$ matrix H, can be decomposed into a weighted sum of unitaries, via the Pauli decomposition. In appendix C.6, we show that the number of qubits required to measure the quantum part of the cost function in Eq. (6.25) grows logarithmically with d. Whilst we leave

the implementation and scaling analysis of the VQA for future work, we give a proof of principle demonstration of the algorithm in appendix. C.7, solving Eq. (3.30), with $d = 4$.

6.5 Conclusion

In this chapter, we have developed an algorithm to find the ground-state of a general quadratic bosonic Hamiltonian. Our approach exploits the matrix structure of the parameterized quantum CM. We showed how the variational principle for Gaussian states can be recast as a constraint matrix optimization problem. We showed how the matrix constraint can be dealt with efficiently, by mapping to a unconstrained version of the problem, ideally suited for optimization. We demonstrated the efficacy of our approach by solving the QDO Hamiltonian on a 2D square and 3D cubic lattice, for up to 10^3 QDOs and thus millions of variational parameters. Finally we show how to partially evaluate the cost function on a quantum computer, via a block circuit encoding of symplectic orthogonal matrices.

Chapter 7

Conclusion

7.1 Summary of work

In this thesis we have focusing on applying Gaussian state quantum information concepts and methods to study noncovalent dipolar bound systems, with the QDO model.

In Chapter 2 and Chapter 3, we introduced much of the theory of Gaussian entanglement, with a focus on the monogamy of entanglement. The original results of the thesis are presented from Chapter 4 on-wards.

In Chapter 4, we investigated the interplay between promiscuous entanglement sharing, arising from the high-dimensional Hilbert space of Gaussian states, and restricted monogamous behavior, imposed by entanglement monogamy constraints. Our findings showed that the entanglement behavior became increasingly promiscuous with stronger coupling. We then provided an example in which promiscuous behavior is prohibited, namely in the limit of an infinitely all-to-all connected system of oscillators, and analyzed the resulting decay of pairwise and multipartite entanglement.

In Chapter 5, we applied Gaussian state theory to the QDO model, demonstrating how the ground state energy of the QDO Hamiltonian can be re-derived via symplectic diagonalization, and how ground-state quantum correlations are efficiently accessible through the covariance matrix (CM). The central result of this chapter was the establishment of the role of distributed entanglement in the QDO model, showing analytically how entanglement governs both the pairwise and infinite-order many-body (MB) dispersive binding energies, compactly described by the bound in Eq. (5.19). We further demonstrated numerically the tightness of this entanglement constraint in different QDO systems and geometries, including large-scale lattices.

In addition, we applied the monogamy/promiscuity classification developed in Chapter 4 to analyze the repulsive or attractive character of MB potentials, first in a trimer system and subsequently in a quasi-one-dimensional chain. In both cases, we accurately predicted whether the MB effects are attractive or repulsive within a physically motivated parameter range, based solely on whether the entanglement distribution is promiscuous or monogamous. Furthermore, we showed that the properties of the trimer provide direct insight into the character of MB effects in two- and three-dimensional lattices. Our results therefore establish a fundamental entanglement-based framework for understanding MB potentials and the limitations of the Axilrod–Teller (AT) three-body correction.

In Chapter 6, we introduced novel methods for finding ground states of quadratic bosonic Hamiltonians, and thus of the QDO Hamiltonian. Specifically, we develop a symplectic optimization framework based on encoding the uncertainty principle constraint into the CM in matrix form. We benchmarked this symplectic optimization scheme for retrieving the Gaussian ground state of dipole-bound lattices, and further demonstrated how the algorithm can be adapted into a variational quantum algorithm (VQA).

7.2 Outlook

Whilst we have shown the efficacy of the symplectic optimization approach for the QDO problem, the algorithm does not offer any immediate advantage over diagonalizing the potential matrix. Evaluating the cost function for an arbitrary N QDO system requires multiplying $6N \times 6N$ dimensional matrices [1], where matrix multiplication scales as $\mathcal{O}(N^3)$, which is also the scaling of diagonalizing the $3N \times 3N$ potential matrix, V.

Moreover in its present form the algorithm does not offer any practical speedups and indeed is more costly in terms of runtime compared with diagonalization, for the systems sizes we have considered in this thesis. Although the latter point could be rectified by trying out other optimizers [182], stochastic modifications [183] or writing the code in a more efficient low-level manner, readily amendable, due to the simplicity of evaluating the cost function and the Jacobian.

Whilst in this thesis we have focused on the dipole-dipole interacting QDOs, including higher order multipoles in QDO simulations in a topic of current research

[1] This is trivially reduced to $3N \times 3N$ dimensional matrices by multiplying out the terms in Eq. (6.6) at the expensive of a larger but constant number of trace terms in the cost function

[184, 185, 186, 187], which could be aided by our methods. In particular, the CM decompositions we utilize, could be used as a basis for approximating non-Gaussian groundstates of perturbative multipole interactions, within the Gaussian state framework, along the lines of techniques in Refs [188, 189, 167, 190, 191]. Our paramterization of pure state CMs may also find use outside intermolecular chemistry, in studies of quantum gravity for instance [192, 136].

We have further left the implementation of the quantum variant of the method for future work. A key challenge here is the scalability of the classical optimization procedure, as this is theoretically NP-hard [193], characterized by vanishing gradients and large numbers of local minima [194, 195, 196, 197]. Complexity theory considerations suggest that a quantum advantage for our cost function may exist. Recent pre-prints [198, 199, 200] develop a parameterized circuit for representing symplectic unitaries, ideally suited for the limited qubit connectivity of near term quantum hardware, as well as random sampling supremacy experiments. [2] Applying this approach to our cost function and methods would significantly reduce gate costs, as well as provide a path toward a possible useful application of NISQ devices.

The central result of this thesis was to establish the relationship between energy and entanglement in dipole bound QDOs, thereby elucidating the connection between the structure of the quantum correlations and the resultant nature of the MB potential. This was analytically substantiated by a bound derived between the reduced tangle, an entanglement monotone we defined based on the monogamous entanglement measure for Gaussian states, and the terms in a perturbative expansion of the interaction energy. This constitutes, to the best of our knowledge, the first analytically rigorous relation between an entanglement measure and the significant contribution to the chemical correlation energy, due to dispersion.

The adiabatic-connection fluctuation–dissipation (ACFD) theorem provides an exact expression for the exchange–correlation energy [151]. Within the random phase approximation (RPA), the infinite series of terms contributing to the dispersive energy in Eq. (5.4) can be rigorously derived from the ACFD theorem [151, 154, 201, 202]. Consequently, both pairwise and many-body dispersion contributions are contained *within* the ACFD correlation energy. Extending our bound to establish a direct connection with the total chemical correlation energy within the RPA would thus represent a first step towards a full mathematical characterization of this highly important quantity in terms of entanglement.

[2] In appendix C.8 we give an example of a variational ansatz, which enforces the symplectic orthogonal constraint based on the approach given in the aforementioned preprint.

Our analytic methods, revolved around the fact that the quantum dipole energy could be written, using the Gaussian state ansatz, in terms of the matrix elements of the CM. Hence whilst we focused on utilizing this fact to connect entanglement and energy, other bounds on the MB energy could be derived. Such an approach would make use of the CM formalism to precisely and mathematically understand the long range extent of dispersive bonds via the algebraic decay of the off-diagonal CM elements [61, 203].

A clearer picture of the relation between the monogamy–promiscuity boundary and the transition between repulsive and attractive many-body effects in the linear–zigzag chain studied in 5.4.4 may be obtained in future work by implementing periodic boundary conditions. This approach would suppress edge-induced discrepancies in the pairwise tangle shared between neighboring QDOs. Furthermore, modifying the dipole–dipole potential through Ewald summation techniques [204] could prove useful in accurately capturing long-range interactions.

Interestingly, a quantum phase transition in a chain of interacting electrons occurs for 1D linear chain going to a zigzag configuration [205, 206, 207] of the type depicted in Fig. 5.5. This type of structural phase transition also occurs in higher dimensions, where the zigzag configuration transitions into a double helix [208]. Our work may thus allow for characterizing different types of structural phases in terms of the underlying entanglement properties and distribution [209].

Importantly while the results here focus on model systems, the same prescription, upon appropriate parameterization of the QDOs, could be applied to realistic materials. This would provide a direct link between their physical and chemical properties and the amount of entanglement shared by their constituents. Concepts from quantum information theory thus provide a novel path for shedding light on important chemical problems [164, 210, 211, 212, 213, 214, 215].

Appendix A

A.1 Mixed State Pairwise Tangle

The pairwise tangle, $\tau_G(i:j)$, quantifying the entanglement shared between modes i and j in a mixed two mode state, is elaborated on here. We define the following quantities, which uniquely capture the two mode entanglement; $a^{ii}, b^{jj}, c_+^{ij}, c_-^{ij}$, with $c_+^{ij} \geq |c_-^{ij}|$. These are required to satisfy the following equalities: $a^{ii} = \sqrt{\langle \hat{\chi}_i^2 \rangle \langle \hat{P}_i^2 \rangle}$, $b^{jj} = \sqrt{\langle \hat{\chi}_j^2 \rangle \langle \hat{P}_j^2 \rangle}$, $c_+^{ij} c_-^{ij} = \langle \hat{\chi}_i \hat{\chi}_j \rangle \langle \hat{P}_i \hat{P}_j \rangle$ and $(a^{ii}b^{jj} - (c_+^{ij})^2)(a^{ii}b^{jj} - (c_-^{ij})^2) = ((\langle \hat{P}_i \hat{P}_j \rangle)^2 - \langle \hat{P}_i^2 \rangle \langle \hat{P}_j^2 \rangle)((\langle \hat{\chi}_i \hat{\chi}_j \rangle)^2 - \langle \hat{\chi}_i^2 \rangle \langle \hat{\chi}_j^2 \rangle)$. In addition the following inequalities must be satisfied: $a^{ii} \geq 1$, $b^{jj} \geq 1$, $a^{ii}b^{jj} - (c_\pm^{ij})^2 \geq 1$ and $(a^{ii}b^{jj} - (c_+^{ij})^2)(a^{ii}b^{jj} - (c_-^{ij})^2) + 1 \geq (a^{ii})^2 + (b^{jj})^2 + 2c_+^{ij}c_-^{ij}$. For notational convenience we will write $a^{ii}, b^{jj}, c_+^{ij}, c_-^{ij}$ as a, b, c_+, c_-, for here onwards. The pairwise tangle is then given by [79],

$$\tau_G(i:j) = f(\min_{0 \leq \phi < 2\pi} m(\phi)), \tag{A.1}$$

where recall the definition of $f(x)$ given underneath Eq. (3.34). Here

$$m(\phi) = h_1^2(\phi)/h_2(\phi), \tag{A.2}$$

$$h_1(\phi) = \xi_- + \sqrt{\eta^*}\cos(\phi), \tag{A.3}$$

$$h_2(\phi) = 2(ab - c_-^2)(a^2 + b^2 + 2c_+c_-) - (\zeta/\sqrt{\eta^*})\cos(\phi) + (a^2 - b^2)\sqrt{1 - \xi_+^2/\eta^*}\sin(\phi) \tag{A.4}$$

$$\xi_\pm = c_+(ab - c_-^2) \pm c_- \tag{A.5}$$

$$\eta^* = [a - b(ab - c_-^2][b - a(ab - c_-^2])] \tag{A.6}$$

and

$$\zeta = 2abc_-^3 + (a^2 + b^2)c_+c_-^2 + [a^2 + b^2 - 2a^2b^2]c_- - ab(a^2 + b^2 - 2)c_+. \tag{A.7}$$

A.2 Properties of $f(x)$

Lemma. 5 .- $f(x+y) \geq f(x) + f(y)$, for $x, y \geq 0$

Proof .- The derivative of $f(x)/x$ with respect to x is

$$\partial_x(f(x)/x) = \frac{(-1+\sqrt{1+x})(-1+\sqrt{x}+\sqrt{1+x})}{x^2\sqrt{1+x}}, \tag{A.8}$$

hence $\partial_x(f(x)/x) \geq 0$ and thus $\partial_x(f(x)/x)$ is an increasing function for $x \geq 0$, i.e

$$\frac{f(x_2)}{x_2} \geq \frac{f(x_1)}{x_1}, \quad \text{given} \quad x_2 \geq x_1 \geq 0. \tag{A.9}$$

Therefore

$$f(cx) \geq cf(x) \quad \text{for} \quad c \geq 1, \tag{A.10}$$

with the converse being true (i.e $f(cx) \leq cf(x)$) for $c \in [0,1]$ and hence $f(x)$ is a star shaped function [216].

Hence setting $c = 1 + \frac{y}{x}$, where $x, y \geq 0$,

$$f(x+y) \geq \frac{(y+x)}{x} f(x) \tag{A.11}$$

likewise,

$$f(x+y) \geq \frac{(y+x)}{y} f(y) \tag{A.12}$$

and thus

$$f(x+y) \geq f(x) + f(y). \tag{A.13}$$

Lemma. 6 .- $f(x) \geq \frac{x}{4}$, for $x \geq 0$.

Proof. Writing out $f(x)$, we have

$$f(x) = \frac{1}{4}\left(\sqrt{x} + \underbrace{\sqrt{x+1}-1}_{\epsilon}\right)^2, \tag{A.14}$$

where $\epsilon = \sqrt{x+1} - 1 \geq 0$, as $x \geq 0$. Expanding out the bracket gives,

$$\frac{1}{4}(x + \epsilon^2 + 2\epsilon\sqrt{x}). \tag{A.15}$$

Given that $\epsilon^2 + 2\epsilon\sqrt{x} \geq 0$,

$$(x + \epsilon^2 + 2\epsilon\sqrt{x}) \geq x, \tag{A.16}$$

which establishes the result.

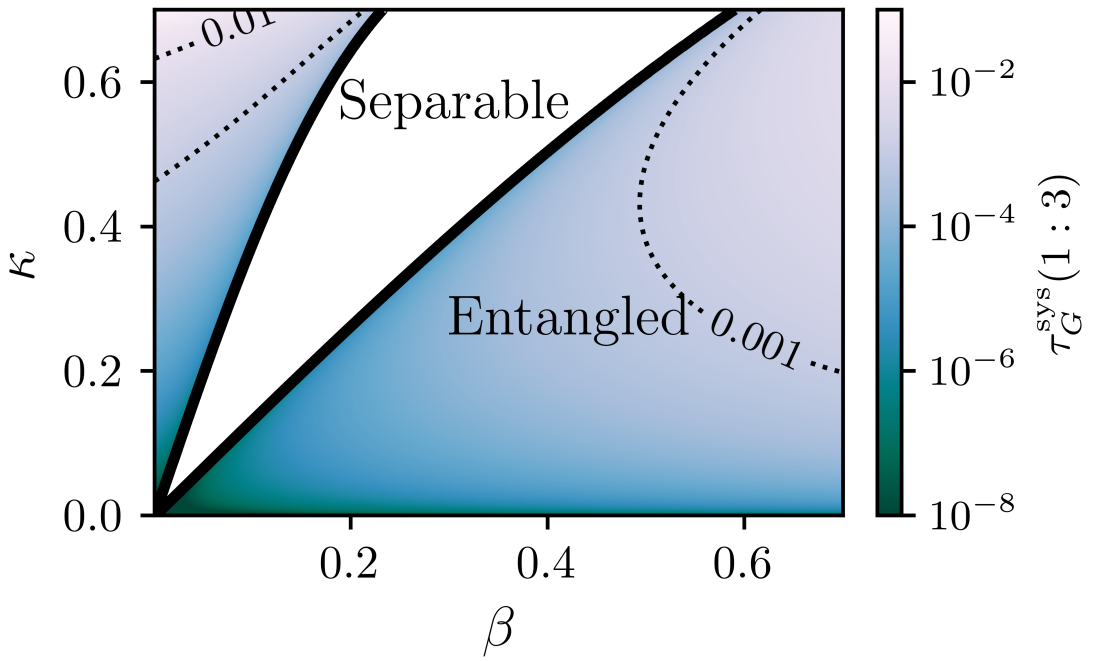

Figure A.1: Heatmap of $\tau_G^{\mathrm{sys}}(i:j)$ plotted on a log-scale for for different values of κ and β, see Eq. (4.8) and Fig. 4.2 for definitions of these parameters. The white region, shows where the PPT criterion ensures modes 1 and 3 share no entanglement.

A.3 von Neumann Entanglement Entropy

The von Neumann entanglement entropy is computable from the symplectic eigenvalues of the CM. The Von Neumann entanglement entropy is computable from the CM as follows [63],

$$S_V(i) = s_v\left(\sqrt{\langle\hat{\chi}_i^2\rangle\langle\hat{P}_i^2\rangle}\right), \tag{A.17}$$

where

$$s_v(x) = \frac{x+1}{2}\log_2\left(\frac{x+1}{2}\right) - \frac{x-1}{2}\log_2\left(\frac{x-1}{2}\right). \tag{A.18}$$

A.4 Entanglement Between Modes 1 and 3 in a Tripartite State

Fig. A.1, shows a heatmap of $\tau_G^{\star}(1:3)$, for the same setup and thus same β and κ values as looked in Fig. 4.3. Interestingly there are κ and β values, shown by the colorless region, where $\langle\hat{\chi}_1\hat{\chi}_3\rangle\langle\hat{P}_1\hat{P}_3\rangle > 0$, with the solid black lines showing where $\langle\hat{\chi}_1\hat{\chi}_3\rangle\langle\hat{P}_1\hat{P}_3\rangle = 0$. Thus from the PPT criterion given in Eq. (3.23), modes 1 and 3 are guaranteed to share no entanglement for this region of the phase space.

Appendix B

B.1 The General QDO Hamiltonian Applied in Material Simulation

The general dipole order QDO Hamiltonian in units of $\hbar\omega_0$ is

$$\begin{aligned}\hat{H}_g = \frac{1}{2}\sum_{\mu=1}^{N}|\hat{\boldsymbol{\mathcal{P}}}_\mu|^2 + \frac{1}{2}\sum_{\mu=1}^{N}|\hat{\boldsymbol{\chi}}_\mu|^2\frac{\omega_\mu^2}{\omega_0^2} + \\ \sum_{\mu>\xi}^{N}\frac{\omega_\mu\omega_\xi}{\omega_0^2}\sqrt{\alpha_\mu}\sqrt{\alpha_\xi}\hat{\boldsymbol{\chi}}_\mu e_\mu^T\mathcal{T}e_\xi\hat{\boldsymbol{\chi}}_\xi,\end{aligned} \tag{B.1}$$

where $\hat{\boldsymbol{\chi}}_\mu = \hat{\boldsymbol{r}}_\mu\sqrt{\omega_0 m/\hbar}$, $\hat{\boldsymbol{\mathcal{P}}}_\mu = \hat{\boldsymbol{p}}_\mu/\sqrt{\hbar m\omega_0}$. Here ω_0 is a reference frequency and $\alpha_\mu = q_\mu^2/(m_\mu\omega_\mu^2 4\pi\epsilon_0)$ is the polarizability of QDO μ.

The general dispersive binding energy is given by

$$E^g = \frac{3}{2}\sum_{\mu=1}^{N}\frac{\omega_\mu}{\omega_0} - \frac{1}{2}\sum_{i=1}^{3N}\sqrt{\lambda_i^g}, \tag{B.2}$$

where λ_i^g are the eigenvalues of the matrix V^g where $e_\mu^T V^g e_\mu = (\omega_\mu^2/\omega_0^2)\mathbb{1}_3$ and $e_\mu^T V^g e_\xi = \frac{\omega_\mu\omega_\xi}{\omega_0^2}\sqrt{\alpha_\mu}\sqrt{\alpha_\xi}e_\mu^T\mathcal{T}e_\xi$, given $\mu \neq \xi$. Note that e_μ as well as $\mathcal{T}$ have been defined in the main-text. The general covariance matrix is thus computable in terms of the matrix V^g, as $\gamma_0^g = (V^g)^{-1/2} \oplus (V^g)^{1/2}$. Here $((V^g)^{-1/2})_{ij} = \langle\hat{\chi}_i\hat{\chi}_j\rangle$ and $((V^g)^{1/2})_{ij} = \langle\hat{\mathcal{P}}_i\hat{\mathcal{P}}_j\rangle$. The more general CM γ_0^g, replaces the CM in Eq. (5.10), when numerically studying arbitrarily parameterized QDOs. Extracting the necessary entanglement information follows the same procedure as defined in Chapter 5, but instead now using the elements of γ_0^g.

Building on the general formulation of the dipole-order QDO Hamiltonian in Eq. (B.1) and its associated bond energy expression, we now discuss how solving variants of this Hamiltonian have been effectively integrated into quantum chemical simulations of realistic molecular systems via the so-called MBD method. This

method has been implemented in a range of electronic structure codes such as Q-Chem, Quantum ESPRESSO, and DFT-D4, as well as in standalone software packages [217].

In the MBD method the dipole order QDO Hamiltonian is constructed on top of a given density functional and thus exhibits a high degree of versatility, depending on both the choice of density functional and the specific procedure used to determine the QDO parameters. In the MBD@SCS approach [58], the QDO parameters $\{\omega_\mu, m_\mu, q_\mu\}$ are computed to encode modified free-atom polarizability reference data, with atomic volumes scaled according to the Hirshfeld-partitioned electron density obtained from a DFT calculation [217].

In this specifc MBD variant, the dipole interaction coupling matrix between QDOs μ and ξ, originally defined in Eq. (1) of the main text, is modified to account for the finite spatial extent of the QDO charge densities:

$$e_\mu^T \mathcal{T}^{\mathrm{scr}} e_\xi = \left(\mathrm{erf}(\zeta^{\mu,\xi}) - \Theta(\zeta^{\mu,\xi})\right) e_\mu^T \mathcal{T} e_\xi + 2\zeta^2 \Theta(\zeta^{\mu,\xi}) \frac{\boldsymbol{R}_{\mu\xi} \otimes \boldsymbol{R}_{\mu\xi}}{R_{\mu\xi}^5}, \tag{B.3}$$

where $\Theta(\zeta^{\mu,\xi}) = \frac{2\zeta^{\mu,\xi}}{\sqrt{\pi}} e^{-(\zeta^{\mu,\xi})^2}$ and $\zeta^{\mu,\xi} = R_{\mu\xi}/\sqrt{\sigma_\mu^2 + \sigma_\xi^2}$. The parameters σ_μ and σ_ξ represent the widths of the Gaussian charge densities associated with QDOs μ and ξ, respectively.

This modified interaction leads to the construction of a new screened dipole interaction matrix $\mathcal{T}^{\mathrm{scr}}$ of dimension $3N \times 3N$, which replaces $\mathcal{T}$ in Eq. (B.1). Since the quadratic form of the Hamiltonian is preserved, this modification acts only to appropriately regularize the dipole-dipole coupling at short range, while recovering the unscreened form in the long-range limit.

The MBD@SCS method has been benchmarked across a range of chemical datasets, notably improving the performance of the Perdew–Burke–Ernzerhof (PBE) functional [218] for non-covalent interactions. In the S66 test set, the inclusion of MBD corrections reduces the mean absolute error in interaction energies to 0.3 kcal/mol, compared to 2.3 kcal/mol for the uncorrected PBE functional [58].

Various versions of the MBD scheme, have demonstrated success across a wide range of simulated materials [6, 32, 33, 24, 219]. For example, applying MBD to the aforementioned PBE functional yields improved predictions for the relative stabilities of oxalic acid polymorphs [219], in agreement with experimental observations, unlike PBE alone. Moreover, the MBD approach has been shown to achieve accuracy comparable to diffusion quantum Monte Carlo for computing the binding energies of C_{70} complexes [28].

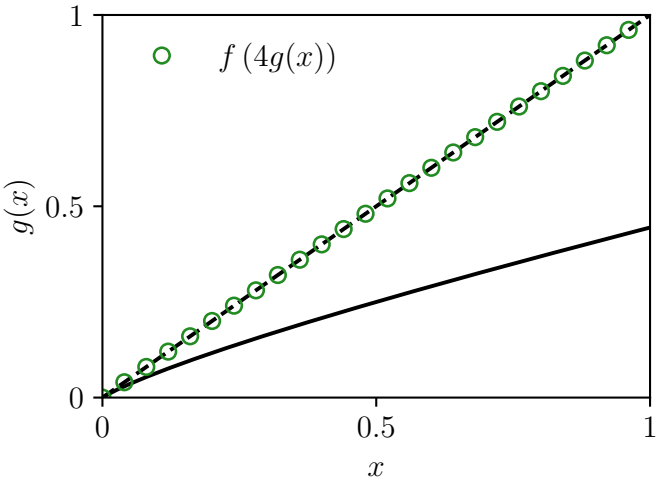

Figure B.1: The function $g(x)$ shown by the solid line, is used to define the reduced tangle. The reduced tangle is used to measures the entanglement in a bipartition between mode i and the other $3N-1$ modes in the QDO groundstate.

Even for materials where standard MBD underperforms, such as with transition-metal dichalcogenides [57] variants of the method, such as the MBD-NL [220], have been developed to overcome the challenges posed by specific systems. This highlights the generality and minimal empiricism of the overall framework.

B.2 Binomial Coefficients

The binomial coefficients are,

$$\sum_{k=0}^{\infty}\binom{-1/2}{k} = \sum_{k=0}^{\infty}(-1)^k\frac{(2k-1)!!}{(2k)!!} \tag{B.4}$$

and

$$\sum_{k=0}^{\infty}\binom{1/2}{k} = \sum_{k=0}^{\infty}(-1)^{k-1}\frac{(2k-3)!!}{(2k)!!}. \tag{B.5}$$

B.3 Properties of $g(x)$

Lemma. 7 $g(y) \geq g(x)$, given $y \geq x \geq 0$.

Proof. The derivative of $g(x)$ is non-negative for any positive x,

$$\frac{\partial\,(g(x))}{\partial_x} = \frac{1+\sqrt{x}(1+2\sqrt{x}+2x)}{(1+2\sqrt{x})^3} \geq 0, \quad \forall x \geq 0. \tag{B.6}$$

Lemma. 8 $g(x+y) \leq g(x)+g(y)$, given $x, y \geq 0$

Proof. The derivative of $g(x)/x$ is always negative for any positive x,

$$\frac{\partial\left(\frac{g(x)}{x}\right)}{\partial_x} = \frac{-(1+\sqrt{x})}{(1+2\sqrt{x})^3\sqrt{x}} \leq 0, \quad \text{given} \quad x \geq 0. \tag{B.7}$$

As a result for positive x and y, we can write,

$$\frac{g(y)}{y} \leq \frac{g(x)}{x}, \quad \text{if} \quad 0 \leq x \leq y. \tag{B.8}$$

Thus,

$$g(cx) \leq cg(x) \quad c \geq 1, \tag{B.9}$$

because c can always be written as $c = y/x$. As a result the inequality in Eq. (B.9) follows from Eq. (B.8). The subadditivity of $g(x)$ follows from inserting $c_1 = 1 + y/x$ into c in Eq. (B.9) and $c_2 = 1+x/y$ into c in Eq. (B.9) also. By adding and simplifying the resultant two inequalities, Eq. (B.9) implies $g(x+y) \leq g(x) + g(y)$, for positive x and y.

B.4 Negativity Bounds

The Gaussian tangle is defined as the squared negativity [79] hence,

$$\mathcal{N}(i) = \frac{1}{2}\left(||\hat{\rho}^{T_i}||_1 - 1\right). \tag{B.10}$$

Following from Eq. (3.7), the negativity between mode i and the other $3N-1$ modes in the system is given by

$$\mathcal{N}(i) = \frac{1}{2}\left(\sqrt{\langle\hat{\chi}_i^2\rangle\langle\hat{P}_i^2\rangle} + \sqrt{\langle\hat{\chi}_i^2\rangle\langle\hat{P}_i^2\rangle - 1} - 1\right). \tag{B.11}$$

We define $\mathcal{N} = \sum_{i=1}^{3N}\mathcal{N}(i)$. We consider here a QDO Hamiltonian of the form in Eq. (5.2) and further assume $\alpha\|\mathcal{T}\|_2 < 1$.

Using the definition of Δ_i in Eq. (5.20), the negativity can be rewritten as

$$\mathcal{N}(i) = \frac{1}{2}\left(\sqrt{\Delta_i + 1} + \sqrt{\Delta_i} - 1\right), \tag{B.12}$$

which by employing Bernoulli's inequality, stating that $(1+x)^r \leq 1 + xr$ for $|r| \leq 1$, leads to the following inequality,

$$\mathcal{N}(i) \leq \frac{1}{2}\sqrt{\Delta_i} + \frac{1}{4}\Delta_i. \tag{B.13}$$

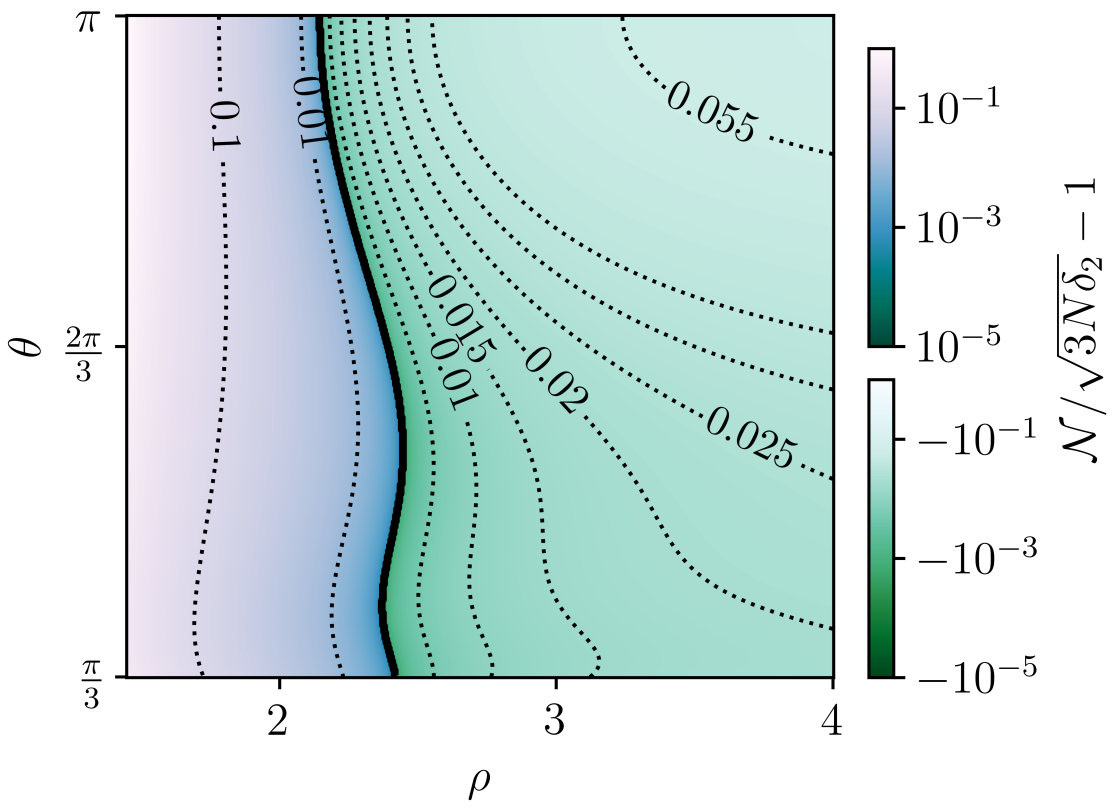

Figure B.2: Deviation between the negativity and $\sqrt{3N\delta_2}$, where δ_2 is the pairwise interaction energy. This is shown as a heatmap on a log-scale for the trimer system, depicted in Fig. 5.2. The black line shows where $\mathcal{N} = \sqrt{3N\delta_2}$, where to the right of the black line $\mathcal{N} < \sqrt{3N\delta_2}$ and to the left $\mathcal{N} > \sqrt{3N\delta_2}$.

By using the definition of $\mathcal{N}$, we can write

$$\mathcal{N} \leq \frac{1}{2}\sum_{i=1}^{3N}\left(\sqrt{\Delta_i} + \frac{1}{2}\Delta_i\right). \tag{B.14}$$

Then by employing the Cauchy-Schwartz inequality

$$\mathcal{N} \leq \frac{1}{2}\sqrt{3N\sum_{i=1}^{3N}\Delta_i} + \frac{1}{4}\Delta_i, \tag{B.15}$$

which from the Taylor series expansion of Δ_i (see Sec. 5.3), leads to

$$\mathcal{N} \leq \sqrt{3N\mathcal{S}_{l\to\infty}} + \mathcal{S}_{l\to\infty}, \tag{B.16}$$

where $\mathcal{S}_{l\to\infty} = \sum_{k=2}^{\infty}(k-1)\delta_k$ and δ_k is the kth body contribution to the dispersive binding energy, as per Eq. (5.4).

Fig. B.2, shows the close relationship between the negativity in the groundstate as measured by $\mathcal{N}$ and the pairwise bond energy, in the trimer setup (see Sec. 5.4 for more information on the trimer setup).

B.5 Further Bounds

B.5.1 Tangle bounds on the CM matrix

As $f(x) \geq \frac{x}{4}\ \forall x \geq 0$ (see lemma A.2), we derive an inequality relating the Gaussian tangle with the CM elements. The following inequality relates the Gaussian tangle and the reduced Gaussian tangle

$$\tau_G \geq \tilde{\tau}_G = \frac{1}{4}\mathrm{tr}(V^{1/2} \circ V^{-1/2} - \mathbb{1}), \tag{B.17}$$

where $\circ$ is the Hadamard product ($(A \circ B)_{ij} = A_{ij}B_{ij}$). This inequality follows from the definition of the Gaussian reduced tangle, we defined in Eq. (5.24). Note that Eq. (B.17) illustrates a simple forumlae for computing the net reduced tangle in the QDO groundstate.

B.5.2 Bounds on the deviation between the MB bond energy and the reduced tangle

Assuming $\alpha\|\mathcal{T}\|_2 < 1$ and using the bound in Eq. (5.19),

$$\tilde{\tau}_G - E + \sum_{k=4}^{\infty}\Xi_k\alpha^k\mathrm{tr}(\mathcal{T}^k) \leq \delta_{MB}. \tag{B.18}$$

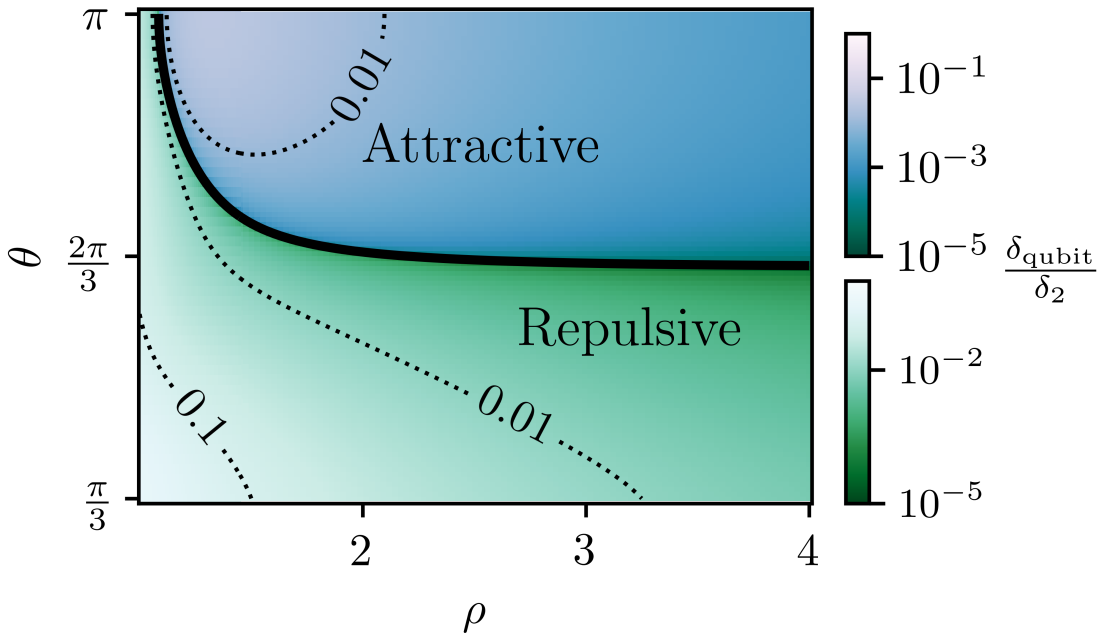

Figure B.3: Behavior of δ_{qubit}, normalized by the pairwise potential δ_2 as a function of trimer parameters ρ and θ (see main-text for trimer definition). The black line separates the phase space into regions where $\delta_{\text{qubit}} > 0$ and $\delta_{\text{qubit}} < 0$. Both regions are shown as heat-maps, plotted on a log-scale.

where,

$$\Xi_k = \frac{5(-1)^{k-1}(2k-3)!! + (-1)^k(2k-1)!!}{2^{k+2}k!}. \tag{B.19}$$

Then rearranging Eq. (B.18), we bound the deviation between the reduced tangle and many-body dispersive bond energy in terms of a function of the dipole-dipole interaction matrix $\mathcal{T}$ and the polarizability of the homogeneous QDO system, following from the definition of δ_{MB}.

B.6 Low Dimensional Trimer Approximation

Here we use Eq. (4.9) to approximate the QDO Hamiltonian. We set $d = 3N$ and $\alpha\mathcal{T}_{ij} = w_{ij}$, in Eq. (4.9), where $\mathcal{T}$ is the dipole-dipole interaction matrix and α is the QDO polarizability. The two level approximation of the QDO binding energy is given by,

$$E_{\text{qub}} = \frac{1}{2}\left(3N - \min[\text{eig}(\hat{H}^{d=3N}_{\text{qub}})]\right). \tag{B.20}$$

We compare the approximate measure of binding given by the qubit Hamiltonian, with the approximate measure of binding given by the pairwise approximation, by

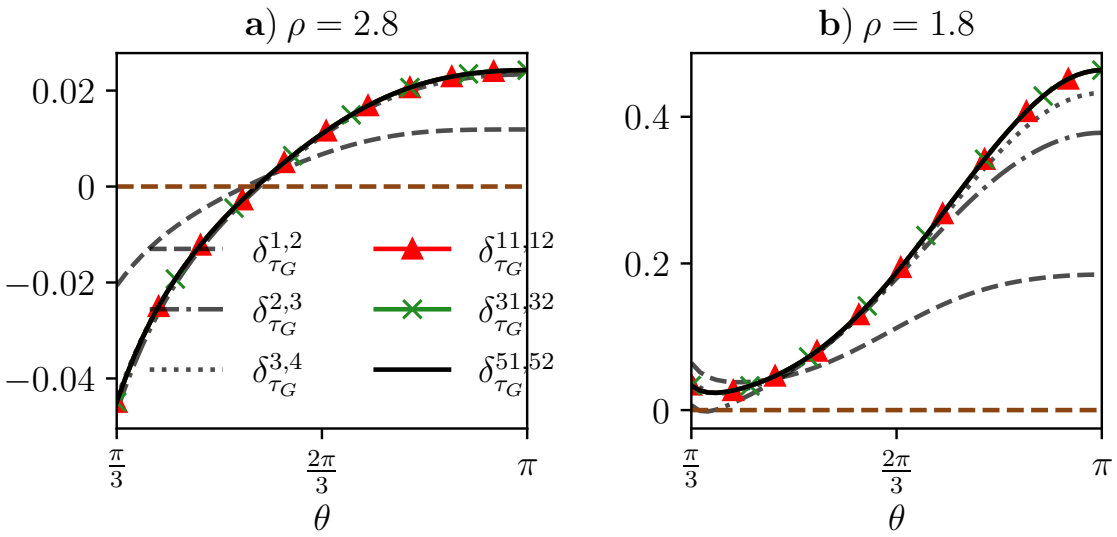

Figure B.4: The behavior of $\delta^{\mu,\mu+1}_{\tau_G}$ in QDOs at the edge of the chain differs from those at the center. The deviation between $\delta^{1,2}_{\tau_G}$ and $\delta^{51,52}_{\tau_G}$ is apparent in both **a)** and **b)**. In comparison for $\rho = 2.8$ $\delta^{2,3}_{\tau_G} \approx \delta^{51,52}_{\tau_G}$.

defining, $\delta_{\text{qub}} = E_{\text{qub}} - \delta_2$. This quantifies the extend to which Eq. (4.9) is able to capture the MB potential, for a N QDO system.

B.7 $\delta^{\mu,\mu+1}$ in Linear/Zigzag Chain

See Fig. B.4.

B.8 $|\delta_4| = |\delta_3|$ Trimer Boundary

See Fig. B.5.

B.9 Reduced Tangle Bounds on Lattices

In Fig. B.6, we show the convergence and tightness of the result in Eq. (5.19), for the different lattices we considered in the main-text in Sec. 5.4. The horizontal dashed brown line shows the value of the reduced tangle $\tilde{\tau}_G$ for different lattice geometries and lattice densities.

B.10 Trimer Distribution of $\tau^{\star}_G(i:j)$

See Fig. B.7.

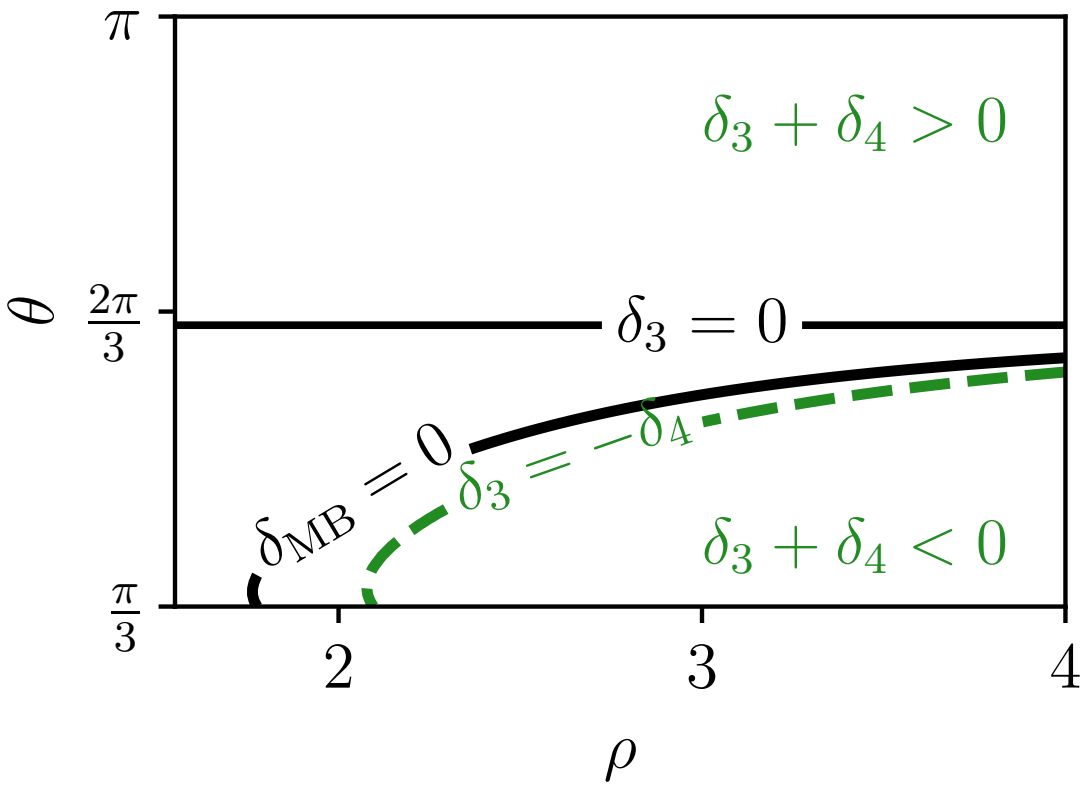

Figure B.5: The boundary where $E = \delta_2$ in the trimer setup is shown here by the solid black curve, $\delta_{MB} = 0$. The boundary between repulsive and attractive AT corrections is given by the horizontal black line $\delta_3 = 0$. The dashed green line shows where $\delta_3 = -\delta_4$. Above the green line $|\delta_4| > |\delta_3|$, whereas the region enclosed by the green dashed line shows the ρ and θ values where $|\delta_4| < |\delta_3|$.

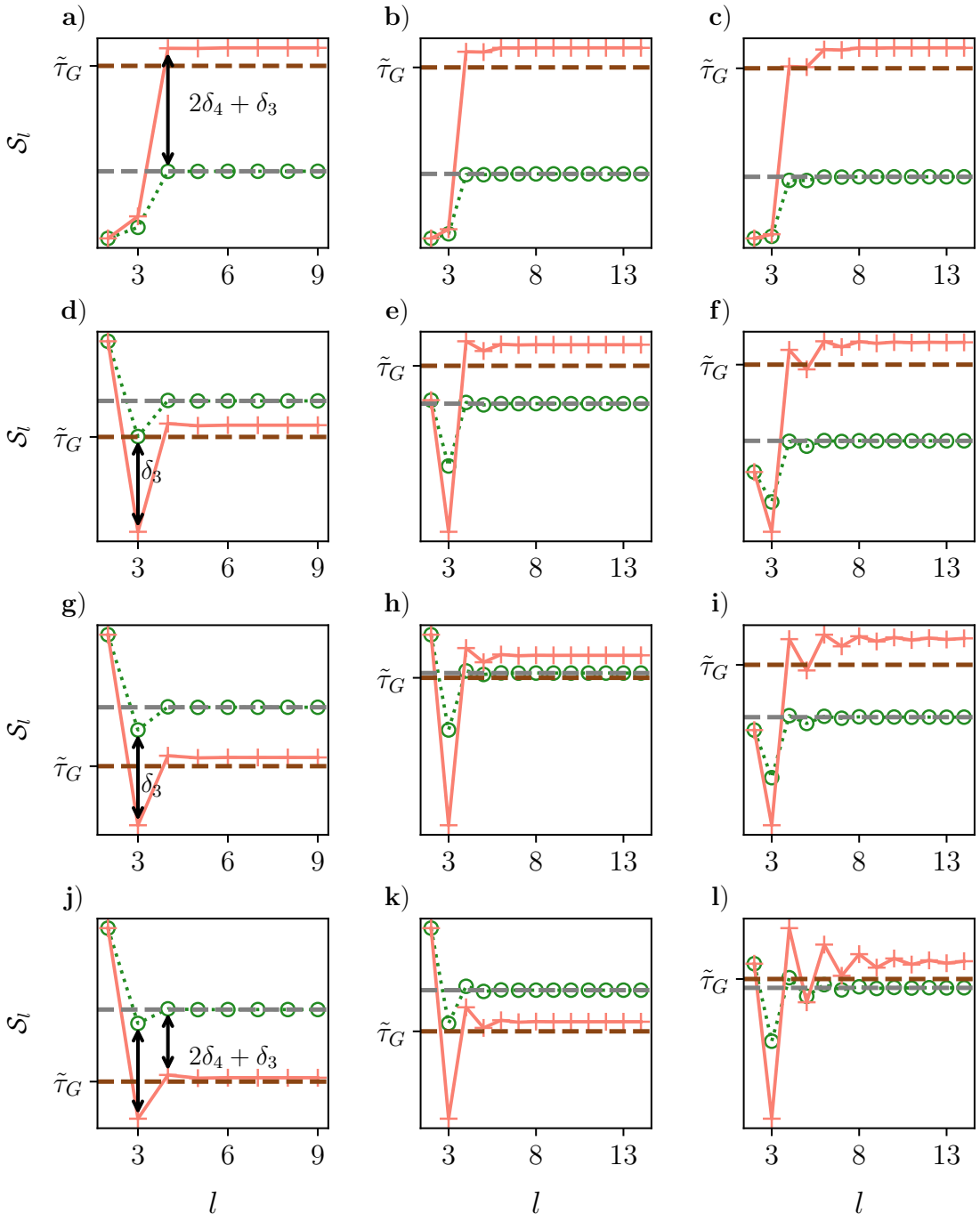

Figure B.6: The crosses show $\mathcal{S}_l = \sum_{k=2}^{l}(k-1)\delta_k$. The convergence to the bound in Eq. (5.19) can be seen, as for large l as the crosses lie above the brown dashed line, where this line shows the value of the groundstate entanglement, measured by $\tilde{\tau}_G$. The green open circles show the series $\sum_{k=2}^{l}\delta_k$ as a function of l, where $E = \sum_{k=1}^{l\to\infty}\delta_k$. **a**), **b**) and **c**) look at the honeycomb lattice. **d**), **e**) and **f**) looks at the square lattice. **g**), **h**) and **i**) considers the triangular lattice. Finally **j**), **k**) and **l**) shows the behavior on the cubic lattice. Going from left to the right $\rho = 4, 2.93$ and 2.29.

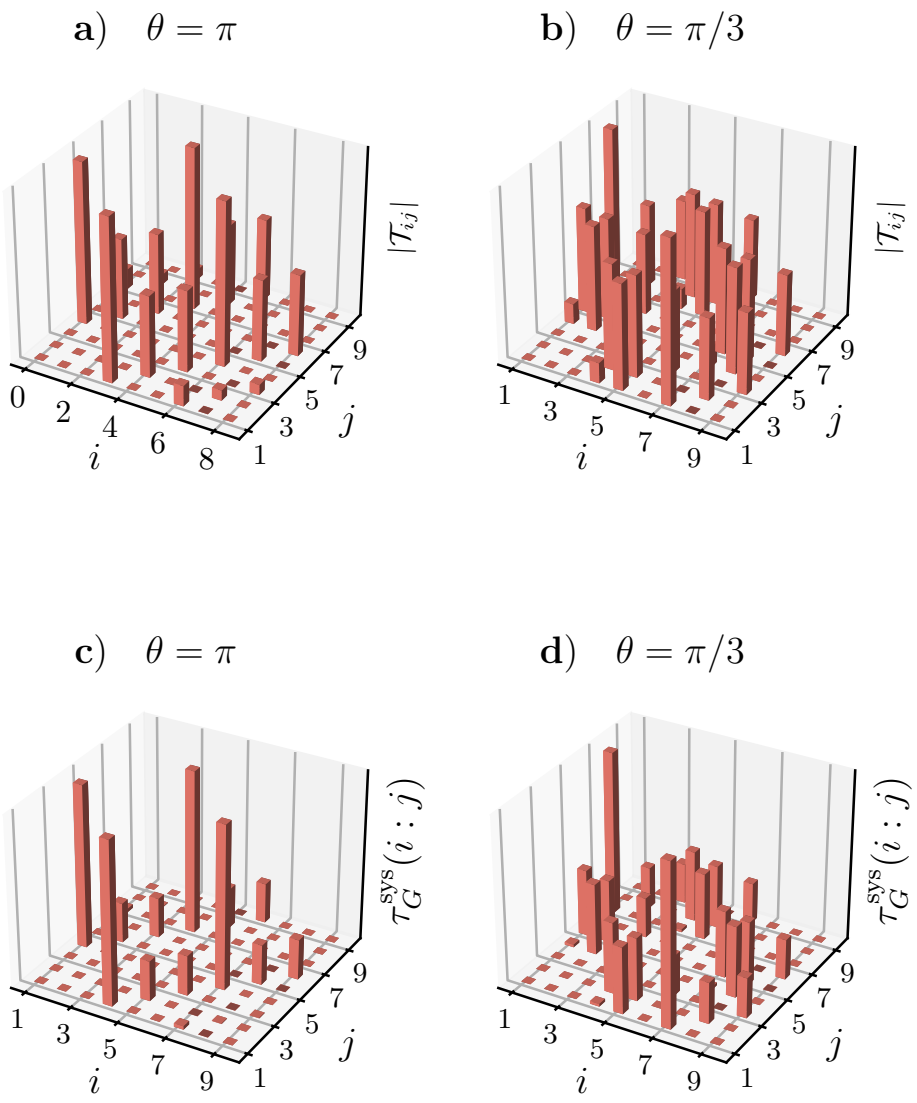

Figure B.7: **a)** – **b)** shows the strength of the dipole connection between modes i and j. **c)** – **b)** show the maximal allowed pairwise tangle, for each pair of modes i and j in the trimer ground state, consistent with the associated monogamy inequalities. **c)** shows the linear three QDO arrangement and **d)** shows the triangular geometry.

Appendix C

C.1 Symplectic Singular Value Decomposition (SVD)

Symplectic SVD factorization.- The set of $2d \times 2d$ symplectic matrices is

$$\mathcal{S}_p(2d,\mathbb{R}) = O_s^1 \underbrace{\begin{pmatrix} D & 0 \\ 0 & D^{-1} \end{pmatrix}}_{D\oplus D^{-1}} (O_s^2)^T \begin{cases} D = \mathrm{diag}(d_1, d_2, .., d_d), \\ D^{-1} = \mathrm{diag}(1/d_1, 1/d_2, .., 1/d_d), \\ O_s^1, O_s^2 \in \mathcal{S}p(2d,\mathbb{R}) \bigcap SO(2d,\mathbb{R}). \end{cases} \tag{C.1}$$

Here O_s^1 and O_s^2 denote symplectic orthogonal matrices. This symplectic decomposition is used to derive the form of the CM in Eq. (6.18) and is also referred to as the Bloch-Messiah decomposition.

C.2 Unit Triangular Factorization

For a symplectic matrix written in block-matrix form one may write the symplectic matrix constraint as follows if

$$S = \begin{pmatrix} A_1 & B_1 \\ A_2 & B_2 \end{pmatrix} \quad \text{and } A_i, B_i \in \mathbb{R}^{d\times d}, \forall i \in \{1,2\}. \tag{C.2}$$

then the following conditions must hold,

$$A_1^T A_2 = A_2^T A_1, \tag{C.3}$$

$$B_1^T B_2 = B_2^T B_1, \tag{C.4}$$

and

$$A_1^T B_2 - A_2^T B_1 = \mathbb{1}. \tag{C.5}$$

These conditions ensure that Eq. (2.23) is met and thus that S is a member of the symplectic matrix group, i.e $S \in \mathcal{S}_p(2d,\mathbb{R})$. Using this block form of the symplectic

matrix constraint, Ref. [170] showed the following are three valid factorizations for a symplectic matrix $S \in \mathcal{S}_p(2d, \mathbb{R})$,

$$\begin{cases} S = \begin{pmatrix} P_1 & 0 \\ 0 & P_1^{-T} \end{pmatrix} \begin{pmatrix} \mathbb{1} & 0 \\ S_1 & \mathbb{1} \end{pmatrix} \begin{pmatrix} \mathbb{1} & T_1 \\ 0 & \mathbb{1} \end{pmatrix} \\ S_1 = A_1^T A_2, T_1 = A_1^{-1} B_1, P_1 = A_1, \end{cases} \tag{C.6}$$

$$\begin{cases} S = \begin{pmatrix} \mathbb{1} & 0 \\ S_2 & \mathbb{1} \end{pmatrix} \begin{pmatrix} P_2 & 0 \\ 0 & P_2^{-T} \end{pmatrix} \begin{pmatrix} \mathbb{1} & T_2 \\ 0 & \mathbb{1} \end{pmatrix} \\ S_2 = A_2 A_1^{-1}, T_2 = A_1^{-1} B_1, P_2 = A_1, \end{cases} \tag{C.7}$$

and

$$\begin{cases} S = \begin{pmatrix} \mathbb{1} & 0 \\ S_3 & \mathbb{1} \end{pmatrix} \begin{pmatrix} \mathbb{1} & T_3 \\ 0 & \mathbb{1} \end{pmatrix} \begin{pmatrix} P_3 & 0 \\ 0 & P_3^{-T} \end{pmatrix} \\ S_3 = A_2 A_1^{-1}, T_3 = B_1 A_1^T, P_3 = A_1, \end{cases} \tag{C.8}$$

where S_1, S_2, S_3, T_1, T_2 and T_3 are all symmetric and P_1, P_2 and P_3 are non-singular. Ref. [170], showed how by decomposing $\begin{pmatrix} P_i & 0 \\ 0 & P_i^{-T} \end{pmatrix}$ into unit triangular matrices, an arbitrary symplectic matrix could be decomposed into a series of alternating unit triangular matrices, as is utilized in Sec. 6.3

C.3 Learning Entanglement in Harmonic Chain

Here we apply the symplectic optimization algorithm detailed in Sec. 6.3 to the harmonic chain, with Hamiltonian given in Eq. (3.30). In Fig. C.1, we show how the reduced tangle in the harmonic chain can be computed via the unconstrained symplectic optimization algorithm. Here we use the same numerical optimization techniques as outlined in Sec. 6.3. Also as was the case in Sec. 6.3, we define a call to the cost function as a step s. Each initial input to the CG algorithm (the initial matrix elements for M_1, M_2 and M_3) is randomly chosen in the range $(1/d)[0, 1]$, where d is the length of the chain. The tolerance of the CG descent algorithm is set here to tol $= 1 \times 10^{-8}$.

The relative error in the algorithm's approximation of the entanglement, per optimization step, is defined as

$$\epsilon_{\tilde{\tau}_G(i)} = \frac{\tilde{\tau}_G^\star(i) - \tilde{\tau}_G(i)}{\tilde{\tau}_G(i)}, \tag{C.9}$$

where $\tilde{\tau}_G(i)$ is the reduced tangle of mode i defined in Eq. (5.18). Then $\tilde{\tau}_G^\star(i)$ is the reduced tangle of mode i computed from the algorithm, using the approximation of

the CM from Eq. (6.16). Fig. C.1, shows the algorithm successfully learning the value of the reduced tangle, as a function of the number of calls to the cost function, for different chain sizes and different coupling strengths.

C.4 Hadamard Test

The Hadamard test is an algorithmic primitive, useful for computing expectations value of the form $\langle\psi|U|\psi\rangle$, where U is a unitary operator/ matrix and $|\psi\rangle$ is some prepared quantum state. Note that the circuit in Fig. C.2 shows the Hadmard test for computing the *real* part of the expectation value. The Hadmard test is able to measure the real and imaginary parts of an expectation value via two separate measurements by adding a single qubit phase gate, directly after the first Hadamard gate in Fig. C.2. Then a computational basis measurement of the ancilla qubit in it's zero state equals $0.5(1 + \mathrm{Im}[\langle\psi|U|\psi\rangle])$.

C.5 Block Matrix Ansatz

See Fig. C.3

C.6 Measuring Unitary Trace

We can compute the trace of a $2d \times 2d$ unitary matrix e.g U on a quantum computer, using the Hadamard test in Fig. C.4, which we will proceed to show here, using the methods outlined in Ref. [221].

We use the circuit illustrated in Fig. C.4. This uses 3 sub-registers S_1, S_2 and S_3. Both S_2, S_3 which will have n qubits, where recall that $n = \log_2(d)$, with d being the number of modes considered. The first step in Fig. C.4 is to maximally entangle the sub-registers S_2 and S_3 using single qubit Hadmard gates and two qubit controlled NOT gates,

$$|\Phi^+\rangle = \frac{1}{\sqrt{2d}} \sum_{\forall \boldsymbol{j}} |\boldsymbol{j}\rangle_{S_2} \otimes |\boldsymbol{j}\rangle_{S_3}, \tag{C.10}$$

with $\boldsymbol{j} = (j_1, .., j_{n+1})$ and $j_l \in \{0, 1\}$. Measuring the expectation value, $\langle\Phi^+|U \otimes \mathbb{1}|\Phi^+\rangle$, contains the information required to compute the trace of a unitary operator,

$$\langle\Phi^+|U \otimes \mathbb{1}|\Phi^+\rangle = \frac{1}{2d}\mathrm{tr}(U). \tag{C.11}$$

To compute the expectation value with error ϵ, the measurement needs to be repeated $\mathcal{O}(1/\epsilon^2)$ times.

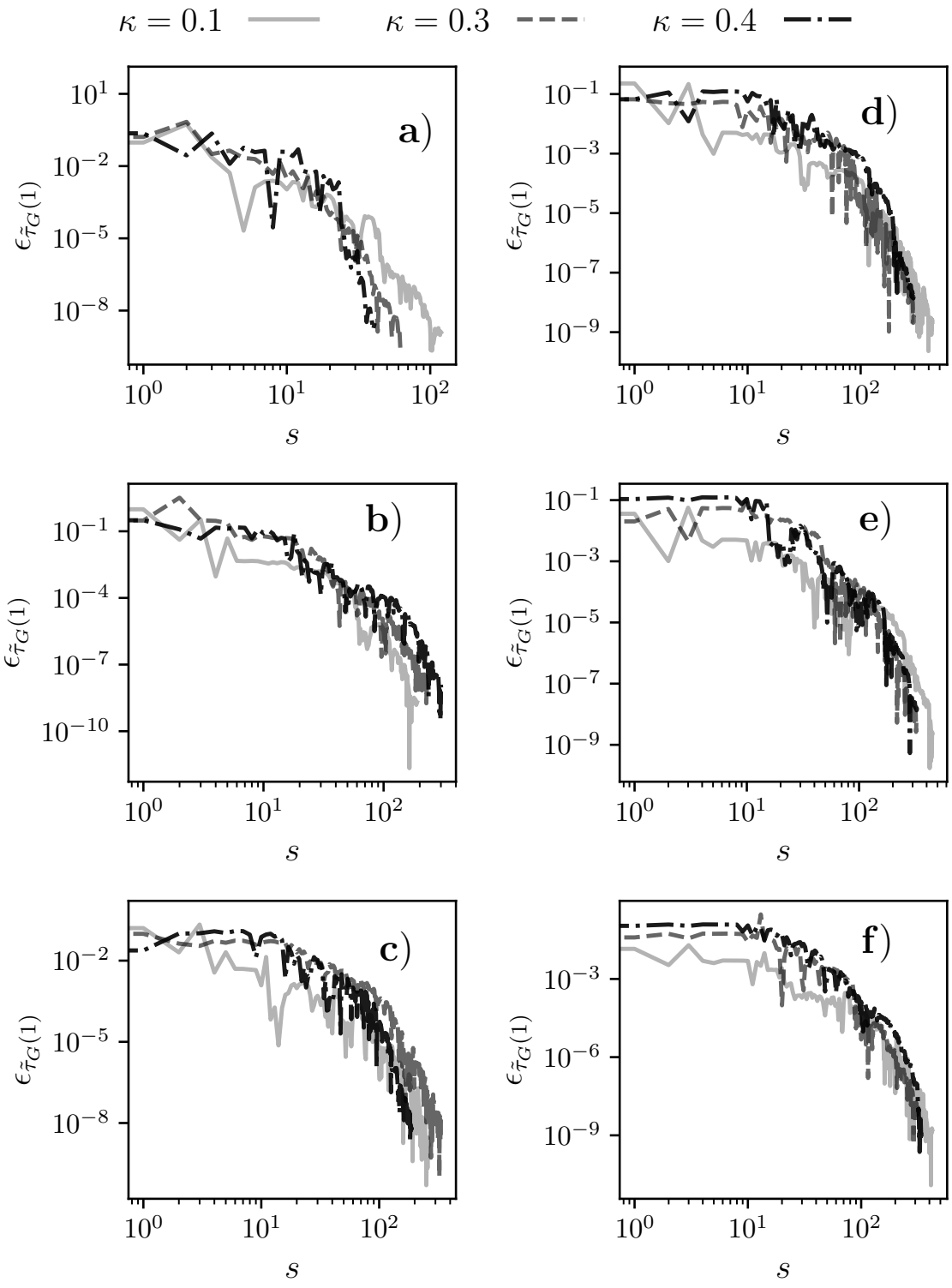

Figure C.1: Evolution of the symplectic trace cost function for different sizes of the harmonic chain. **a)** $d = 2$, **b)** $d = 4$, **c)** $d = 8$, **d)** $d = 16$, **e)** $d = 32$ and **f)** $d = 64$.

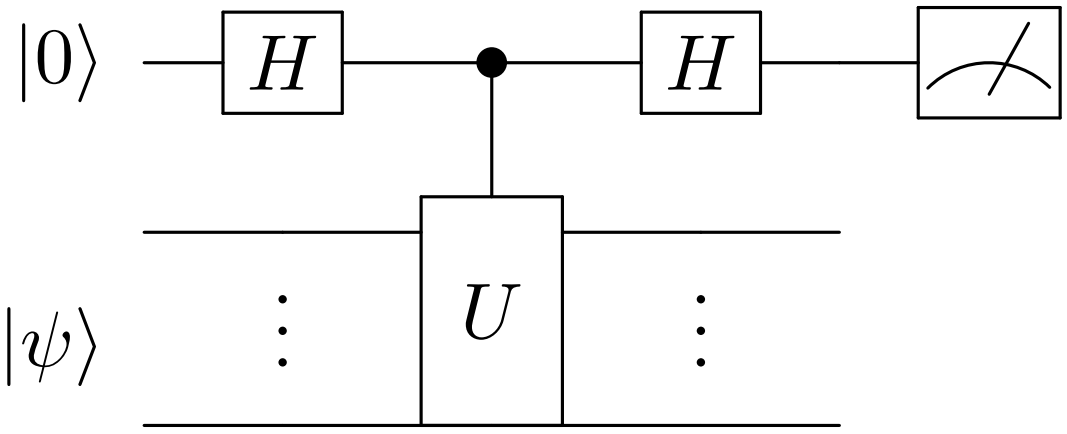

Figure C.2: Hadamard test circuit useful for computing the real part of the expectation, $\langle\psi|U|\psi\rangle$, where U is an unitary matrix and $|\psi\rangle$ is a quantum state. The Hadmard test, in addition to preparation of $|\psi\rangle$ and a controlled U operation, requires measurement of an ancilla qubit. The probability of measuring the ancilla qubit in the computational basis state $|0\rangle$ equals $0.5(1 + \mathrm{Re}[\langle\psi|U|\psi\rangle])$

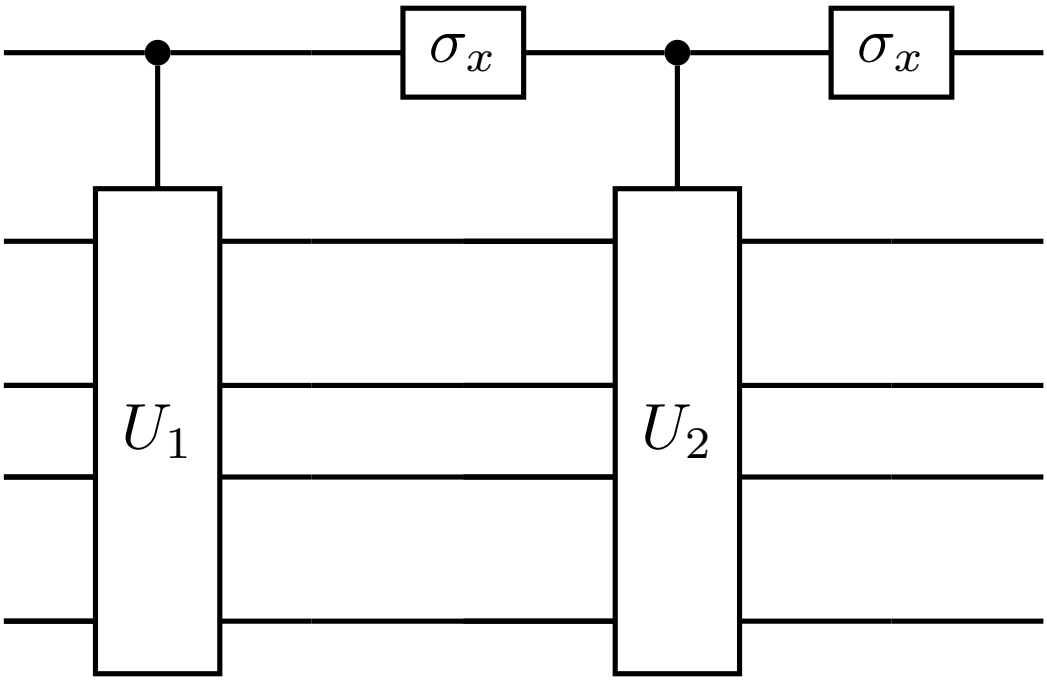

Figure C.3: Circuit implementing the block diagonal matrix $U_1 \oplus U_2$.

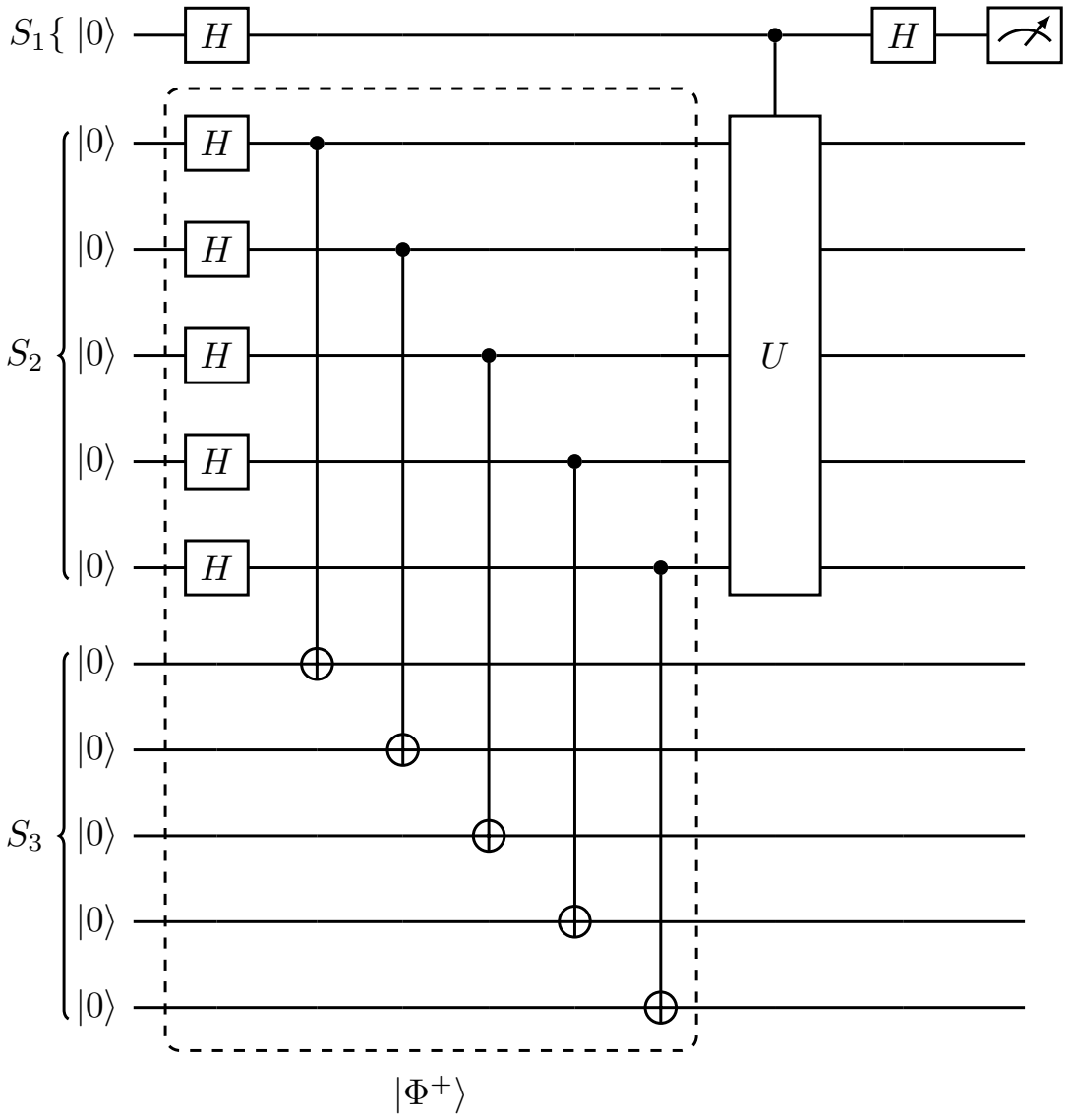

Figure C.4: Circuit for computing $\mathrm{tr}(U)$, where U is a unitary matrix.

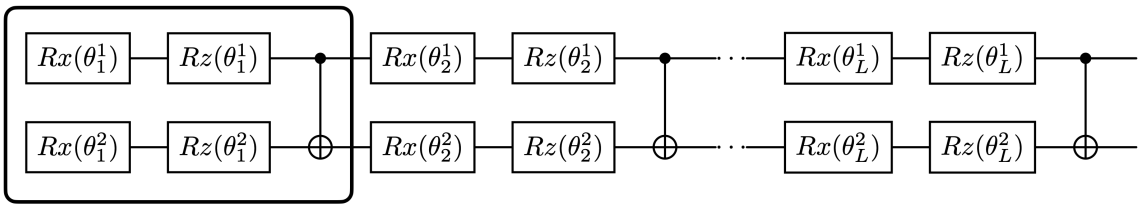

Figure C.5: Ansatz circuit used in Fig. C.6. $U(\boldsymbol{\theta})$ example for $n = 2$ qubits. The parameters for each layer (one layer is highlighted in the box) are given by $(\boldsymbol{\theta})_l = \{\theta_l^1, \theta_l^2, .., \theta_l^n\}$, where $l \in \{1, .., L\}$. The parameters are fed into the single qubit rotation gates $R_x(\theta_l^i)$ and $R_z(\theta_l^i)$, with $i \in \{1, .., n\}$. Entanglement between qubits is generated by two qubit CNOT gates.

C.7 Proof of Principle of VQA

The single qubit rotation gates, shown in Fig. C.5 are given as,

$$R_x(\theta_l^i) = \begin{pmatrix} \cos(\theta_l^i/2) & -\mathrm{i}\sin(\theta_l^i/2) \\ -\mathrm{i}\sin(\theta_l^i/2) & \cos(\theta_l^i/2) \end{pmatrix} \tag{C.12}$$

and

$$R_z(\theta_l^i) = \begin{pmatrix} e^{-\mathrm{i}\frac{\theta_l^i}{2}} & 0 \\ 0 & e^{-\mathrm{i}\frac{\theta_l^i}{2}} \end{pmatrix}. \tag{C.13}$$

The conjugate of Fig. C.5 is straightforward to computer as $U^\star(\boldsymbol{\theta}) = U(-\boldsymbol{\theta})$ as $R_x(-\theta_l^i) = R_x^\star(\theta_l^i)$ and $R_z(-\theta_l^i) = R_z^\star(\theta_l^i)$ both $\forall i \in \{1, .., n\}, \forall l \in \{1, .., L\}$. Thus in order to represent $U^\star(\boldsymbol{\theta})$ as a quantum circuit, we implement the circuit $U(-\boldsymbol{\theta})$, where $-\boldsymbol{\theta}^T = (-\boldsymbol{\theta}_1^T, .., -\boldsymbol{\theta}_L^T)$ and $(-\boldsymbol{\theta})_l^T = (-\theta_l^1, -\theta_l^2, .., -\theta_l^n)$. The inverse and transpose circuits, $U^\dagger(\boldsymbol{\theta})$ and $U^T(\boldsymbol{\theta})$, can then be computed via reversing the order of the circuit and inverting each of the two and single qubit gates.

In Fig. C.6, we show results for a two qubit ansatz and thus four mode system. The Hamiltonian we consider is the the $1D$ discretization of the Klein-Gordon Hamiltonian, given in Eq. (3.30). We set $d = 4$ and look at different coupling strengths. We build the ansatz circuit in Fig. C.6, enforcing the unitary constraint, and evaluate Eq. (6.25).

We use the CG algorithm to optimize Eq. (6.25), as was the case in Sec. 6.3. Here we set the tolerance to it's default value and our initial set of angles are all randomly chosen in the range $\{0, 1\}$. A step s is defined as the number of times the CG algorithm must evaluate Eq. (6.25). Note that the number of required steps for termination of the algorithm in Eq. (6.25) is much larger then in Eq. (6.2), as we do not have a closed form expression for the Jacobian of Eq. (6.25).

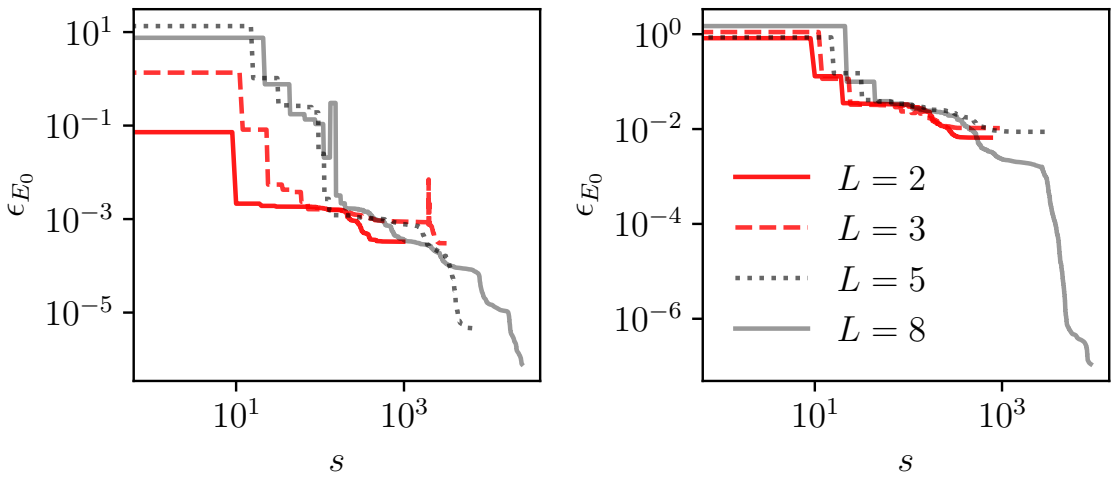

Figure C.6: Benchmarking the hybrid VQA for solving Eq. (6.3), described in Sec. 6.4. Error in the cost function's approximation of the groundstate energy at a step s (defined as a call to the cost function) is given as $\epsilon_{E_0} = (E_0^\star - E_0)/E_0$, where E_0 is the true groundstate energy. We use the VQA to solve Eq. (3.30) with $d = 4$ (Left) $\kappa = 0.1$ and (Right) $\kappa = 0.4$. The number of layers in the ansatz (see Fig. C.5) is specified by the integer L.

Fig. C.6 shows the increasing accuracy in the groundstate energy of the four mode system, for increased ansatz depth, given by L. The true groundstate energy of the chain is computed via symplectic diagonalization, as per Eq. (2.26). For small L values the termination of the CG algorithm at higher groundstate energies, is indicative of the presence of local minima. For both left and right plots in Fig. C.7, $L = 8$ is sufficient for accurate approximations of the groundstate energy.

C.8 Symplectic Ansatz

Fig. C.7 shows a parameterized circuit, which represents a general symplectic orthogonal matrix. See Ref [198] for more details.

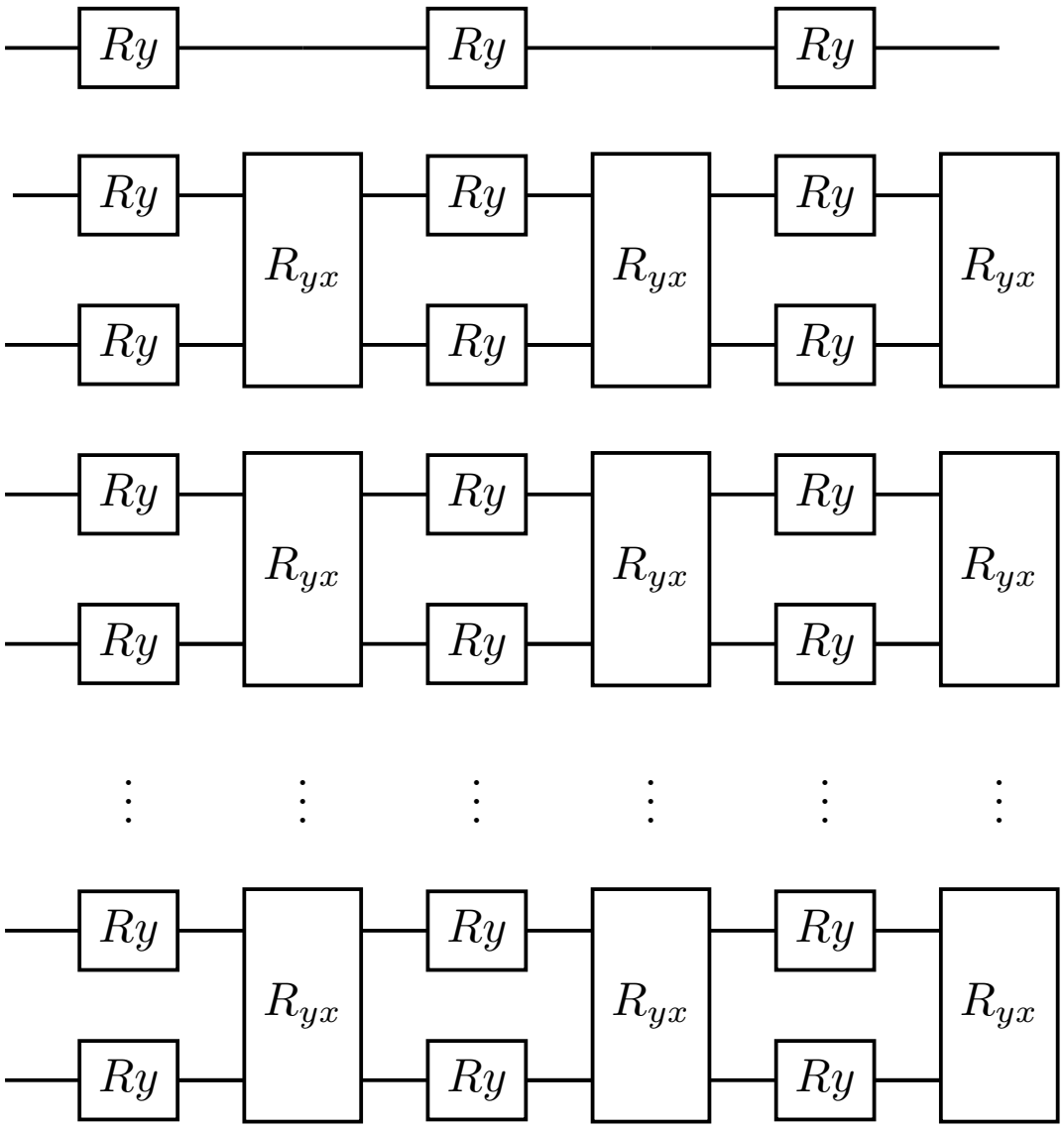

Figure C.7: Ansatz circuit which encodes a symplectic orthogonal matrix by design. The single qubit gates are R_y rotation gates and the two qubit entangling gates are R_{yx} rotation gates.

Bibliography

[1] Anthony Stone. *The Theory of Intermolecular Forces*. OUP oxford, 2013.

[2] Joseph O Hirschfelder. *Intermolecular Forces, Volume 12*, volume 12. John Wiley & Sons, 2009.

[3] Fritz London. Zur theorie und systematik der molekularkräfte. *Zeitschrift für Physik*, 63(3-4):245–279, 1930.

[4] Jan Hermann, Robert A DiStasio Jr, and Alexandre Tkatchenko. First-principles models for van der waals interactions in molecules and materials: Concepts, theory, and applications. *Chemical Reviews*, 117(6):4714–4758, 2017.

[5] Stefan Grimme. Density functional theory with london dispersion corrections. *Wiley Interdisciplinary Reviews: Computational Molecular Science*, 1(2):211–228, 2011.

[6] Robert A DiStasio, Vivekanand V Gobre, and Alexandre Tkatchenko. Many-body van der waals interactions in molecules and condensed matter. *Journal of Physics: Condensed Matter*, 26(21):213202, 2014.

[7] Ewa Pastorczak, Jun Shen, Michał Hapka, Piotr Piecuch, and Katarzyna Pernal. Intricacies of van der waals interactions in systems with elongated bonds revealed by electron-groups embedding and high-level coupled-cluster approaches. *Journal of Chemical Theory and Computation*, 13(11):5404–5419, 2017.

[8] O Anatole Von Lilienfeld, Ivano Tavernelli, Ursula Rothlisberger, and Daniel Sebastiani. Optimization of effective atom centered potentials for london dispersion forces in density functional theory. *Physical Review Letters*, 93(15):153004, 2004.

[9] Roger H French, V Adrian Parsegian, Rudolf Podgornik, Rick F Rajter, Anand Jagota, Jian Luo, Dilip Asthagiri, Manoj K Chaudhury, Yet-ming Chiang, Steve

Granick, et al. Long range interactions in nanoscale science. *Reviews of Modern Physics*, 82(2):1887, 2010.

[10] Igor E Dzyaloshinskii, Efrat M Lifshitz, and Lev P Pitaevskii. General theory of van der waals'forces. *Soviet Physics Uspekhi*, 4(2):153, 1961.

[11] Frank H Stillinger and Thomas A Weber. Computer simulation of local order in condensed phases of silicon. *Physical Review B*, 31(8):5262, 1985.

[12] BM Axilrod. Triple-dipole interaction. ii. cohesion in crystals of the rare gases. *The Journal of Chemical Physics*, 19(6):724–729, 1951.

[13] Laurens Jansen. Stability of crystals of rare-gas atoms and alkali halides in terms of three-body interactions. i. rare-gas crystals. *Physical Review*, 135(5A):A1292, 1964.

[14] Sören Rösel, Henrik Quanz, Christian Logemann, Jonathan Becker, Estelle Mossou, Laura Cañadillas-Delgado, Eike Caldeweyher, Stefan Grimme, and Peter R Schreiner. London dispersion enables the shortest intermolecular hydrocarbon h··· h contact. *Journal of the American Chemical Society*, 139(22):7428–7431, 2017.

[15] Leeor Kronik and Alexandre Tkatchenko. Understanding molecular crystals with dispersion-inclusive density functional theory: pairwise corrections and beyond. *Accounts of Chemical Research*, 47(11):3208–3216, 2014.

[16] J Philipp Wagner and Peter R Schreiner. London dispersion in molecular chemistry—reconsidering steric effects. *Angewandte Chemie International Edition*, 54(42):12274–12296, 2015.

[17] Andre K Geim and Irina V Grigorieva. Van der waals heterostructures. *Nature*, 499(7459):419–425, 2013.

[18] Vivekanand V Gobre and Alexandre Tkatchenko. Scaling laws for van der waals interactions in nanostructured materials. *Nature Communications*, 4(1):1–6, 2013.

[19] Michal Kolar, Tomas Kubar, and Pavel Hobza. On the role of london dispersion forces in biomolecular structure determination. *The Journal of Physical Chemistry B*, 115(24):8038–8046, 2011.

[20] Robert A DiStasio Jr, O Anatole von Lilienfeld, and Alexandre Tkatchenko. Collective many-body van der waals interactions in molecular systems. *Proceedings of the National Academy of Sciences*, 109(37):14791–14795, 2012.

[21] Martin Stöhr and Alexandre Tkatchenko. Quantum mechanics of proteins in explicit water: The role of plasmon-like solute-solvent interactions. *Science Advances*, 5(12):eaax0024, 2019.

[22] Alexandre Tkatchenko, Mariana Rossi, Volker Blum, Joel Ireta, and Matthias Scheffler. Unraveling the stability of polypeptide helices: critical role of van der waals interactions. *Physical Review Letters*, 106(11):118102, 2011.

[23] Kellar Autumn, Metin Sitti, Yiching A Liang, Anne M Peattie, Wendy R Hansen, Simon Sponberg, Thomas W Kenny, Ronald Fearing, Jacob N Israelachvili, and Robert J Full. Evidence for van der waals adhesion in gecko setae. *Proceedings of the National Academy of Sciences*, 99(19):12252–12256, 2002.

[24] Alberto Ambrosetti, Dario Alfè, Robert A DiStasio Jr, and Alexandre Tkatchenko. Hard numbers for large molecules: Toward exact energetics for supramolecular systems. *The Journal of Physical Chemistry Letters*, 5(5):849–855, 2014.

[25] Alexandre Tkatchenko, Robert A DiStasio Jr, Roberto Car, and Matthias Scheffler. Accurate and efficient method for many-body van der waals interactions. *Physical Review Letters*, 108(23):236402, 2012.

[26] Alston J Misquitta, Ryo Maezono, Neil D Drummond, Anthony J Stone, and Richard J Needs. Anomalous nonadditive dispersion interactions in systems of three one-dimensional wires. *Physical Review B*, 89(4):045140, 2014.

[27] Yaroslav V Shtogun and Lilia M Woods. Many-body van der waals interactions between graphitic nanostructures. *The Journal of Physical Chemistry Letters*, 1(9):1356–1362, 2010.

[28] Jan Hermann, Dario Alfe, and Alexandre Tkatchenko. Nanoscale π–π stacked molecules are bound by collective charge fluctuations. *Nature Communications*, 8(1):14052, 2017.

[29] Volker L Deringer and Gabor Csanyi. Many-body dispersion correction effects on bulk and surface properties of rutile and anatase tio2. *The Journal of Physical Chemistry C*, 120(38):21552–21560, 2016.

[30] Won June Kim, Minho Kim, Eok Kyun Lee, Sebastien Lebegue, and Hyungjun Kim. Failure of density functional dispersion correction in metallic systems and its possible solution using a modified many-body dispersion correction. *The Journal of Physical Chemistry Letters*, 7(16):3278–3283, 2016.

[31] Noa Marom, Robert A DiStasio Jr, Viktor Atalla, Sergey Levchenko, Anthony M Reilly, James R Chelikowsky, Leslie Leiserowitz, and Alexandre Tkatchenko. Many-body dispersion interactions in molecular crystal polymorphism. *Angewandte Chemie International Edition*, 52(26):6629–6632, 2013.

[32] Anthony M Reilly and Alexandre Tkatchenko. Role of dispersion interactions in the polymorphism and entropic stabilization of the aspirin crystal. *Physical Review Letters*, 113(5):055701, 2014.

[33] Anthony M Reilly and Alexandre Tkatchenko. Seamless and accurate modeling of organic molecular materials. *The Journal of Physical Chemistry Letters*, 4(6):1028–1033, 2013.

[34] Krzysztof Rościszewski, Beate Paulus, Peter Fulde, and Hermann Stoll. Ab initio coupled-cluster calculations for the fcc and hcp structures of rare-gas solids. *Physical Review B*, 62(9):5482, 2000.

[35] Tal Maaravi, Itai Leven, Ido Azuri, Leeor Kronik, and Oded Hod. Interlayer potential for homogeneous graphene and hexagonal boron nitride systems: reparametrization for many-body dispersion effects. *The Journal of Physical Chemistry C*, 121(41):22826–22835, 2017.

[36] Rodney J Bartlett and Monika Musiał. Coupled-cluster theory in quantum chemistry. *Reviews of Modern Physics*, 79(1):291–352, 2007.

[37] Robert O Jones. Density functional theory: Its origins, rise to prominence, and future. *Reviews of Modern Physics*, 87(3):897–923, 2015.

[38] FS Cipcigan, Jason Crain, VP Sokhan, and Glenn J Martyna. Electronic coarse graining: Predictive atomistic modeling of condensed matter. *Reviews of Modern Physics*, 91(2):025003, 2019.

[39] Kestutis Aidas, Celestino Angeli, Keld L Bak, Vebjørn Bakken, Radovan Bast, Linus Boman, Ove Christiansen, Renzo Cimiraglia, Sonia Coriani, Pål Dahle, et al. The d alton quantum chemistry program system. *Wiley Interdisciplinary Reviews: Computational Molecular Science*, 4(3):269–284, 2014.

[40] Frank Jensen. *Introduction to computational chemistry*. John wiley & sons, 2017.

[41] Chr Møller and Milton S Plesset. Note on an approximation treatment for many-electron systems. *Physical Review*, 46(7):618, 1934.

[42] Alberto Baiardi and Markus Reiher. The density matrix renormalization group in chemistry and molecular physics: Recent developments and new challenges. *The Journal of Chemical Physics*, 152(4), 2020.

[43] Trygve Helgaker, Wim Klopper, and David P Tew. Quantitative quantum chemistry. *Molecular Physics*, 106(16-18):2107–2143, 2008.

[44] A Jones, F Cipcigan, VP Sokhan, J Crain, and GJ Martyna. Electronically coarse-grained model for water. *Physical Review Letters*, 110(22):227801, 2013.

[45] Ornella Vaccarelli, Dmitry V Fedorov, Martin Stöhr, and Alexandre Tkatchenko. Quantum-mechanical force balance between multipolar dispersion and pauli repulsion in atomic van der waals dimers. *Physical Review Research*, 3(3):033181, 2021.

[46] WL Bade. Drude-model calculation of dispersion forces. i. general theory. *The Journal of Chemical Physics*, 27(6):1280–1284, 1957.

[47] Feng Wang and KD Jordan. A drude-model approach to dispersion interactions in dipole-bound anions. *The Journal of Chemical Physics*, 114(24):10717–10724, 2001.

[48] Andrew P Jones, Jason Crain, Vlad P Sokhan, Troy W Whitfield, and Glenn J Martyna. Quantum drude oscillator model of atoms and molecules: Many-body polarization and dispersion interactions for atomistic simulation. *Physical Review B*, 87(14):144103, 2013.

[49] AG Donchev. Many-body effects of dispersion interaction. *The Journal of Chemical Physics*, 125(7):074713, 2006.

[50] Flaviu S Cipcigan, Vlad P Sokhan, Jason Crain, and Glenn J Martyna. Electronic coarse graining enhances the predictive power of molecular simulation allowing challenges in water physics to be addressed. *Journal of Computational Physics*, 326:222–233, 2016.

[51] Fritz London. The general theory of molecular forces. *Transactions of the Faraday Society*, 33:8b–26, 1937.

[52] MJ Sparnaay. On the additivity of london-van der waals forces: An extension of london's oscillator model. *Physica*, 25(1-6):217–231, 1959.

[53] Joseph Oakland Hirschfelder, Charles F Curtiss, and R Byron Bird. Molecular theory of gases and liquids. *Molecular Theory of Gases and Liquids*, 1964.

[54] J Cao and BJ Berne. Many-body dispersion forces of polarizable clusters and liquids. *The Journal of Chemical Physics*, 97(11):8628–8636, 1992.

[55] Martin Stöhr, Mainak Sadhukhan, Yasmine S Al-Hamdani, Jan Hermann, and Alexandre Tkatchenko. Coulomb interactions between dipolar quantum fluctuations in van der waals bound molecules and materials. *Nature Communications*, 12(1):137, 2021.

[56] Almaz Khabibrakhmanov, Dmitry V Fedorov, and Alexandre Tkatchenko. Universal pairwise interatomic van der waals potentials based on quantum drude oscillators. *Journal of Chemical Theory and Computation*, 2023.

[57] Kyle R Bryenton and Erin R Johnson. Many-body dispersion in model systems and the sensitivity of self-consistent screening. *The Journal of Chemical Physics*, 158(20), 2023.

[58] Alberto Ambrosetti, Anthony M Reilly, Robert A DiStasio, and Alexandre Tkatchenko. Long-range correlation energy calculated from coupled atomic response functions. *The Journal of chemical physics*, 140(18), 2014.

[59] Gerardo Adesso, Sammy Ragy, and Antony R Lee. Continuous variable quantum information: Gaussian states and beyond. *Open Systems & Information Dynamics*, 21(01n02):1440001, 2014.

[60] Christian Weedbrook, Stefano Pirandola, Raúl García-Patrón, Nicolas J Cerf, Timothy C Ralph, Jeffrey H Shapiro, and Seth Lloyd. Gaussian quantum information. *Reviews of Modern Physics*, 84(2):621, 2012.

[61] Norbert Schuch, J Ignacio Cirac, and Michael M Wolf. Quantum states on harmonic lattices. *Communications in Mathematical Physics*, 267(1):65–92, 2006.

[62] Michael M Wolf, Frank Verstraete, and J Ignacio Cirac. Entanglement frustration for gaussian states on symmetric graphs. *Physical Review Letters*, 92(8):087903, 2004.

[63] Alessio Serafini. *Quantum continuous variables: A Primer of Theoretical Methods*. CRC press, 2017.

[64] Jan Dereziński. Bosonic quadratic hamiltonians. *Journal of Mathematical Physics*, 58(12):121101, 2017.

[65] JHP Colpa. Diagonalization of the quadratic boson hamiltonian. *Physica A: Statistical Mechanics and its Applications*, 93(3-4):327–353, 1978.

[66] JL Van Hemmen. A note on the diagonalization of quadratic boson and fermion hamiltonians. *Zeitschrift für Physik B Condensed Matter*, 38(3):271–277, 1980.

[67] Osvaldo Maldonado. On the bogoliubov transformation for quadratic boson observables. *Journal of Mathematical Physics*, 34(11):5016–5027, 1993.

[68] Géza Giedke, Michael M Wolf, Ole Krüger, Reinhard F Werner, and J Ignacio Cirac. Entanglement of formation for symmetric gaussian states. *Physical Review Letters*, 91(10):107901, 2003.

[69] G Giedke, B Kraus, M Lewenstein, and JI Cirac. Entanglement criteria for all bipartite gaussian states. *Physical Review Letters*, 87(16):167904, 2001.

[70] Marcus Cramer, Jens Eisert, Martin B Plenio, and J Dreissig. Entanglement-area law for general bosonic harmonic lattice systems. *Physical Review A*, 73(1):012309, 2006.

[71] Martin B Plenio, Jens Eisert, J Dreissig, and Marcus Cramer. Entropy, entanglement, and area: analytical results for harmonic lattice systems. *Physical Review Letters*, 94(6):060503, 2005.

[72] Jens Eisert and MB1069 Plenio. Introduction to the basics of entanglement theory in continuous-variable systems. *International Journal of Quantum Information*, 1(04):479–506, 2003.

[73] Mattia Walschaers. Non-gaussian quantum states and where to find them. *PRX quantum*, 2(3):030204, 2021.

[74] Barbara M Terhal. Is entanglement monogamous? *IBM Journal of Research and Development*, 48(1):71–78, 2004.

[75] Gerardo Adesso and Fabrizio Illuminati. Entanglement sharing: from qubits to gaussian states. *International Journal of Quantum Information*, 4(03):383–393, 2006.

[76] Ryszard Horodecki, Paweł Horodecki, Michał Horodecki, and Karol Horodecki. Quantum entanglement. *Reviews of modern physics*, 81(2):865, 2009.

[77] Valerie Coffman, Joydip Kundu, and William K Wootters. Distributed entanglement. *Physical Review A*, 61(5):052306, 2000.

[78] Tobias J Osborne and Frank Verstraete. General monogamy inequality for bipartite qubit entanglement. *Physical Review Letters*, 96(22):220503, 2006.

[79] Tohya Hiroshima, Gerardo Adesso, and Fabrizio Illuminati. Monogamy inequality for distributed gaussian entanglement. *Physical Review Letters*, 98(5):050503, 2007.

[80] Michael M Wolf, Frank Verstraete, and J Ignacio Cirac. Entanglement and frustration in ordered systems. *International Journal of Quantum Information*, 1(04):465–477, 2003.

[81] Marcin Pawłowski. Security proof for cryptographic protocols based only on the monogamy of bell's inequality violations. *Physical Review A*, 82(3):032313, 2010.

[82] Seth Lloyd and John Preskill. Unitarity of black hole evaporation in final-state projection models. *Journal of High Energy Physics*, 2014(8):1–30, 2014.

[83] Michael P Seevinck. Monogamy of correlations versus monogamy of entanglement. *Quantum Information Processing*, 9:273–294, 2010.

[84] Masato Koashi and Andreas Winter. Monogamy of quantum entanglement and other correlations. *Physical Review A*, 69(2):022309, 2004.

[85] Kevin M O'Connor and William K Wootters. Entangled rings. *Physical Review A*, 63(5):052302, 2001.

[86] Alessandro Ferraro, Artur García-Saez, and Antonio Acín. Monogamy and ground-state entanglement in highly connected systems. *Physical Review A*, 76(5):052321, 2007.

[87] Gerardo Adesso, Marie Ericsson, and Fabrizio Illuminati. Coexistence of unlimited bipartite and genuine multipartite entanglement: Promiscuous quantum correlations arising from discrete to continuous-variable systems. *Physical Review A*, 76(2):022315, 2007.

[88] Yu Wang, PJ Knowles, and Jian Wang. Information entropy as a measure of the correlation energy associated with the cumulant. *Physical Review A*, 103(6):062808, 2021.

[89] Jian Wang and Evert Jan Baerends. Self-consistent-field method for correlated many-electron systems with an entropic cumulant energy. *Physical Review Letters*, 128(1):013001, 2022.

[90] Jerzy Cioslowski and Krzysztof Strasburger. Constraints upon functionals of the 1-matrix, universal properties of natural orbitals, and the fallacy of the collins "conjecture". *The Journal of Physical Chemistry Letters*, 15(5):1328–1337, 2024.

[91] Douglas M Collins. Entropy maximizations on electron density. *Zeitschrift für Naturforschung A*, 48(1-2):68–74, 1993.

[92] Bennet Windt, Alexander Jahn, Jens Eisert, and Lucas Hackl. Local optimization on pure gaussian state manifolds. *SciPost Physics*, 10(3):066, 2021.

[93] Lieven Vandenberghe and Stephen Boyd. Semidefinite programming. *SIAM review*, 38(1):49–95, 1996.

[94] Michel X Goemans and David P Williamson. Improved approximation algorithms for maximum cut and satisfiability problems using semidefinite programming. *Journal of the ACM (JACM)*, 42(6):1115–1145, 1995.

[95] Jianqing Fan, Yuan Liao, and Han Liu. An overview of the estimation of large covariance and precision matrices. *The Econometrics Journal*, 19(1):C1–C32, 2016.

[96] Bo Jiang, Shiqian Ma, and Shuzhong Zhang. Tensor principal component analysis via convex optimization. *Mathematical Programming*, 150(2):423–457, 2015.

[97] Zhaoliang Chen and Shiping Wang. A review on matrix completion for recommender systems. *Knowledge and Information Systems*, 64(1):1–34, 2022.

[98] Adrian S Lewis. The mathematics of eigenvalue optimization. *Mathematical Programming*, 97:155–176, 2003.

[99] Sergio Blanes and Per Christian Moan. Practical symplectic partitioned runge–kutta and runge–kutta–nyström methods. *Journal of Computational and Applied Mathematics*, 142(2):313–330, 2002.

[100] J Candy and W Rozmus. A symplectic integration algorithm for separable hamiltonian functions. *Journal of Computational Physics*, 92(1):230–256, 1991.

[101] Hong Qin and Xiaoyin Guan. A variational symplectic integrator for the guiding center motion of charged particles for long time simulations in general magnetic fields. *Phys. Rev. Lett*, 100:035006, 2008.

[102] Molei Tao. Explicit symplectic approximation of nonseparable hamiltonians: Algorithm and long time performance. *Physical Review E*, 94(4):043303, 2016.

[103] Michael Betancourt, Michael I Jordan, and Ashia C Wilson. On symplectic optimization. *arXiv preprint arXiv:1802.03653*, 2018.

[104] Marco David and Florian Méhats. Symplectic learning for hamiltonian neural networks. *Journal of Computational Physics*, 494:112495, 2023.

[105] Hong Qin, Jian Liu, Jianyuan Xiao, Ruili Zhang, Yang He, Yulei Wang, Yajuan Sun, Joshua W Burby, Leland Ellison, and Yao Zhou. Canonical symplectic particle-in-cell method for long-term large-scale simulations of the vlasov–maxwell equations. *Nuclear Fusion*, 56(1):014001, 2015.

[106] Alberto Peruzzo, Jarrod McClean, Peter Shadbolt, Man-Hong Yung, Xiao-Qi Zhou, Peter J Love, Alán Aspuru-Guzik, and Jeremy L O'brien. A variational eigenvalue solver on a photonic quantum processor. *Nature Communications*, 5(1):4213, 2014.

[107] Michael Lubasch, Jaewoo Joo, Pierre Moinier, Martin Kiffner, and Dieter Jaksch. Variational quantum algorithms for nonlinear problems. *Physical Review A*, 101(1):010301, 2020.

[108] Marco Cerezo, Andrew Arrasmith, Ryan Babbush, Simon C Benjamin, Suguru Endo, Keisuke Fujii, Jarrod R McClean, Kosuke Mitarai, Xiao Yuan, Lukasz Cincio, et al. Variational quantum algorithms. *Nature Reviews Physics*, 3(9):625–644, 2021.

[109] Aleksey K Fedorov and Mikhail S Gelfand. Towards practical applications in quantum computational biology. *Nature Computational Science*, 1(2):114–119, 2021.

[110] Lewis W Anderson, Martin Kiffner, Panagiotis Kl Barkoutsos, Ivano Tavernelli, Jason Crain, and Dieter Jaksch. Coarse-grained intermolecular interactions on quantum processors. *Physical Review A*, 105(6):062409, 2022.

[111] Matthieu Sarkis, Alessio Fallani, and Alexandre Tkatchenko. Modeling noncovalent interatomic interactions on a photonic quantum computer. *arXiv preprint arXiv:2306.08544*, 2023.

[112] Ali Javadi-Abhari, Matthew Treinish, Kevin Krsulich, Christopher J Wood, Jake Lishman, Julien Gacon, Simon Martiel, Paul D Nation, Lev S Bishop, Andrew W Cross, et al. Quantum computing with qiskit. *arXiv preprint arXiv:2405.08810*, 2024.

[113] J Robert Johansson, Paul D Nation, and Franco Nori. Qutip: An open-source python framework for the dynamics of open quantum systems. *Computer physics communications*, 183(8):1760–1772, 2012.

[114] Jérôme Manuceau and André Verbeure. Quasi-free states of the ccr—algebra and bogoliubov transformations. *Communications in Mathematical Physics*, 9:293–302, 1968.

[115] AS Holevo. Generalized free states of the c-algebra of the ccr. *Theor. Math. Phys*, 6(1):3–20, 1971.

[116] Janet Anders. Estimating the degree of entanglement of unknown gaussian states. *arXiv preprint quant-ph/0610263*, 2006.

[117] Stefano Pirandola, Alessio Serafini, and Seth Lloyd. Correlation matrices of two-mode bosonic systems. *Physical Review A*, 79(5):052327, 2009.

[118] Robin L Hudson. When is the wigner quasi-probability density non-negative? *Reports on Mathematical Physics*, 6(2):249–252, 1974.

[119] Michael M Wolf, Geza Giedke, Ole Krüger, Reinhard F Werner, and J Ignacio Cirac. Gaussian entanglement of formation. *Physical Review A*, 69(5):052320, 2004.

[120] John Williamson. On the algebraic problem concerning the normal forms of linear dynamical systems. *American Journal of Mathematics*, 58(1):141–163, 1936.

[121] Koenraad Audenaert, Jens Eisert, Martin B Plenio, and Reinhard F Werner. Entanglement properties of the harmonic chain. *Physical Review A*, 66(4):042327, 2002.

[122] Michael A Nielsen and Isaac L Chuang. *Quantum computation and quantum information*. Cambridge university press, 2010.

[123] Nicolas Gisin, Grégoire Ribordy, Wolfgang Tittel, and Hugo Zbinden. Quantum cryptography. *Reviews of modern physics*, 74(1):145, 2002.

[124] Stefano Pirandola, Jens Eisert, Christian Weedbrook, Akira Furusawa, and Samuel L Braunstein. Advances in quantum teleportation. *Nature photonics*, 9(10):641–652, 2015.

[125] Eric Chitambar, Debbie Leung, Laura Mančinska, Maris Ozols, and Andreas Winter. Everything you always wanted to know about locc (but were afraid to ask). *Communications in Mathematical Physics*, 328:303–326, 2014.

[126] Yu Luo, Tian Tian, Lian-He Shao, and Yongming Li. General monogamy of tsallis q-entropy entanglement in multiqubit systems. *Physical Review A*, 93(6):062340, 2016.

[127] Wei Song, Yan-Kui Bai, Mou Yang, Ming Yang, and Zhuo-Liang Cao. General monogamy relation of multiqubit systems in terms of squared rényi-α entanglement. *Physical Review A*, 93(2):022306, 2016.

[128] Jeong San Kim and Barry C Sanders. Monogamy of multi-qubit entanglement using rényi entropy. *Journal of Physics A: Mathematical and Theoretical*, 43(44):445305, 2010.

[129] Yan-Kui Bai, Yuan-Fei Xu, and ZD Wang. General monogamy relation for the entanglement of formation in multiqubit systems. *Physical Review Letters*, 113(10):100503, 2014.

[130] Luigi Amico, Rosario Fazio, Andreas Osterloh, and Vlatko Vedral. Entanglement in many-body systems. *Reviews of modern physics*, 80(2):517, 2008.

[131] Asher Peres. Separability criterion for density matrices. *Physical Review Letters*, 77(8):1413, 1996.

[132] Rajiah Simon. Peres-horodecki separability criterion for continuous variable systems. *Physical Review Letters*, 84(12):2726, 2000.

[133] Reinhard F Werner and Michael M Wolf. Bound entangled gaussian states. *Physical Review Letters*, 86(16):3658, 2001.

[134] Gerardo Adesso, Alessio Serafini, and Fabrizio Illuminati. Extremal entanglement and mixedness in continuous variable systems. *Physical Review A*, 70(2):022318, 2004.

[135] Alessio Serafini, Fabrizio Illuminati, and Silvio De Siena. Symplectic invariants, entropic measures and correlations of gaussian states. *Journal of Physics B: Atomic, Molecular and Optical Physics*, 37(2):L21, 2003.

[136] Erik Aurell, Lucas Hackl, Paweł Horodecki, Robert H Jonsson, and Mario Kieburg. Random pure gaussian states and hawking radiation. *Physical Review Letters*, 133(6):060202, 2024.

[137] Gerardo Adesso, Alessio Serafini, and Fabrizio Illuminati. Determination of continuous variable entanglement by purity measurements. *Physical review letters*, 92(8):087901, 2004.

[138] Alonso Botero and Benni Reznik. Modewise entanglement of gaussian states. *Physical Review A*, 67(5):052311, 2003.

[139] Guillaume Verdon, Jacob Marks, Sasha Nanda, Stefan Leichenauer, and Jack Hidary. Quantum hamiltonian-based models and the variational quantum thermalizer algorithm. *arXiv preprint arXiv:1910.02071*, 2019.

[140] Jens Eisert, MB Plenio, S Bose, and J Hartley. Towards quantum entanglement in nanoelectromechanical devices. *Physical Review Letters*, 93(19):190402, 2004.

[141] Alonso Botero and Benni Reznik. Spatial structures and localization of vacuum entanglement in the linear harmonic chain. *Physical Review A—Atomic, Molecular, and Optical Physics*, 70(5):052329, 2004.

[142] Gerardo Adesso and Fabrizio Illuminati. Gaussian measures of entanglement versus negativities: Ordering of two-mode gaussian states. *Physical Review A*, 72(3):032334, 2005.

[143] AW Marshall. Inequalities: Theory of majorization and its applications, 1979.

[144] Philip J Davis. *Circulant Matrices*, volume 2. Wiley New York, 1979.

[145] Joseph Tindall, Amy Searle, Abdulla Alhajri, and Dieter Jaksch. Quantum physics in connected worlds. *Nature Communications*, 13(1):7445, 2022.

[146] David C Langreth and John P Perdew. Exchange-correlation energy of a metallic surface: Wave-vector analysis. *Physical Review B*, 15(6):2884, 1977.

[147] Olle Gunnarsson and Bengt I Lundqvist. Exchange and correlation in atoms, molecules, and solids by the spin-density-functional formalism. *Physical Review B*, 13(10):4274, 1976.

[148] Bogumil Jeziorski, Robert Moszynski, and Krzysztof Szalewicz. Perturbation theory approach to intermolecular potential energy surfaces of van der waals complexes. *Chemical Reviews*, 94(7):1887–1930, 1994.

[149] Hye-Young Kim, Jorge O Sofo, Darrell Velegol, Milton W Cole, and Amand A Lucas. van der waals forces between nanoclusters: Importance of many-body effects. *The Journal of chemical physics*, 124(7), 2006.

[150] D Langbein. Microscopic calculation of macroscopic dispersion energy. *Journal of Physics and Chemistry of Solids*, 32(1):133–138, 1971.

[151] Alexandre Tkatchenko, Alberto Ambrosetti, and Robert A DiStasio. Interatomic methods for the dispersion energy derived from the adiabatic connection fluctuation-dissipation theorem. *The Journal of Chemical Physics*, 138(7), 2013.

[152] Deyu Lu, Huy-Viet Nguyen, and Giulia Galli. Power series expansion of the random phase approximation correlation energy: The role of the third-and higher-order contributions. *The Journal of chemical physics*, 133(15), 2010.

[153] Murray Gell-Mann and Keith A Brueckner. Correlation energy of an electron gas at high density. *Physical Review*, 106(2):364, 1957.

[154] David Bohm and David Pines. A collective description of electron interactions: Iii. coulomb interactions in a degenerate electron gas. *Physical Review*, 92(3):609, 1953.

[155] MJ Renne and BRA Nijboer. Microscopic derivation of macroscopic van der waals forces. *Chemical Physics Letters*, 1(8):317–320, 1967.

[156] BM Axilrod and Ei Teller. Interaction of the van der waals type between three atoms. *The Journal of Chemical Physics*, 11(6):299–300, 1943.

[157] Frank Hansen and Gert K Pedersen. Jensen's operator inequality. *Bulletin of the London Mathematical Society*, 35(4):553–564, 2003.

[158] Roger A Horn and Charles R Johnson. *Matrix A mnalysis*. Cambridge university press, 2012.

[159] Guifré Vidal. Entanglement monotones. *Journal of Modern Optics*, 47(2-3):355–376, 2000.

[160] Alexander Ibrahim and Pierre-Nicholas Roy. Three-body potential energy surface for para-hydrogen. *The Journal of Chemical Physics*, 156(4), 2022.

[161] Robert J Hinde. Three-body interactions in solid parahydrogen. *Chemical Physics Letters*, 460(1-3):141–145, 2008.

[162] Peter Wind and Inge Røeggen. Ab initio calculation of three-body interaction in the (h2) 3 trimer. *Chemical physics*, 211(1-3):179–189, 1996.

[163] Alexander Ibrahim and Pierre-Nicholas Roy. Equation of state of solid parahydrogen using ab initio two-body and three-body interaction potentials. *The Journal of Chemical Physics*, 157(17), 2022.

[164] Matteo Gori, Philip Kurian, and Alexandre Tkatchenko. Second quantization of many-body dispersion interactions for chemical and biological systems. *Nature Communications*, 14(1):8218, 2023.

[165] Froilán M Dopico and Charles R Johnson. Parametrization of the matrix symplectic group and applications. *SIAM journal on matrix analysis and applications*, 31(2):650–673, 2009.

[166] Maksymilian Bujok, Alicja Smoktunowicz, and Grzegorz Borowik. On computing the symplectic llt factorization. *Numerical Algorithms*, 93(3):1401–1416, 2023.

[167] Tao Shi, Eugene Demler, and J Ignacio Cirac. Variational study of fermionic and bosonic systems with non-gaussian states: Theory and applications. *Annals of Physics*, 390:245–302, 2018.

[168] Tohya Hiroshima. Additivity and multiplicativity properties of some gaussian channels for gaussian inputs. *Physical Review A—Atomic, Molecular, and Optical Physics*, 73(1):012330, 2006.

[169] Nguyen Thanh Son, P-A Absil, Bin Gao, and Tatjana Stykel. Computing symplectic eigenpairs of symmetric positive-definite matrices via trace minimization and riemannian optimization. *SIAM Journal on Matrix Analysis and Applications*, 42(4):1732–1757, 2021.

[170] Pengzhan Jin, Yifa Tang, and Aiqing Zhu. Unit triangular factorization of the matrix symplectic group. *SIAM Journal on Matrix Analysis and Applications*, 41(4):1630–1650, 2020.

[171] Pengzhan Jin, Zhangli Lin, and Bo Xiao. Optimal unit triangular factorization of symplectic matrices. *Linear Algebra and its Applications*, 650:236–247, 2022.

[172] Kaare Brandt Petersen, Michael Syskind Pedersen, et al. The matrix cookbook. *Technical University of Denmark*, 7(15):510, 2008.

[173] Pauli Virtanen, Ralf Gommers, Travis E. Oliphant, Matt Haberland, Tyler Reddy, David Cournapeau, Evgeni Burovski, Pearu Peterson, Warren Weckesser, Jonathan Bright, Stéfan J. van der Walt, Matthew Brett, Joshua Wilson, K. Jarrod Millman, Nikolay Mayorov, Andrew R. J. Nelson, Eric Jones, Robert Kern, Eric Larson, C J Carey, İlhan Polat, Yu Feng, Eric W. Moore, Jake VanderPlas, Denis Laxalde, Josef Perktold, Robert Cimrman, Ian Henriksen, E. A. Quintero, Charles R. Harris, Anne M. Archibald, Antônio H. Ribeiro, Fabian Pedregosa, Paul van Mulbregt, and SciPy 1.0 Contributors. SciPy 1.0: Fundamental Algorithms for Scientific Computing in Python. *Nature Methods*, 17:261–272, 2020.

[174] Jorge Nocedal and Stephen J Wright. Conjugate gradient methods. *Numerical optimization*, pages 101–134, 2006.

[175] Jorge Nocedal and Stephen J Wright. *Numerical optimization*. Springer, 1999.

[176] Carlos Bravo-Prieto, Ryan LaRose, Marco Cerezo, Yigit Subasi, Lukasz Cincio, and Patrick J Coles. Variational quantum linear solver. *Quantum*, 7:1188, 2023.

[177] Dhrumil Patel, Patrick J Coles, and Mark M Wilde. Variational quantum algorithms for semidefinite programming. *Quantum*, 8:1374, 2024.

[178] Gloria Turati, Alessia Marruzzo, Maurizio Ferrari Dacrema, and Paolo Cremonesi. An empirical analysis on the effectiveness of the variational quantum linear solver. *arXiv preprint arXiv:2409.06339*, 2024.

[179] Keisuke Fujii, Hirotada Kobayashi, Tomoyuki Morimae, Harumichi Nishimura, Shuhei Tamate, and Seiichiro Tani. Impossibility of classically simulating one-clean-qubit model with multiplicative error. *Physical Review Letters*, 120(20):200502, 2018.

[180] Peter W Shor and Stephen P Jordan. Estimating jones polynomials is a complete problem for one clean qubit. *Quantum Information & Computation*, 8(8):681–714, 2008.

[181] Arvind, Biswadeb Dutta, N Mukunda, and R Simon. The real symplectic groups in quantum mechanics and optics. *Pramana*, 45:471–497, 1995.

[182] James Kennedy and Russell Eberhart. Particle swarm optimization. In *Proceedings of ICNN'95-international conference on neural networks*, volume 4, pages 1942–1948. ieee, 1995.

[183] Pier Paolo Poier, Louis Lagardere, and Jean-Philip Piquemal. O (n) stochastic evaluation of many-body van der waals energies in large complex systems. *Journal of Chemical Theory and Computation*, 18(3):1633–1645, 2022.

[184] Dario Massa, Alberto Ambrosetti, and Pier Luigi Silvestrelli. Many-body van der waals interactions beyond the dipole approximation. *The Journal of Chemical Physics*, 154(22), 2021.

[185] Pier Paolo Poier, Olivier Adjoua, Louis Lagardère, and Jean-Philip Piquemal. Generalized many-body dispersion correction through random-phase approximation for chemically accurate density functional theory. *The Journal of Physical Chemistry Letters*, 14(6):1609–1617, 2023.

[186] Dario Massa, Alberto Ambrosetti, and Pier Luigi Silvestrelli. Beyond-dipole van der waals contributions within the many-body dispersion framework. *Electronic Structure*, 3(4):044002, 2021.

[187] Pablo Sala, Tao Shi, Stefan Kühn, Mari Carmen Banuls, Eugene Demler, and Juan Ignacio Cirac. Variational study of u (1) and su (2) lattice gauge theories with gaussian states in 1+ 1 dimensions. *Physical Review D*, 98(3):034505, 2018.

[188] Christina V Kraus and J Ignacio Cirac. Generalized hartree–fock theory for interacting fermions in lattices: numerical methods. *New Journal of Physics*, 12(11):113004, 2010.

[189] Tommaso Guaita, Lucas Hackl, Tao Shi, Claudius Hubig, Eugene Demler, and J Ignacio Cirac. Gaussian time-dependent variational principle for the bose-hubbard model. *Physical Review B*, 100(9):094529, 2019.

[190] Yulia E Shchadilova, Fabian Grusdt, Alexey N Rubtsov, and Eugene Demler. Polaronic mass renormalization of impurities in bose-einstein condensates: Correlated gaussian-wave-function approach. *Physical Review A*, 93(4):043606, 2016.

[191] Lucas Hackl, Tommaso Guaita, Tao Shi, Jutho Haegeman, Eugene Demler, and J Ignacio Cirac. Geometry of variational methods: dynamics of closed quantum systems. *SciPost Physics*, 9(4):048, 2020.

[192] Hugo A Camargo, Lucas Hackl, Michal P Heller, Alexander Jahn, Tadashi Takayanagi, and Bennet Windt. Entanglement and complexity of purification in (1+ 1)-dimensional free conformal field theories. *Physical Review Research*, 3(1):013248, 2021.

[193] Lennart Bittel and Martin Kliesch. Training variational quantum algorithms is np-hard. *Physical Review Letters*, 127(12):120502, 2021.

[194] Jarrod R McClean, Sergio Boixo, Vadim N Smelyanskiy, Ryan Babbush, and Hartmut Neven. Barren plateaus in quantum neural network training landscapes. *Nature Communications*, 9(1):4812, 2018.

[195] Roeland Wiersema and Nathan Killoran. Optimizing quantum circuits with riemannian gradient flow. *Physical Review A*, 107(6):062421, 2023.

[196] David Wierichs, Christian Gogolin, and Michael Kastoryano. Avoiding local minima in variational quantum eigensolvers with the natural gradient optimizer. *Physical Review Research*, 2(4):043246, 2020.

[197] Martin Larocca, Supanut Thanasilp, Samson Wang, Kunal Sharma, Jacob Biamonte, Patrick J Coles, Lukasz Cincio, Jarrod R McClean, Zoë Holmes, and M Cerezo. A review of barren plateaus in variational quantum computing. *arXiv preprint arXiv:2405.00781*, 2024.

[198] Diego García-Martín, Paolo Braccia, and M Cerezo. Architectures and random properties of symplectic quantum circuits. *arXiv preprint arXiv:2405.10264*, 2024.

[199] Maxwell West, Antonio Anna Mele, Martin Larocca, and M Cerezo. Random ensembles of symplectic and unitary states are indistinguishable. *arXiv preprint arXiv:2409.16500*, 2024.

[200] Alice Barthe, M Cerezo, Andrew T Sornborger, Martin Larocca, and Diego García-Martín. Gate-based quantum simulation of gaussian bosonic circuits on exponentially many modes. *arXiv preprint arXiv:2407.06290*, 2024.

[201] Filipp Furche. Developing the random phase approximation into a practical post-kohn–sham correlation model. *The Journal of Chemical Physics*, 129(11), 2008.

[202] Patrick Bleiziffer, Marcel Krug, and Andreas Görling. Self-consistent kohn-sham method based on the adiabatic-connection fluctuation-dissipation theorem and the exact-exchange kernel. *The Journal of Chemical Physics*, 142(24), 2015.

[203] Marcus Cramer and Jens Eisert. Correlations, spectral gap and entanglement in harmonic quantum systems on generic lattices. *New Journal of Physics*, 8(5):71, 2006.

[204] Abdulnour Toukmaji, Celeste Sagui, John Board, and Tom Darden. Efficient particle-mesh ewald based approach to fixed and induced dipolar interactions. *The Journal of Chemical Physics*, 113(24):10913–10927, 2000.

[205] GE Astrakharchik, Giovanna Morigi, Gabriele De Chiara, and J Boronat. Ground state of low-dimensional dipolar gases: Linear and zigzag chains. *Physical Review A—Atomic, Molecular, and Optical Physics*, 78(6):063622, 2008.

[206] Efrat Shimshoni, Giovanna Morigi, and Shmuel Fishman. Quantum zigzag transition in ion chains. *Physical Review Letters*, 106(1):010401, 2011.

[207] Abhijit C Mehta, CJ Umrigar, Julia S Meyer, and Harold U Baranger. Zigzag phase transition in quantum wires. *Physical Review Letters*, 110(24):246802, 2013.

[208] Daniel HE Dubin. Theory of structural phase transitions in a trapped coulomb crystal. *Physical Review Letters*, 71(17):2753, 1993.

[209] Elisabeth Rieper, Janet Anders, and Vlatko Vedral. Entanglement at the quantum phase transition in a harmonic lattice. *New Journal of Physics*, 12(2):025017, 2010.

[210] Seunghoon Lee, Joonho Lee, Huanchen Zhai, Yu Tong, Alexander M Dalzell, Ashutosh Kumar, Phillip Helms, Johnnie Gray, Zhi-Hao Cui, Wenyuan Liu, et al. Evaluating the evidence for exponential quantum advantage in ground-state quantum chemistry. *Nature Communications*, 14(1):1952, 2023.

[211] Lexin Ding, Sam Mardazad, Sreetama Das, Szilárd Szalay, Ulrich Schollwock, Zoltán Zimborás, and Christian Schilling. Concept of orbital entanglement and correlation in quantum chemistry. *Journal of Chemical Theory and Computation*, 17(1):79–95, 2020.

[212] Lexin Ding and Christian Schilling. Correlation paradox of the dissociation limit: A quantum information perspective. *Journal of Chemical Theory and Computation*, 16(7):4159–4175, 2020.

[213] M Molina-Espíritu, RO Esquivel, S López-Rosa, and JS Dehesa. Quantum entanglement and chemical reactivity. *Journal of Chemical Theory and Computation*, 11(11):5144–5151, 2015.

[214] Katharina Boguslawski, Paweł Tecmer, Gergely Barcza, Örs Legeza, and Markus Reiher. Orbital entanglement in bond-formation processes. *Journal of Chemical Theory and Computation*, 9(7):2959–2973, 2013.

[215] Katharina Boguslawski, Pawel Tecmer, Ors Legeza, and Markus Reiher. Entanglement measures for single-and multireference correlation effects. *The Journal of Physical Chemistry Letters*, 3(21):3129–3135, 2012.

[216] Andrew M Bruckner and E Ostrow. Some function classes related to the class of convex functions. 1962.

[217] Jan Hermann, Martin Stöhr, Szabolcs Góger, Shayantan Chaudhuri, Bálint Aradi, Reinhard J Maurer, and Alexandre Tkatchenko. libmbd: A general-purpose package for scalable quantum many-body dispersion calculations. *The Journal of Chemical Physics*, 159(17), 2023.

[218] John P Perdew, Kieron Burke, and Matthias Ernzerhof. Generalized gradient approximation made simple. *Physical Review Letters*, 77(18):3865, 1996.

[219] Anthony M Reilly and Alexandre Tkatchenko. van der waals dispersion interactions in molecular materials: beyond pairwise additivity. *Chemical Science*, 6(6):3289–3301, 2015.

[220] Jan Hermann and Alexandre Tkatchenko. Density functional model for van der waals interactions: Unifying many-body atomic approaches with nonlocal functionals. *Physical Review Letters*, 124(14):146401, 2020.

[221] Sumeet Khatri, Ryan LaRose, Alexander Poremba, Lukasz Cincio, Andrew T Sornborger, and Patrick J Coles. Quantum-assisted quantum compiling. *Quantum*, 3:140, 2019.